Vacuum assembly, atomic source development, and micromotion studies for a trapped Ba^+ based quantum processor

by

Ali Mustafa Khatai

A thesis
presented to the University of Waterloo
in fulfillment of the
thesis requirement for the degree of
Master of Science
in
Physics (Quantum Information)

Waterloo, Ontario, Canada, 2025
© Ali Mustafa Khatai 2025

Author's Declaration

I hereby declare that I am the sole author of this thesis. This is a true copy of the thesis, including any required final revisions, as accepted by my examiners.

I understand that my thesis may be made electronically available to the public.

Abstract

Trapped-ions are one of the leading platforms for quantum information processing, due to their long coherence times and high-fidelity State Preparation and Measurement (SPAM) and gate operations. However, implementing a trapped-ion system with many desirable features such as Ultra-High-Vacuum (UHV), High-Optical-Access (HOA), and a high trapping probability presents significant technical challenges. These features are critical for enabling complex quantum simulation experiments, including simulations of spin-1/2 systems and beyond, by leveraging the multiple internal states of barium and tunable spin–spin interactions. High optical access is required to deliver tightly focused beams for site-resolved control and inter-ion coupling, while UHV conditions are essential for achieving long ion lifetimes necessary for stable, large-scale simulations. Achieving such optical access, which is vital for both coherent gate operations and high numerical aperture fluorescence collection, whilst maintaining vacuum integrity presents substantial engineering challenges. This thesis presents the construction of a vacuum chamber system intended for an individually addressable 16-qubit quantum processor based on barium-133 ions confined in a microfabricated surface-electrode ion trap. Although the complete processor has not yet been realized, the chamber has been assembled to support its future implementation. The microfabricated surface-electrode ion trap features ~ 100 electrodes that require independent control of static voltages for precise tailoring of the confining electric potential. The experimental setup was designed to provide high optical access and to reach base pressures in the low 10^{-11} mbar range, thereby minimizing ion–background gas collisions. This is achieved by centrally mounting the trap within the vacuum chamber, a departure from conventional flange-mounted designs. To bring in-vacuum electrical connections to ~ 100 trap electrodes, a custom implementation of an in-vacuum wire harness is described that enables reliable electrical connectivity to the centrally mounted surface-electrode ion trap. The development of this wire harness enabled us to reach UHV with a pressure of $\approx 3 \times 10^{-11}$mbar. The successful development of this wire harness demonstrates that it is possible to create a UHV compatible wiring solution using commercially available components for a surface-electrode ion trap suspended at the center of the vacuum chamber. This centrally mounted design provides both high optical access and high conductance to vacuum pumps, enabling individual ion addressing and long ion lifetimes, which in turn facilitate more complex quantum simulation experiments. In addition, a multispecies ablation target was developed that incorporates both radioactive barium-133 and metallic barium to enable ion loading at lower trap depths, addressing a common challenge in surface-electrode ion traps. The velocity of the atomic plume generated from barium metal ablation targets was measured and compared to that of $BaCl_2$ targets. Although we were unable to definitively measure the effective temperature and peak velocity of the

atomic plume generated from barium metal, the neutral fluorescence measurements from the barium metal targets indicate a larger number of slower moving atoms compared to $BaCl_2$ targets. The lower speeds of the atoms generated from metal targets is also plausible due to the low bond energy of metallic bonds compared to covalent bonds in salts. Barium has recently become a popular choice for high-fidelity trapped-ion experiments due to its favorable atomic structure. The larger number of slower moving atoms from barium metal demonstrates that metallic barium could be a much more promising atomic source for barium-based trapped-ion experiments, as the slower plume enables higher loading rates in surface-electrode ion trap systems.

Finally, excess micromotion, caused by stray electric fields in RF traps, can lead to undesirable effects such as heating and frequency modulation of atomic transitions. This work evaluates the micromotion compensation capabilities of the Phoenix ion trap used in our system through numerical simulations of single ion trajectories. Through these simulations, it was determined that stray fields of $E_x \approx 3000\,\mathrm{V/m}$, $E_y \approx 3800\,\mathrm{V/m}$, and $E_z \approx 600\,\mathrm{V/m}$ can be effectively compensated for with the Phoenix ion trap. With typical stray electric fields in trapped-ion systems ranging from tens to a few hundred V/m, this demonstrates that the Phoenix trap should be well capable of compensating any stray fields expected in our system.

Acknowledgements

A project as ambitious as building a quantum computer depends on the dedicated contributions of countless individuals across many disciplines. I am profoundly grateful to all those whose efforts and expertise have made this work possible.

I would like to express my heartfelt gratitude to my supervisor, Prof. Kazi Rajibul Islam, for giving me the opportunity to work under his guidance on such an exciting and cutting-edge project. Beyond being an exceptional teacher, he is an inspiring leader and mentor. I am especially grateful for his remarkable guidance and patience in mentoring me. I have consistently been impressed by his ability to make complex concepts clear and intuitive, making the learning experience both engaging and enlightening.

I would like to thank Prof. Crystal Senko, co-lead of the QuantumIon project. I have learned a great deal from her guidance in the lab and, in particular, from her trapped-ion class, which significantly deepened my understanding of the underlying physics of trapped-ion systems.

I would like to thank my supervisory committee members Prof. Kevin Resch and Prof. Bradley Hauer for their guidance and keeping me on track for my degree.

Most of my time during this degree was spent with the QuantumIon optics and vacuum team, working in the lab and cleanroom to assemble our system. I have had the pleasure of working closely with Dr. Akbar Jahangiri and Hawking Tan; both are wonderful colleagues, and I have learned a great deal from them. I will greatly value my time working with them. I joined the QuantumIon group at the same time as my fellow student Akimasa Ihara (Aki). Sharing the same office and spending countless hours together in the cleanroom allowed me to collaborate closely with him. Aki is not only an exceptional peer but has also become a great friend. Graduate school, especially with intensive lab work, can often be frustrating, but Aki's company, both inside and outside the lab, has made my graduate journey significantly more enjoyable and memorable.

I would like to extend special thanks to former PhD student Dr. Noah Greenberg, whose work has informed much of the content in my thesis related to the QuantumIon vacuum chamber. As the most senior student when I joined the group, he taught me a great deal about foundational trapped-ion physics and shared invaluable insights while working together in the cleanroom. I would like to thank PhD student Collin J.C. Epstein for his valuable insights on the *controlgen* package. Conversations with Collin were always highly enlightening, and I frequently learned important lessons about our control system and computer programming from him.

Special thanks to all the members of the QITI lab. Dr. Sainath Motlokunta and Dr. Nikhil Kotibaskar, who were assembling their blade trap system alongside us in the cleanroom, provided immense support and guidance. Fabien Lefebvre, who has also become a great friend, offered valuable insights on my ion trajectory simulations. Lewis Hahn provided significant support to the QuantumIon group during the final assembly and helped us machine various parts in the machine shop. It was also a pleasure to get to know and work with Sakshee, Shilpa, and Monica, especially during our study sessions for the Quantum Mechanics and trapped-ion class we took together. Special thanks to Nico, Gaurav and Pei Jiang from the Qudit lab for their insights on working with barium ions.

I, of course, must thank my family for their unwavering support and encouragement. My parents have always believed in me and provided constant guidance, motivation, and love throughout my academic journey. I am also grateful to my siblings and grandmother for their continual support, especially my brother Hussain, whose wise advice has been invaluable throughout my studies. Being far away from home for the entirety of my graduate degree was often challenging, but my aunt and cousins in Toronto provided a true home away from home. Their warmth, care, and hospitality made my time in Canada much more comfortable and enjoyable, and their support helped me navigate both the academic and personal challenges of living abroad.

Finally, I would like to thank all the wonderful friends I made throughout my time in graduate school, especially Andy, Ruhi, and Zach. Their company and support made my time in graduate school much more enjoyable and memorable.

Dedication

This is dedicated to my family

Table of Contents

Author's Declaration ii

Abstract iii

Acknowledgements v

Dedication vii

List of Figures xi

List of Tables xx

List of Abbreviations xxi

1 Introduction 1

1.1 Thesis outline 4

2 Ion trapping physics 7

2.1 The QuantumIon project 7

2.1.1 $^{133}Ba^{+}$ Qubit 8

2.2 Ion traps 15

2.2.1 4-rod linear Paul trap 17

2.2.2 Surface-electrode traps 20

2.3 Summary 27

3 QuantumIon Vacuum chamber setup **28**
3.1 UHV for trapped-ions . . . 28
3.2 QuantumIon vacuum chamber setup . . . 30
3.2.1 The experimental chamber . . . 31
3.2.2 The diagnostic chamber . . . 35
3.2.3 The five-way cross . . . 35
3.3 Summary . . . 36

4 Simulating Ion trajectories for Micromotion compensation **37**
4.1 Excess micromotion . . . 38
4.1.1 Effects of micromotion . . . 40
4.1.2 Compensating Micromotion . . . 40
4.1.3 Micromotion compensation in the Phoenix trap . . . 42
4.2 Simulating Ion trajectories . . . 43
4.2.1 *controlgen* . . . 44
4.2.2 Ion trajectory simulations . . . 46
4.2.3 Results . . . 50
4.3 Summary . . . 51

5 Barium atomic sources **55**
5.1 **$BaCl_2$** ablation targets . . . 56
5.2 Velocity of ablated atoms and trap depth . . . 57
5.2.1 Velocity of atomic plume from $BaCl_2$ targets . . . 57
5.2.2 Trap depth of the Phoenix trap . . . 58
5.3 Barium metal . . . 60
5.3.1 Neutral fluorescence and Time-of-Flight (TOF) . . . 61
5.3.2 Barium metal oxidation . . . 67
5.4 Ablation target holder . . . 69
5.5 Summary . . . 70

6 In-vacuum wire harness and vacuum chamber assembly **72**
6.1 UHV compatible in-vacuum wire harness 74
6.1.1 Issues encountered 77
6.1.2 Custom wire harness solution and assembly 79
6.2 Vacuum chamber assembly 88
6.2.1 Chamber sealing and Bake-out 88
6.3 Summary 105

7 Summary and outlook **106**

References **109**

APPENDICES **116**

A Wires harness components and tools **117**

List of Figures

2.1 **Energy level diagram of $^{133}Ba^{+}$ with relevant transitions, branching ratios and splitting (Not to scale)**. The computational basis states are encoded in the magnetic field insensitive clock states in the $6S_{1/2}$ manifold. All but one relevant transition is in the visible spectrum and the long lived states in the D-manifold with lifetimes of 35 s and 85 s allow for shelving operations. Adapted from [11, 65]. 10

2.2 **Depiction of the two-step isotope-selective photoionization scheme used in the QuantumIon system**. The first step excites the 553 nm transition in neutral barium, which can be isotope selective due to the isotope shift. The second step uses a 405 nm laser to drive the electron to the continuum. Figure adapted from [22, 16, 65]. 12

2.3 **Energy level diagram of $^{133}Ba^{+}$ with transitions relevant to Doppler cooling, and SPAM (Not to scale)**. The $|6S_{1/2}, F = 1\rangle = |1\rangle \leftrightarrow |6P_{1/2}, F = 1\rangle$ pumps the ion to $|0\rangle$. The cycling transition $|6S_{1/2}, F = 1\rangle = |1\rangle \leftrightarrow |6P_{1/2}, F = 0\rangle$ continually emits photons if the ion is in $|1\rangle$ and remains dark otherwise. 15

2.4 **Plot of a saddle potential using Eq. 2.2 with $\alpha = -1$, $\beta = 1$, $\gamma = 1$.** The potential is confining in the x direction and anti confining in the y direction. The confining and anti-confining directions are swapped before the ion has a chance to escape. The saddle point is shown in red. Adapted from [45]. 17

2.5 **Schematic of a 4-rod linear Paul trap (Not to scale)**. a) Oblique angle view of a 4 rod trap. V_{RF} is applied to a pair of diagonal electrodes and the other two are grounded for confinement along x and y-axis (radial). Two needle electrodes receive a static Direct current (DC) voltage U_0 for confinement along the z-axis (axial direction or the trap axis). b) Shows a end-view of the trap with the needle electrodes omitted. The dashed blue lines show the electric fields generated by the electrodes. This configuration generates a quadrupole pseudopotential with a minimum known as the Radio Frequency (RF) null in the center of the trap marked by the black dot. Adapted from [65]. 19

2.6 **Simulated trajectory of a trapped ion according to Eq.** (2.12). The plot shows the secular motion (blue), the micromotion component (green), and the total motion (thin orange). The secular motion corresponds to harmonic oscillations at the secular frequency $\omega_x = 2\pi \times 3\,\text{MHz}$, with an amplitude $u_{1i} = 1\mu\text{m}$. The micromotion arises from the RF drive at frequency $\Omega_{RF} = 2\pi \times 36\,\text{MHz}$, with a Mathieu parameter $q_i = 0.3$. 21

2.7 **Schematic of a five-wire surface-electrode trap**. a) Illustration of how a surface-electrode trap is essentially a "unrolled" 4-rod trap. b) Shows the five wire design with the DC electrodes in maroon for axial confinement. c) Shows the confining electric field lines generated by a surface-electrode trap. The potential minimum lies a certain distance above the trap. Adapted from [49]. 22

2.8 **Close-up image of the Phoenix trap (Top) and CAD rendering of the trap Ceramic Pin Grid Array (CPGA) (bottom)**. The bowtie shape of the trap gives high optical access by allowing beams to come from the vertical direction in the image above without clipping on the trap surface. The CPGA resembles a computer CPU with the trap on one side and connection pins on the other. Images taken from [54]. 24

2.9 **Electrode layout of the Phoenix trap with trap zones labeled**. The quantum zone shows a close up of the symmetric six-rail design. Adapted from [54]. 25

2.10 **Scanning Electron Micro-graph (SEM) image of the Phoenix trap**. The wire bonds making the electrical connections from the trap to the CPGA are kept away from the quantum zone to prevent laser beams clipping on them. Image taken from [54]. 26

3.1 **Two implementations of a flange mounted surface-electrode trap design**. The trap being mounted onto a chamber flange makes electrical connections to the trap much less complex. Left image taken from [35] and right image from [25]. 32

3.2 **Schematic and image of the QuantumIon vacuum chamber**. a) Internal cross-section view of the QuantumIon vacuum chamber. There are three main sections, the diagnostic chamber, the five-way cross and the experimental chamber. The view also shows where the ion pump and NEG pumps are connected on the chamber. b) Picture of the actual chamber in our lab. The experimental chamber houses the trap and is located at the bottom of the system directly above a valley in the optics table. We call this the imaging valley as it contains all the optics for imaging ions through the 0.6 Numerical Aperture (NA) re-entrant at the bottom of the experimental chamber. Adapted from [22]. 33

3.3 **Schematic of the experimental chamber that house the surface-electrode trap and atomic sources**. a) The trap is mounted in the geometric center of the chamber. The high NA re-entrants allow high optical access to the trap. b) Bottom view of the experimental chamber. The Raman individual addressing beams enter from the high NA re-entrants where as the 493, 650, 553, and 405 nm lasers enter from view ports on the diagonals of the chamber. The DC and RF electrical connections to the trap enter the vacuum chamber through an electrical feed-through. Adapted from [22]. 34

4.1 **Illustration of how a static stray electric field $\mathbf{E}_{DC}$ can induce excess micromotion**. a) Without any stray electric field both the DC and RF potential nulls coincide in space where the ion sits. b) In the presence of a stray electric field the DC null is displaced from the RF null, the ion moves to a new average position and experiences a higher RF potential leading to excess micromotion. 39

4.2 **Voltage configurations for stray electric field compensation**. Shows a cut out of the center of the quantum region of the Phoenix trap with voltages configurations to generate micromotion compensation fields along x, y, and z directions. Adapted from [18]. 43

4.3 **DC voltages and the corresponding electric potential for trapping an ion in the Phoenix trap**. a) Shows the DC voltages for axial confinement in the center of the quantum zone of the Phoenix trap. b) Shows the Radial DC potential + RF pseudopotential for $V_0 = 150V$ and $\Omega_{RF} = 32.9$MHz. C) Shows the potential along the axial direction for the DC voltages in a). We can see the minimum close to 0 which is the center of the trap. 47

4.4 **Trajectories of a $^{133}Ba^+$ ion in all directions as well as the radial plane.** We can clearly see that the trajectories follow Eq. (2.12) with a slow secular motion and fast micromotion. RF voltage amplitude $V_0 = 150V$, RF drive frequency $\Omega_{RF} = 32.9\,\mathrm{MHz}$ and the DC voltage from Fig. 4.3 a) where used for these trajectories. 48

4.5 **Fast-Fourier-Transform (FFT) spectrum of the ion's trajectories**. The plots in the right column show the secular frequencies. Plots in the left column show the two sidebands and central peak for intrinsic and excess micromotion respectively. The central peak at the RF drive frequency is very small as there are no stray electric fields and hence no micromotion. . 52

4.6 **Ion's trajectories and their FFT spectrums in the presence of a stray electric field $E_x \approx 3000\,\mathrm{V/m}$, $E_y \approx 3800\,\mathrm{V/m}$, and $E_z \approx 600\,\mathrm{V/m}$.** We see a significant increase the the micromotion and secular motion amplitude in the radial directions (x and y) compared to Fig. 4.4. The FFTs show a much larger excess micromotion peak in the radial directions compared to Fig. 4.5. Motion along the axial direction remains mostly unchanged. . . . 53

4.7 **Ion's trajectories and their FFT spectrums in the presence of a stray electric field and compensation fields turned on**. The micromotion and secular motion amplitudes go back down what they were with no stray electric field (see Fig. 4.5). This shows that we have successfully pushed the ion back to the RF null and almost completely eliminated the excess micromotion. 54

5.1 **Ablation TOF spectrum of $BaCl_2$**. a) shows the time of flight distribution. b) Shows the velocity distribution fitted to a Maxwell-Boltzmann distribution. A plume temperature of $37{,}000 \pm 1{,}000\,\mathrm{K}$ and a peak velocity of $2{,}600 \pm 50\,\mathrm{m/s}$ is estimated from this data. Taken from [70, 8]. 58

5.2 **PMT counts as a function of the frequency of the 553 nm laser after ablation of $BaCl_2$ ablation targets**. We can see that the most abundant isotope is ^{138}Ba, but other isotopes are also clearly present. The ^{138}Ba peak occurs at 541.43300 THz. Taken from [22]. 61

5.3 **Experimental setup of the barium metal neutral fluorescence and TOF experiments**. a) and b) show a diagram of the experimental setup, showing the beam orientations. The target is placed d=11.35 mm from the 553 nm laser . The inset in b) shows a CAD rendering of the ablation target holder. c) Shows an image of the actual setup in the lab. d) Pulse sequence for the experiments. 0 μs marks the beginning of the experiments when the trigger signal is sent to the ablation laser. The ablation pulse arrives $\sim 75\,\mu$s after the experiment is started. The PMT starts registering photon counts after a delay of t_d after the ablation pulse for a collection window of Δt. Adapted from [22]. 63

5.4 **Neutral fluorescence of ablated barium metal**. Each ablation pulse of the 553 nm laser is switched between the resonant and non-resonant (1 GHz detuned) frequency to compare background counts to the signal from the barium atoms. We see a clear distinction in fluorescence counts between the resonant and non-resonant case which confirms that we are able to produce neutral barium atoms from ablation of barium metal. 64

5.5 **TOF spectroscopy results of ablated barium metal**. a) Shows the TOF distribution. b) Velocity distribution obtained by scaling the TOF data in a) by $1/t_d$ and converting to velocity. A "peak" velocity corresponding to the maximum fluorescence signal $v_{peak} = 333.8\,$m/s is obtained. 66

5.6 **Images of the barium metal source and its oxidation**. a) Image of the barium metal chunk inside a sealed glass ampule filled with inert argon gas to prevent oxidation. We can see it has a clear metallic sheen before it oxidizes. b) Images of the barium metal after being exposed to air for 10 and 30 minutes respectively. After 10 minutes we can see some white BaO appear on the surface and after 30 minutes it turns completely white. The oxide easily flakes off the metal and can contaminate the surface-electrode trap. 68

5.7 **The ablation target holder used in the QuantumIon system**. a) Shows a CAD rendering of the ablation target holder. b) Shows an image of the ablation target holder indicating where each type of source will be installed. c) Shows the back part of the holder with a chunk of barium metal installed in it. 69

5.8 **CAD rendering of two views of the ablation target holder and the surface-electrode trap**. The targets are approximately 14 mm away from the trap. The surface normals of each target is directly pointed at the trapping region of the trap so that that atomic plume generated during laser ablation goes straight to the trapping region. 70

6.1 **Mounting of the Phoenix trap inside the experimental chamber and the PCB + Zero-Insertion-Force (ZIF) socket assembly**. a) Shows a CAD rendering of how the Phoenix trap is mounted inside the experimental chamber. b) Shows images of the PCB + ZIF socket assembly. The trap CPGA mounts in the ZIF socket. The PCB distributes the dense pin layout of the ZIF socket to a more accessible layout for easier soldering. 76

6.2 **Image of the Micro-D wire harness and how it interfaces with the Phoenix trap**. a) Image of the commercially available Micro-D connector wire harness made with Polyether ether ketone (PEEK) (beige connector in b) and Kapton insulated wires. The PEEK connector mates with the Micro-D socket on the feedthrough flange and the wires are soldered onto the PCB shown in Fig. 6.1. b) Image of the wires harness soldered to the PCB. 77

6.3 **Microscope images of the flakes on the Kapton insulated wires**. The images clearly show little flakes of the Kapton coming off of the wires. These flakes were found on the commercially available wires harness out of the box. The flaking got worse when the wires were sonicated in Isopropyl Alcohol (IPA) to clean them. The Kapton wires are in close proximity of the surface-electrode trap (few centimeters) which means it is highly likely for these flakes to contaminate the trap's electrodes. 79

6.4 **Wire crimping procedure for the PCB side crimp pins**. 1) Strip a 4 mm section of the Kapton insulation. 2) Two strands of the stranded core wire are separated from the main bundle. 3) The two separated strands are trimmed 1 mm above the Kapton insulation. 4) Fold the stripped wire over the Kapton insulation. 5) Insert wire into the pin making sure the Kapton part is inside the pin and then crimp the pin. 82

6.5 **Wire crimping procedure for the ZIF side crimp pins**. 1) Strip a 5 mm section of the Kapton insulation. 2) Fold the wire over the Kapton insulation. 3) Insert the wire into the crimp pin making sure the Kapton part is inside the pin and crimp the pin right above the vent hole. In this case the entire stranded core is folded over the Kapton insulation, as these connections interface with wider crimp pins that accommodate the full wire gauge. 83

6.6 **Soldered PCB+ZIF socket assembly**. a) Shows the entire wire harness assembly after the wires are soldered onto the PCB+ZIF socket assembly. b) Shows a close up of the wires that were soldered directly onto the ZIF socket pins instead of the PCB for easier soldering. c) Shows a side view of the assembly. This assembly was cleaned in a sonicator bath with IPA with the IPA level just above the gold crimp pins to ensure the Kapton wires were not sonicated. 85

6.7 **Image of the completed in-vacuum wire harness ZIF socket assembly**. The CPGA of the Phoenix trap mounts into the ZIF socket. The stainless steel bridge attaches the assembly inside the vacuum chamber by screwing into brackets inside the chamber. The PEEK micro-D connector connects to the UHV electrical feedthrough on the vacuum chamber flange which makes the electrical connections accessible from outside the vacuum chamber. 87

6.8 **Alignment jigs used to center the Phoenix trap**. a) Shows an image of the alignments jigs installed in the chamber and being used to align the wire harness ZIF socket assembly. b) Shows a CAD rendering of the alignment jig. The mock trap CPGA fits into the notches in the alignment jigs. These notches and the jig are referenced to the experimental chamber and attached to it via the multiple bolts that are used for attaching the Raman re-entrants. The large number of bolts tightly constrains the jig to the chamber. This ensures the traps is within 150 μm of the chamber's center. 89

6.9 **Shows the assembly station and cleanroom setup where the vacuum chamber was assembled**. We can see the chamber connected to the turbomolecular pump in red. 90

6.10 **Bolt tightening sequence used for sealing the Conflat (CF) flanges on our vacuum chamber**. The chamber has 2.75 inch CF flanges with 6 bolts, 4.5 inch CF flanges with 8 bolts, and 8 inch CF flanges with 20 bolts. 92

6.11 **Image of the vacuum chamber inside the TestEquity 1027C Temperature Chamber**. The bellows for the turbomolecular pump are feed into the temperature chamber through a feedthrough on the right. 93

6.12 **Installation procedure of the Phoenix trap**. a) Shows PhD student Akimasa Ihara installing the Phoenix trap into the experimental chamber from the bottom. After the trap is inserted into the ZIF socket, another lab member tightens it in place. b) Shows a bottom view of the trap installed in the experimental chamber. c) Shows a side view of the trap installed in the chamber. 97

6.13 **Assembly of the ablation target holder + shield assembly inside the nitrogen filled glove bag**. a) Shows the smaller in-house made nitrogen filled glove bag used to assemble the ablation target holder + shield assembly in order to minimize exposure of the barium metal to oxygen and reduce oxidation. Two lab members need to work together to put the assembly together using tweezers and screw drivers. b) Shows the two halves of the ablation target being joined together. c) Shows the ablation target being installed onto the metal shield. 98

6.14 **Shows the ablation target holder + shield assembly installed inside the experimental chamber**. a) and b) shows two views of the ablation target + shield installed inside the chamber after it was sealed. In a) we can clearly see that the barium metal source still has the its silvery metallic surface that it had before being removed from the glass ampule. This indicated that we were successfully able to mitigate excessive oxidation of the barium metal. c) Shows an image of the metal shield installed in the trap from the bottom of the chamber before it is sealed. 99

6.15 **Nitrogen filled glove bag for installation of the ablation target holder + shield assembly**. a) Show the larger in-house made nitrogen filled glove bag attached over the experimental chamber with cleanroom grade tape. The bag and the vacuum chamber are filled with nitrogen gas to minimize the exposure of the barium metal to oxygen whilst it sits in the chamber while it is being sealed. b) Shows PhD student Akimasa Ihara underneath the glove bag installing the ablation target holder + shield assembly whilst other lab members hand in components and tools through an opening in the glove bag. 100

6.16 **Moving the vacuum chamber to the Lab**. a) and b) shows the process of moving our vacuum chamber from the cleanroom in RAC-1 where it was assembled to our lab in RAC-2. c) Shows our vacuum chamber installed onto the optics table in our lab. 102

6.17 **Pressure of the vacuum chamber during the short bake and a few days after it was moved to the lab**. The plotting begins once the pressure reaches the 10^{-7} mbar level as that is when the extractor gauge can be turned on. The plot shows several spikes and gaps. The spikes are due to the degassing procedures done during bakeout and the gaps are due to connection loss or turning the gauge off when moving the chamber. The chamber was moved to the lab on November 25th 2024 and we can see that about 4 days after that the pressures started to plateau to around 3×10^{-11} mbar. 104

List of Tables

6.1 **Vacuum components used to achieve UHV pressures.** 90

A.1 **Components used in the In-vacuum wire harness assembly.** All components are UHV compatible as our chamber achieved $\approx 3 \times 10^{-11}$ pressure with these components inside. 118

A.2 **Tools used for the in-vacuum wire harness assembly.** 119

List of Abbreviations

ARTIQ Advanced Real-Time Infrastructure for Quantum physics 49

CF Conflat xviii, 91, 92

CPGA Ceramic Pin Grid Array xii, xvi, xvii, 24–26, 73, 75, 76, 86–89

DAC Digital-to-Analog Converter 49, 51, 106

DC Direct current xii–xiv, 18–20, 22, 23, 25, 34, 38–50, 75, 83, 102, 103, 118

EIT Electromagnetically Induced Transparency 13, 14

FFT Fast-Fourier-Transform xiv, 46, 49, 50, 52–54

HOA High-Optical-Access iii, 5, 8, 25, 28

HTCC High-Temperature Co-fired Ceramic 26

HV High-Vacuum 35, 62

ID Inner-Diameter 91

IPA Isopropyl Alcohol xvi, xvii, 77–81, 84, 85

IR Infrared 9

NA Numerical Aperture xiii, 31–34, 36, 62, 107, 108

NEG Non-Evaporable Getter 35, 36, 81, 89, 94, 101, 103

NISQ Noisy Intermediate-Scale Quantum 1–3

NIST National Institute of Science and Technology 49

OMG Optical-Metastable-Ground 9

PEEK Polyether ether ketone xvi, xvii, 75, 77, 84, 85, 87

PMT Photomultiplier Tube 14, 57, 62

PPM Parts-Per-Million 95

QCCD Quantum Charge-Coupled Device 23

RF Radio Frequency xii–xiv, 5, 16–20, 25–27, 29, 34, 37–50, 52, 54, 58, 59, 75, 83, 118

RGA Residual Gas Analyzer 35, 36, 92–94, 101

RSC Resolved Sideband Cooling 14, 40

SEM Scanning Electron Micro-graph xii, 25, 26

SPAM State Preparation and Measurement iii, xi, 2, 5, 7, 8, 15, 27, 107, 108

TOF Time-of-Flight ix, xiv, xv, 5, 55–58, 61–64, 66

UHV Ultra-High-Vacuum iii, ix, x, xvii, xx, 4–6, 8, 28–31, 35, 36, 62, 67, 72–75, 77–80, 83, 87–91, 103, 105, 107, 118

UPS Uninterruptable-Power-Supply 102

UV Ultra-Violet 9

ZIF Zero-Insertion-Force xvi–xviii, 75–78, 80–89, 92, 96, 97, 118

Chapter 1

Introduction

The first quantum revolution, in the early 1900s, which was fueled by the discoveries of pioneers like Max Planck, Albert Einstein, Niels Bohr, Erwin Schrödinger, led to the development of many useful technologies that are now essential to modern life such as transistors, light emitting diodes, MRI scanners among others. Today, we are in the midst of a second quantum revolution, one which focuses on using quantum phenomena to perform useful computations and simulations. As early as the 1980s, Yuri Manin and Paul Benioff had already started exploring the idea of computation governed by the laws of quantum mechanics [1, 5]. In 1981, Richard Feynman famously suggested that in order to efficiently simulate natural phenomena, one would need a machine that follows the laws of quantum mechanics [17], thus planting the conceptual seed of what we now call a quantum computer.

Since Feynman's proposal, the field of quantum information and computing has grown tremendously. The development of quantum algorithms such as Shor's algorithm to efficiently factor large integers [60] and Grover's algorithm to accelerate unstructured search [24] demonstrated the potential of quantum computers to outperform their classical counterparts. These breakthroughs, along with the emergence of foundational concepts like quantum error correction and fault-tolerant quantum computing [52], motivated serious experimental efforts toward the physical realization of quantum hardware. However, implementing these algorithms at a practically useful scale requires gate and measurement fidelities to exceed certain thresholds to enable reliable quantum error correction, which remains a significant engineering challenge. We are currently in the Noisy Intermediate-Scale Quantum (NISQ) era of quantum computing [53], characterized by devices with tens to hundreds of qubits but limited by noise and decoherence. Despite these limitations, current gate and measurement fidelities are sufficient for near-term applications such as quantum

simulation [53]. Quantum simulation is a powerful approach for exploring quantum system. It involves using a highly controllable quantum system to mimic and then investigate the dynamics of other complex quantum systems that are intractable for classical computers. This was, in fact, the original motivation behind Feynman's vision. Quantum simulation holds promise for advancing our understanding of complex problems in diverse fields such as condensed matter physics, high-energy physics, atomic physics, quantum chemistry, and cosmology [20]. The practical realization of quantum simulation demands a physical quantum system that offers high controllability and long coherence times. A variety of quantum systems can be employed for this including trapped-ions, neutral atoms, superconducting circuits, and photons. This thesis focuses on the trapped-ion platform for quantum computing.

In the NISQ era, trapped-ions have emerged as a leading candidate since the early days of quantum computing research. Several fundamental features make trapped-ions particularly well-suited for quantum computing, as will be outlined below:

1. **Long coherence times**
   Information encoded in the energy levels of the internal electronic ground state of a trapped-ion benefits from strong isolation from the surrounding environment. This isolation has allowed the trapped-ion platform to achieve some of the longest qubit coherence times ever recorded, including a landmark demonstration of coherence exceeding one hour [68].

2. **High State Preparation and Measurement fidelities**
   Encoding information in the internal energy states of an ion offers the additional advantage of utilizing transitions to auxiliary excited states, which facilitate qubit manipulation and readout via optical pumping and state-dependent fluorescence techniques. Using these methods, recent experiments have achieved a record SPAM fidelity of 99.9993% [63].

3. **Free from fabrication defects**
   To the best of our knowledge, all ions of any given element are fundamentally identical, earning them the designation of "nature's qubits". This intrinsic uniformity makes them ideal candidates for qubits, as it eliminates concerns about fabrication defects, which are a major source of error in manufactured qubit platforms such as superconducting systems.

A powerful quantum simulator is one that can flexibly model complex quantum systems by faithfully mimicking their underlying physics. In the most general terms, this requires

not just a collection of qubits, but a tunable system of interacting qubits. Trapped-ions naturally provide this capability through phonon-mediated interactions. When multiple ions are confined in a trap, they form an ordered structure because of their mutual repulsion. Rather than interacting directly, the ions are coupled through their shared motion modes, which are modes of the quantum harmonic oscillator due to the confining potential being harmonic in nature. Each qubit is encoded in two ground state internal electronic energy levels of an ion. Depending on the ion species and experimental design, these can be hyperfine sub-levels, Zeeman sub-levels, or metastable states which enables what is known as the Optical–Metastable–Ground (OMG) architecture [3]. The two internal ground states can serve as effective spin-$\frac{1}{2}$ states and laser-based spin-dependent forces can be used to couple these internal spin states to the ions' collective motion, mediating tunable interactions between any pair of ions in the chain. This shared motional coupling provides native all-to-all connectivity, a feature unique to trapped-ion systems and not available in platforms limited to short-range interactions.

In condensed matter physics, many-body spin models are essential for describing collective quantum phenomena such as magnetism, quantum phase transitions, and topological order. Trapped-ion systems are particularly well suited for simulating these models, as they offer precise control over spin interactions and the flexibility to engineer a wide range of Hamiltonians. The ability to tune the strength and range of interactions, combined with long coherence times and high fidelity control, allows trapped-ions to effectively perform quantum simulation of spin-spin interacting systems [41]. Significant research progress has been made in simulating specific Hamiltonians in trapped-ion systems [51, 33, 56, 29].

The field of trapped-ion quantum simulation is entering a transformative stage. As research moves beyond early demonstrations, the focus is shifting toward expanding the practical capabilities of NISQ era devices. Several key directions have emerged as especially promising for unlocking the next level of performance.

1. **Scaling to larger systems**. Increasing the number of qubits expands the size and complexity of the systems we can simulate.

2. **Improved control of qubit internal states and ion-ion coupling**. Enhanced control techniques enable high-fidelity operations, precise state manipulation, and reliable interactions, supporting more complex quantum simulation experiments.

3. **Expanding internal state space**. Using atomic species with more long-lived internal states enables access to higher-dimensional Hilbert spaces. This allows various encoding schemes including qudits, supports new state preparation and measurement

(SPAM) schemes, and opens up possibilities for simulating more complex quantum systems with richer internal dynamics.

4. **Reducing decoherence to increase the usable time of devices**. Minimizing decoherence allows for longer quantum simulation experiments.

Scaling up the number of qubits requires precise and customizable trapping potentials for shuttling ions and regular ion spacing. Photonic interconnects can be used to connect multiple ion traps and highly engineered optical systems would be needed to optically address a large number of ion qubits. Enhanced control of qubits requires precise individual addressing of ions using tightly focused laser beams with minimal crosstalk and regular ion spacing. In order to individually address a large number of ions in a long chain, it is important that the ions maintain regular spacing along the trap axis. Uniform spacing ensures that focused laser beams can reliably target specific ions without crosstalk, simplifies the design of beam-shaping and delivery optics, and can reduce the complexity of imaging and detection systems used for state readout. Accurate control of laser parameters, such as frequency, intensity, and polarization, is essential for manipulating both internal states and motional couplings between ions. Expanding the internal state space depends on using atomic species with many long-lived internal states, such as the metastable states in barium. Longer coherence times can be achieved by maintaining UHV conditions, which reduces ion collisions with background gases that would otherwise disrupt the quantum state of the ions.

The work presented in this thesis contributes to the construction of a barium-based trapped-ion quantum simulator/processor that addresses several of the research directions outlined above and discusses the technical challenges encountered in the process. The next section provides a brief outline of my work.

1.1 Thesis outline

The work presented in this thesis is part of the QuantumIon project, which is a collaboration between Prof. Kazi Rajibul Islam and Prof. Crystal Senko to build a barium-133 based trapped-ion quantum processor/simulator. I joined the QuantumIon project in September 2023, at a time when the group was actively working on assembling the vacuum chamber used for our system. As a result, a significant portion of my master's research was dedicated to the installation of the Phoenix ion trap and atomic source ablation targets into the chamber, followed by sealing the chamber, achieving UHV pressures, and relocating

the chamber from the cleanroom, where the assembly was carried out, to the main laboratory. During this period, we addressed several critical challenges that arose throughout the assembly and integration process. In addition to this, I also worked on single ion trajectory simulations to analyze the micromotion compensation capabilities of our surface-electrode ion trap.

The remaining chapters of this thesis are structured as follows:

- **Chapter 2**: Introduces the QuantumIon project and provides a foundational overview of ion trapping physics. It covers the $^{133}Ba^{+}$ qubit, standard experimental techniques such as ion loading, Doppler cooling, and SPAM, and explains ion confinement using RF electric fields. The chapter also outlines the surface-electrode architecture for ion traps and introduces the Phoenix ion trap used in our system.

- **Chapter 3**: Describes the design of the vacuum chamber setup used in our system. This chapter discusses how it can be challenging to design a vacuum chamber with both HOA and low vacuum pressures. It describes how our chamber mounts the surface-electrode trap in the center of the vacuum chamber, enabling higher optical access and high-conductance to vacuum pumps to achieve lower pressures.

- **Chapter 4**: Introduces the problem of excess micromotion, caused by stray electric fields in trapped-ion systems. The micromotion compensation capabilities of the Phoenix trap are analyzed using numerical simulations of single ion trajectories. This chapter analyzes the levels of stray electric fields that can be effectively compensated by the Phoenix trap.

- **Chapter 5**: This chapter discusses the types of barium sources used as ablation targets installed in our vacuum chamber. A key result presented is the successful integration of a metallic barium source. Neutral fluorescence and TOF spectroscopy data of the metallic barium target are shown. The speed of the atomic plume generated from $BaCl_2$ targets is compared to that from metal targets, demonstrating that metal targets produce a larger number of slower moving atoms. The slower atomic velocity facilitates higher ion loading rates in surface-electrode traps with shallower trap depths.

- **Chapter 6**: This chapter describes the assembly of the vacuum chamber used in our system, including the implementation of a custom UHV-compatible wire harness with approximately 100 connections to the Phoenix trap. The integration of a radioactive

source alongside a rapidly oxidizing barium metal source during the assembly procedure is detailed. Finally, the process of sealing the chamber and achieving UHV pressures is discussed.

Chapter 2

Ion trapping physics

This chapter introduces the QuantumIon project and its key features. Section 2.1 explores the properties of the $^{133}Ba^{+}$ ion and motivates its use in our system. It also provides an overview of conventional experimental techniques used in trapped-ion laboratories, with a focus on their application to $^{133}Ba^{+}$, including ion loading, Doppler cooling, and SPAM methods. Section 2.2 describes how atomic ions are confined using electric fields and introduces the surface-electrode ion trap architecture, highlighting its advantages for scaling up trapped-ion systems. It concludes with an overview of the Phoenix surface-electrode trap (Phoenix trap), developed by Sandia National Laboratories, which is used in our system.

2.1 The QuantumIon project

The research presented in this thesis is part of the QuantumIon project at the Institute of Quantum Computing. The overarching goal of this initiative is to develop an open-access quantum processor that enables researchers to test novel ideas without the need to construct their own experimental platforms. The QuantumIon system will feature 16 individually addressable trapped-ion qubits, realized using $^{133}Ba^{+}$ ions confined in a microfabricated surface-electrode trap designed and manufactured by Sandia National Laboratories [54].

The primary qubit species for this platform is the isotope $^{133}Ba^{+}$, chosen for its favorable atomic structure. However, the system incorporates a multi-species atomic source, enabling the trapping of alternative isotopes such as $^{137}Ba^{+}$ and $^{138}Ba^{+}$, providing flexibility for future investigations. In addition to its qubit versatility, the QuantumIon system

distinguishes itself from other surface-electrode trap implementations through its HOA and UHV environment, key features that will be described in detail in chapter 3. Portions of the explanatory structure and system description in the following sections are informed by [16, 65], which provided valuable guidance in framing the presentation of this material.

2.1.1 $^{133}Ba^{+}$ Qubit

Barium is an alkaline-earth metal that behaves as a *hydrogen-like* ion when one of its valence electrons is removed via photoionization, resulting in a positively charged ion. $^{133}Ba^{+}$, a manufactured radioisotope, has recently gained serious attention within the trapped-ion community as a promising qubit candidate, commonly referred to as the "Goldilocks Qubit" [28]. Its energy level structure is illustrated in Fig. 2.1. The growing popularity of $^{133}Ba^{+}$ as a qubit is attributed to the several key advantages discussed below.

1. **Simple hyperfine structure**
   As can be seen in Fig. 2.1, the spin-$\frac{1}{2}$ nucleus of $^{133}Ba^{+}$ gives rise to the simplest possible hyperfine structure. The computational basis states can be encoded as $|0\rangle = |F = 0, m_f = 0\rangle$ and $|1\rangle = |F = 1, m_f = 0\rangle$ in the "clock states" within the $S_{1/2}$ manifold. Theses states are magnetic field insensitive to first (linear) order which makes them more immune to decoherence caused by ambient magnetic field fluctuations. The minimal hyperfine structure significantly reduces leakage to auxiliary levels during state preparation, measurement, and gate operations, contributing to high SPAM and gate fidelities. In comparison, $^{137}Ba^{+}$, which has a nuclear spin of $I = \frac{3}{2}$, exhibits a more complex hyperfine structure. Its corresponding clock states are typically defined as $|0\rangle = |F = 1, m_f = 0\rangle$ and $|1\rangle = |F = 2, m_f = 0\rangle$ within the $S_{1/2}$ manifold. However, these states are accompanied by six other hyperfine levels, compared to just two for $^{133}Ba^{+}$. This added complexity can introduce additional pathways for error and makes $^{133}Ba^{+}$ a particularly attractive choice for high-fidelity quantum operations.

2. **Visible Wavelength transitions**
   Another attractive feature of $^{133}Ba^{+}$ are the wavelengths needed to manipulate the state of the ion. We can see from Fig. 2.1 that all transitions relevant to quantum information processing except one fall within the visible spectrum. This is highly advantageous due to the easy availability of commercial optical elements. This enables the use of high power lasers, low-loss fibers, high efficiency photon detectors and other optical equipment not typically available to other trapped-ion species, which

ultimately makes things such as individual addressing and photonic networking easier. For comparison, $^{171}Yb^{+}$is another popular species used in trapped-ion systems. However, all the relevant transitions in Ytterbium are in the Ultra-Violet (UV) or near Infrared (IR) which restricts the use of in-fiber optical elements. Higher-energy UV photons are also more likely to charge trap electrodes, particularly in surface-electrode traps, where the laser beams pass within tens of microns of the electrodes.

3. **Long lived metastable states**
   Besides its remarkably simple hyperfine structure, the energy level diagram of $^{133}Ba^{+}$ also includes long-lived metastable states in the D-manifold. In particular, the $5D_{5/2}$ level has an exceptionally long lifetime of approximately 35 seconds, orders of magnitude longer than typical experimental timescales, which are usually on the order of milliseconds. This extended lifetime enables the use of the $5D_{5/2}$ state for shelving operations, long-term state storage, and even as a basis for qubit encoding. It has been demonstrated that shelving the $|F = 1, m_f = 0\rangle$ state into the $5D_{5/2}$ level can improve readout fidelities, particularly in state-dependent fluorescence and mid-circuit measurement schemes [12, 71]. In addition to the standard ground-state (hyperfine) qubit, $^{133}Ba^{+}$ also supports other qubit encodings. These include *optical qubits*, based on the electric quadrupole transition $S_{1/2} \leftrightarrow 5D_{5/2}$, and *metastable qubits*, which can be fully encoded within the long-lived $5D_{5/2}$ manifold. This versatility enables what is known as the Optical-Metastable-Ground (OMG) architecture [3], in which multiple types of qubit encodings coexist within the same ion. Each encoding offers distinct advantages.

All these useful features of $^{133}Ba^{+}$ come with one big disadvantage, which is that it is a manufactured radioactive isotope with a half life of $\tau = 10.5$ years and exposure rate of $\Gamma = 28.564\,\mathrm{mSv\,cm^2\,mCi^{-1}\,hr^{-1}}$ [62]. This means that strict radiation safety protocols have to be followed during the assembly of the system and lead shielding must be installed on the final system to reduce radiation exposure to lab members as much as possible. The other challenge this leads to is the amount of $^{133}Ba^{+}$ that can be used in the system. Due to radiation safety regulation and to minimize exposure, we only use ≤ 0.5 mCi (microgram quantities) in our system. This, along with appropriate shielding and radiation protocols, provides enough radiation protection for the benefits of $^{133}Ba^{+}$ to far exceed its risks.

Ion loading

^{133}Ba is procured in the form of $BaCl_2$ salt. In order to comply with the radiation safety regulations, we use ≤ 5 μg salt in our system. This is a very small amount which makes

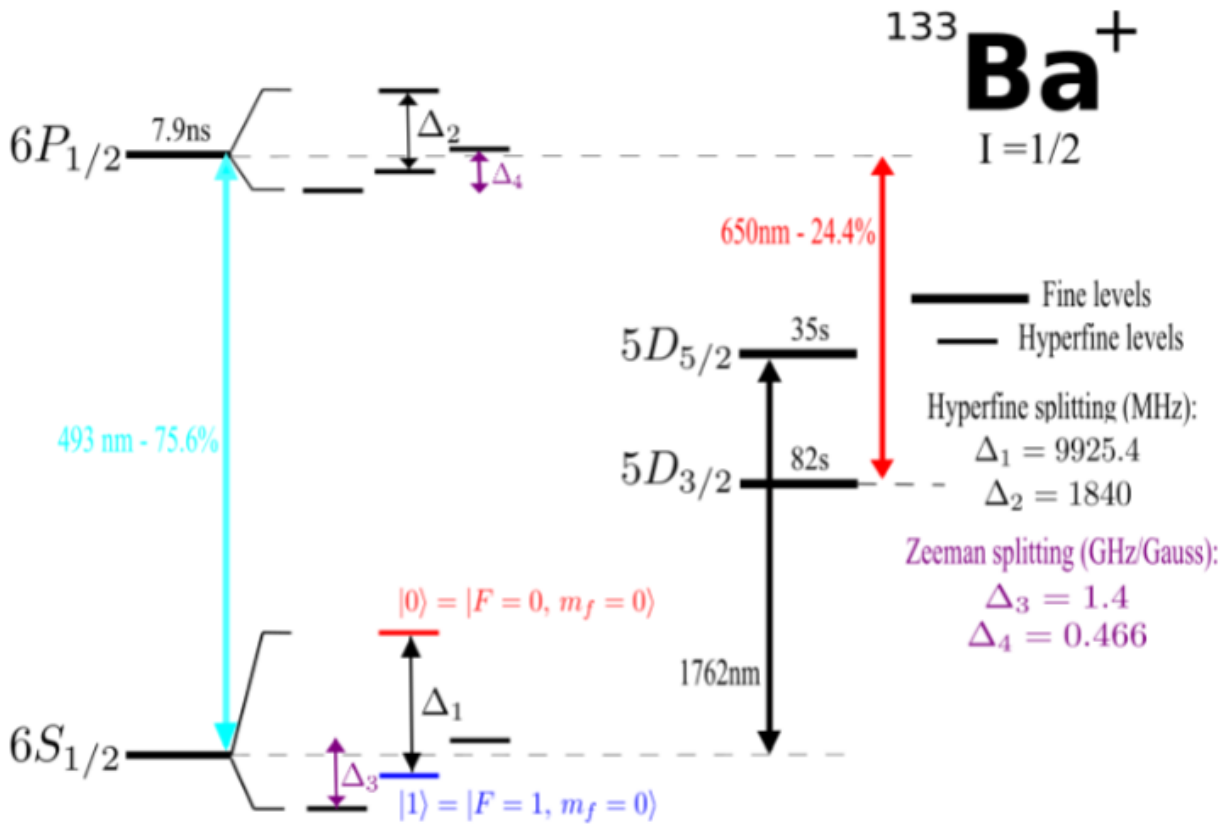


Figure 2.1: Energy level diagram of $^{133}Ba^{+}$ with relevant transitions, branching ratios and splitting (Not to scale). The computational basis states are encoded in the magnetic field insensitive clock states in the $6S_{1/2}$ manifold. All but one relevant transition is in the visible spectrum and the long lived states in the D-manifold with lifetimes of 35 s and 85 s allow for shelving operations. Adapted from [11, 65].

it difficult to reliably produce ^{133}Ba atoms with a high yield using traditional ovens. Traditionally, atoms are produced via resistively heating a bulk sample until neutral atoms are emitted. These ovens do not work for microgram quantities as all of the sample would be vaporized very quickly. This method also works with metallic samples only and to the best of our knowledge there is no commercially available source of metallic ^{133}Ba. Under these constraints, the only viable method to produce ^{133}Ba atoms is laser ablation.

Laser ablation involves shooting a $BaCl_2$ sample with a high intensity pulsed laser. The intense local heating induced by the laser pulse rapidly vaporizes a small section of the sample creating a plume of material directed towards the ion trap. This plume can contain neutral atoms, ions, and any other impurities in the sample depending on the intensity of the ablation laser. This method is much more suitable for a microgram sample as the ablation laser can be focused down to a beam radius in the 10 s of microns range which means a very small amount of material can be ablated in each pulse leading to a much higher yield. It has been shown that Ba^+ atoms can be generated thousands of times via laser ablation from just microgram amounts of $BaCl_2$ [23]. Precise timing control of the laser pulse is also possible through control systems which would give us the ability of producing atoms on demand, compared to the traditional ovens which have much slower heating and cooling cycles on the order of several seconds [4]. Once the neutral atoms reach the trapping region of the ion trap, they are ionized via photoionization and trapped.

The samples procured for ablation targets are never 100% pure, therefore the plume of neutral atoms produced via laser ablation contains a mixture of barium isotopes as well as potential impurities from the ablation target. So, in order to load a specific isotope into the trap, we employ a two-step isotope-selective photoionization scheme depicted in Fig. 2.2. In the first step, a 553 nm laser is used to drive the $6s^2\,{}^1S_0 \leftrightarrow 6s6p\,{}^1P_1$ resonant transition in neutral barium. By slightly modulating the frequency of the 553 nm laser, we can selectively excite the desired isotope due to the isotope shift. Once an electron is excited to the $6s6p\,{}^1P_1$ state, only a small additional amount of energy is required to ionize the atom. A 405 nm laser photon provides more than enough energy to promote this excited electron to the continuum in a non-resonant process, effectively ionizing the atom by removing a valence electron.

These photoionization beams are aligned to intersect at the trapping region of the ion trap, ensuring that ionization occurs only within the trap volume. As soon as a neutral atom is ionized, it becomes subject to the electric fields of the trap electrodes and is confined. The neutral atoms in the ablation plume from $BaCl_2$ travel at speeds on the order of 2500 m/s [70] and disperse in multiple directions. To minimize Doppler shifts during the isotope-selective excitation step, the 553 nm laser is directed perpendicular to the atomic plume whereas the 405 nm laser is parallel to the plume as the second step is

less sensitive to frequency shift.

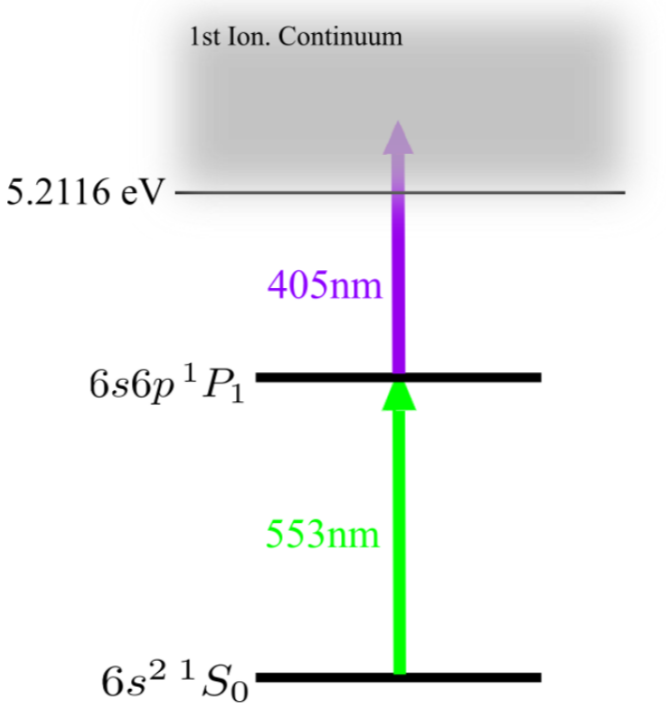


Figure 2.2: Depiction of the two-step isotope-selective photoionization scheme used in the QuantumIon system. The first step excites the 553 nm transition in neutral barium, which can be isotope selective due to the isotope shift. The second step uses a 405 nm laser to drive the electron to the continuum. Figure adapted from [22, 16, 65].

Doppler cooling

When the plume of atoms produced from laser ablation are ionized within the trapping region, they are typically considered "hot" which means they still have high kinetic energy and are moving rapidly. Only a subset of these ionized atoms will have kinetic energy lower than the trap depth of the ion trap and these are the ions that end up getting confined by the electric fields of the trap. Here, the trap depth refers to the difference in total potential energy between the RF null (the center of the trap) and the saddle point of the trapping potential. It represents the maximum kinetic energy an ion can have whilst remaining trapped. However, even the ions that end up getting trapped are still too "hot"

to be used as qubits or be imaged with high resolution as their spatial distribution is too large. Therefore, additional cooling methods are required to reduce their kinetic energy and localize them more tightly within the trap

Doppler cooling is a laser cooling technique used to reduce the kinetic energy of a trapped-ion. It exploits the Doppler effect: ions moving towards the laser source see the laser light blue-shifted, while those moving away see the light as red-shifted. The frequency of the laser is tuned slightly red-shifted from an atomic transition in the ion. When the ion is moving towards the laser, the red-shifted light is brought much closer to resonance, increasing the probability of the ion absorbing a photon. This photon absorption imparts a small momentum kick on the ion in the direction opposite the ions motion which effectively slows the ion down. The ion then spontaneously emits a photon in a random direction. When this process is repeated many times, the momentum change from photon absorption reduces the ion's average velocity, whereas the momentum change from photon emission averages to zero since emission is spontaneous and in random directions. This continuous cycle of absorption and emission leads to a net loss of kinetic energy, thereby cooling the ion.

Fast and efficient Doppler cooling requires an atomic transition that can be rapidly and repeatedly excited, ideally forming a closed cycle. For $^{133}Ba^{+}$, this is provided by the electric dipole transition $6S_{1/2} \leftrightarrow 6P_{1/2}$ at 493 nm which can be seen in Fig. 2.1. The excited state $6P_{1/2}$ has a short lifetime of approximately $\tau_e \approx 8$ ns, enabling rapid photon scattering and effective cooling. However, spontaneous decay from the $6P_{1/2}$ state does not always return the ion to the $6S_{1/2}$ state. There is a branching ratio of about 25% for decay into the long-lived metastable $5D_{3/2}$ state, which has a lifetime of ≈ 82 seconds. Waiting for spontaneous decay back to the ground state would significantly slow the cooling process. To maintain a fast and closed cooling cycle, a 650 nm repump laser is used to drive the $5D_{3/2} \leftrightarrow 6P_{1/2}$ transition. Once in the $6P_{1/2}$ state, the ion can quickly decay back to $6S_{1/2}$, re-entering the cooling cycle. In addition to their role in closing the cooling cycle, the frequencies of the 493 nm and 650 nm lasers must be carefully chosen to avoid coherent population trapping due to the Electromagnetically Induced Transparency (EIT) phenomenon. According to numerical simulations done in Ref. [37], if the detunings of the two lasers are nearly equal ($\Delta_{493nm} \approx \Delta_{650}$), the ion can be optically pumped into a dark superposition of the $S_{1/2}$ and $D_{3/2}$ states in barium, significantly reducing the population in the $P_{1/2}$ state and suppressing fluorescence and hence cooling. The simulation results from Ref. [37] indicate that optimal laser frequencies for maximizing ion fluorescence are dependent on laser intensities and higher laser intensities do not lead to higher fluorescence. Therefore, precise control of both 493 nm and 650 nm laser frequencies is critical for maintaining efficient Doppler cooling and avoiding population trapping.

The lowest kinetic energy, or effective temperature, that can be achieved through Doppler cooling is known as the Doppler limit, which is around 0.5 mK for $^{133}Ba^{+}$. The temperature at the Doppler limit T_{lim} is determined by the natural linewidth of the cooling transition.

$$T_{lim} = \frac{\hbar\Gamma}{2k_b} \tag{2.1}$$

Where Γ is the natural linewidth of the cooling transition. At this limit, ions are sufficiently localized to be imaged with a high spatial resolution, but they remain too "hot" for high-fidelity quantum operations. Such operations require the ion to be cooled near or into its motional ground state. Achieving this level of cooling typically requires more advanced techniques such as Resolved Sideband Cooling (RSC) [13] or EIT [42] cooling.

State preparation and Measurement

State preparation and measurement are among the most fundamental and essential operations in quantum computing, and they are explicitly included in DiVincenzo's criteria for a functional quantum computer [14]. In trapped-ion systems, these operations are typically implemented using optical pumping for state preparation and state-dependent fluorescence for measurement. Optical pumping allows us to initialize the ion in a well defined energy level, typically the ground state which is encoded as $|0\rangle$. With state-dependent fluorescence, a laser is used to selectively excite only one of the qubit states, causing it to emit photons which can be detected with a Photomultiplier Tube (PMT), while the other state remains dark. This state dependent fluorescence allows for high fidelity readout of the qubit state based on whether photons are detected or not. For state preparation and measurement of $^{133}Ba^{+}$, we use the same 493 nm and 650 nm lasers used for Doppler cooling. For state preparation of the $^{133}Ba^{+}$ qubit to the state $|0\rangle$, the 493 nm laser is frequency modulated to excite the ion from $|6S_{1/2}, F = 1\rangle$ to $|6P_{1/2}, F = 1\rangle$. From the $|6P_{1/2}, F = 1\rangle$ state, the ion decays to $|6S_{1/2}, F = 0\rangle = |0\rangle$ effectively populating and initializing the ion in the $|0\rangle$ state. From the excited $|6P_{1/2}, F = 1\rangle$ state, there is still a $\approx 25\%$ chance that ion decays to the metastable $5D_{3/2}$ state. For this the 650 nm laser is also applied during state preparation to pump out any population from the metastable state back to the excited state. Fig. 2.3 shows the energy level diagram of $^{133}Ba^{+}$ with the relevant transitions for state preparation.

State measurement is performed by driving a closed loop transition in the ion that makes it continuously emit photons if it is in one computational basis states and no photons

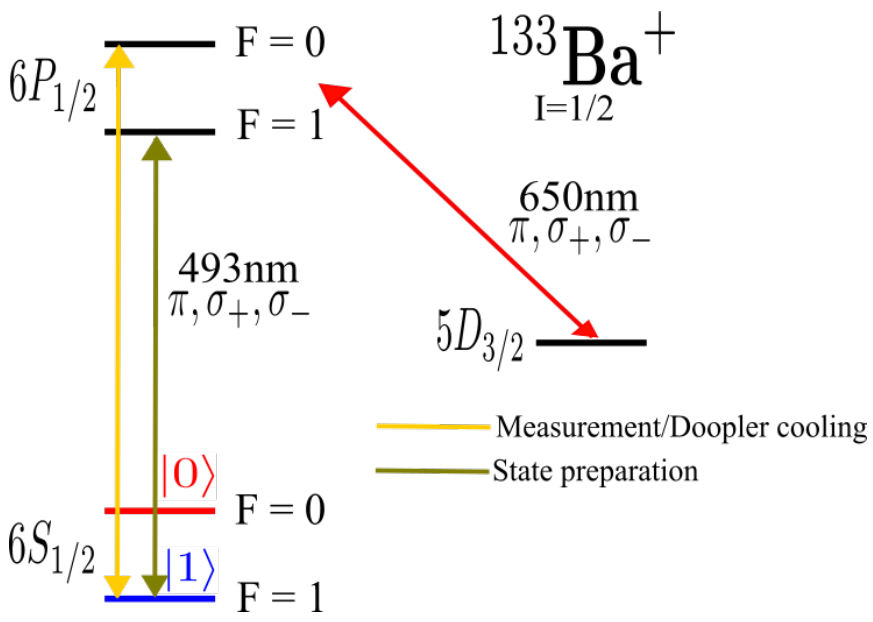


Figure 2.3: Energy level diagram of $^{133}Ba^+$ with transitions relevant to Doppler cooling, and SPAM (Not to scale). The $|6S_{1/2}, F = 1\rangle = |1\rangle \leftrightarrow |6P_{1/2}, F = 1\rangle$ pumps the ion to $|0\rangle$. The cycling transition $|6S_{1/2}, F = 1\rangle = |1\rangle \leftrightarrow |6P_{1/2}, F = 0\rangle$ continually emits photons if the ion is in $|1\rangle$ and remains dark otherwise.

if it is in the other. This is similar to the Doppler cooling procedure, but this time we are modulating the 493 nm laser to drive the $|6S_{1/2}, F = 1\rangle = |1\rangle \leftrightarrow |6P_{1/2}, F = 0\rangle$ transition. The 650 nm laser is again used to pump out population from the metastable state. If the ion is in the state $|1\rangle$ then it will be excited to $|6P_{1/2}, F = 0\rangle$ which can only decay to $|6S_{1/2}, F = 1\rangle$ and not $|6S_{1/2}, F = 0\rangle$ due to the state selection rule that forbids $\Delta J = \Delta m_f = m_f = 0$ transitions. So an ion in $|1\rangle$ will be in a closed cycle and will emit many photons, and an ion in $|0\rangle$ will not emit any photons. Thus, we can discriminate between the two computational basis states by observing if we see any fluorescence from the ion or not. Consequently, $|1\rangle$ is known as the "bright" state and $|0\rangle$ as the "dark" state. This state measurement procedure is depicted in Fig. 2.3.

2.2 Ion traps

Ions, being charged particles, experience forces in the presence of electric fields. This allows, in principle, for them to be confined using carefully designed electric potentials. To

trap an ion in three dimensions using electric fields, the potential must be confining in all spatial directions. A general form for a static electric potential in three dimensions can be written as

$$\phi(x, y, z) = \alpha x^2 + \beta y^2 + \gamma z^2, \tag{2.2}$$

where α, β, γ are constants that determine the curvature of the potential in each spatial direction. However, all electrostatic potentials must satisfy Laplace's equation, which in free space takes the form

$$\nabla^2 \phi = 0. \tag{2.3}$$

Applying this condition to Eq (2.2), we find

$$\alpha + \beta + \gamma = 0. \tag{2.4}$$

This constraint implies that at least one of the coefficients must be negative, meaning the potential is anti-confining in at least one direction. As a result, it is impossible to create a stable trap for a charged particle in all three dimensions using static electric fields alone. This is a direct consequence of Laplace's equation and is formally known as Earnshaw's theorem.

Laplace's equation restricts us from generating a 3D static potential minimum. However, it is possible to generate a static potential in the shape of a hyperbolic paraboloid, commonly referred to as a saddle potential. If we set $\alpha = -1, \beta = 1, \gamma = 1$ in Eq (2.2) then Laplace's equation is satisfied, and we get a saddle potential as shown in Fig. 2.4. Near the saddle point, the potential is confining in one direction and anti-confining in another, which means an ion near the saddle point would accelerate away along the anti-confining direction. However, if the roles of the confining and anti-confining directions are switched rapidly and periodically, before the ion has time to escape, the ion can be effectively confined near the saddle point. This is achieved using oscillating electric fields and forms the basis of RF trapping as the required drive frequencies typically lie in the RF range. These oscillating fields, when averaged over time, give rise to a net confining force described by a pseudopotential which enables stable ion trapping.

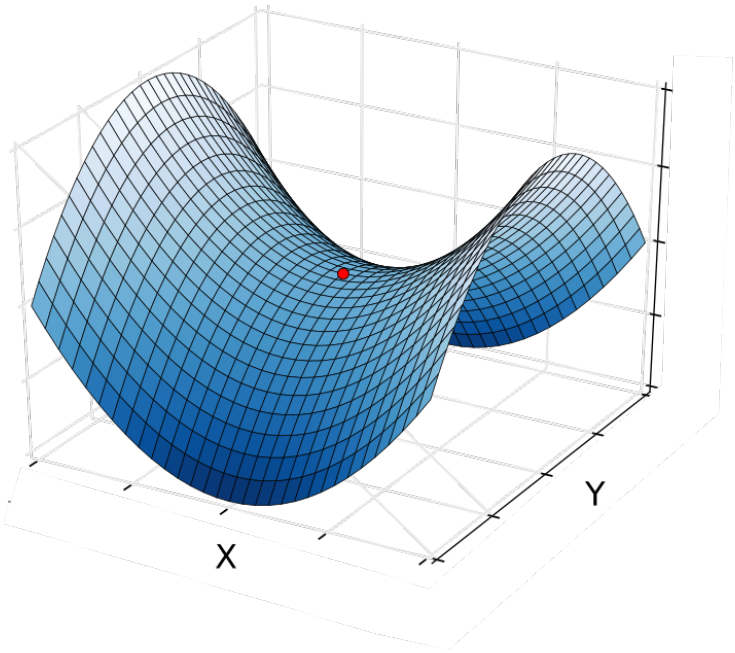


Figure 2.4: Plot of a saddle potential using Eq. 2.2 with $\alpha = -1$, $\beta = 1$, $\gamma = 1$. The potential is confining in the x direction and anti confining in the y direction. The confining and anti-confining directions are swapped before the ion has a chance to escape. The saddle point is shown in red. Adapted from [45].

2.2.1 4-rod linear Paul trap

The following explanations and derivations are based on the approaches presented in [6, 36, 15]. A confining potential based on oscillating electric fields can be realized using a Paul trap [48, 47], named after its inventor Wolfgang Paul, who was awarded the Nobel Prize in Physics in 1989 for this work. The Paul trap uses a combination of static and rapidly oscillating electric fields to create an effective potential that confines ions in free space.

Linear Paul traps are the most commonly used version of the Paul trap. A version of the linear paul trap is the 4-rod trap which consists of 4 rod-shaped electrodes in a quadrupole configuration, with the rods arranged around the trap center. An oscillating RF voltage V_{RF} is applied to two diagonally opposing electrodes, while the other two are held at ground potential.

$$V_{RF} = V_0 \cos(\Omega_{RF} t) \tag{2.5}$$

where V_0, Ω_{RF}, t are the RF voltage amplitude, RF drive frequency and time, respectively. For axial confinement, two needle electrodes are used that receive a static DC voltage U_0. The directions from the trap center where the trapped ion sits to the RF electrodes are generally referred to as the radial directions, and the direction along the two needle electrodes is known as the axial direction. In this thesis, the x and y axes will be the radial directions, and the z-axis will be the axial direction, also known as the trap axis. Fig. 2.5 shows the diagram of a 4-rod linear Paul trap. The potential can be decomposed into a time-independent static DC part and a time-dependent RF part that varies sinusoidally at the RF drive frequency Ω_{RF}

$$\phi = \frac{U_0}{2}(\alpha x^2 + \beta y^2 + \gamma z^2) + \frac{V_0}{2}(\alpha' x^2 + \beta' y^2 + \gamma' z^2)\cos(\Omega_{RF} t) \tag{2.6}$$

where the coefficients are geometric factors and must satisfy $\alpha+\beta+\gamma = \alpha'+\beta'+\gamma' = 0$ for the potential to satisfy Laplace's equation. For the 4-rod trap shown in Fig. 2.5, the DC and RF potentials are

$$\phi_{DC}(x, y, z) = \frac{\kappa U_0}{Z_0^2}[z^2 - \frac{1}{2}(x^2 + y^2)] \tag{2.7}$$

$$\phi_{RF}(x, y, z, t) = \frac{V_0}{2}\left(1 + \frac{x^2 - y^2}{R'^2}\right)\cos(\Omega_{RF} t) \tag{2.8}$$

where R is the perpendicular distance from the trap axis to the rod electrodes as shown in Fig. 2.5 [$R = R'$ if the rod electrodes are hyperbolic cylinders of infinite length], Z_0 is the distance from the tips of the needle electrodes to the trap center and κ is a geometric factor.

We can then obtain the classical equations of motion for an ion in this confining potential. These equations are cast into the form of the well-studied Mathieu differential equations whose solutions are already known. For a single ion of mass m and charge Q, we get the following Mathieu equation.

$$\ddot{u}_i + [a_i + 2q_i \cos(\Omega_{RF} t)]\frac{\Omega_{RF}^2}{4} u_i = 0 \tag{2.9}$$

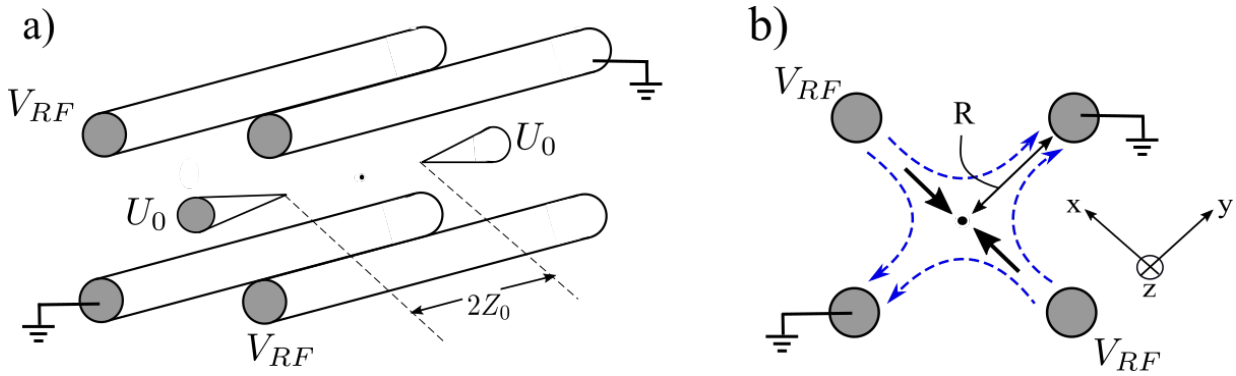


Figure 2.5: Schematic of a 4-rod linear Paul trap (Not to scale). a) Oblique angle view of a 4 rod trap. V_{RF} is applied to a pair of diagonal electrodes and the other two are grounded for confinement along x and y-axis (radial). Two needle electrodes receive a static DC voltage U_0 for confinement along the z-axis (axial direction or the trap axis). b) Shows a end-view of the trap with the needle electrodes omitted. The dashed blue lines show the electric fields generated by the electrodes. This configuration generates a quadrupole pseudopotential with a minimum known as the RF null in the center of the trap marked by the black dot. Adapted from [65].

where $\mathbf{u} = u_x\hat{x} + u_y\hat{y} + u_z\hat{z}$ is the position of the ion based on the coordinate system shown in Fig. 2.5 which decouples Eq (2.9). The axes along which the ion's motion is decoupled in the three spatial directions are known as the principle axes of the trap.

$$a_x = a_y = -\frac{1}{2}a_z = -\frac{4Q\kappa U_0}{mZ_0^2\Omega_{RF}^2} \tag{2.10}$$

and

$$q_x = -q_y = \frac{2QV_0}{mR'^2\Omega_{RF}^2} \tag{2.11}$$

Here a_i, and q_i represent the influence of the static DC field and time-varying RF field, respectively. Stable trapping of an ion only occurs in specific regions of the $a-q$ parameter space called the stability region.

In the typical case where $|q_i| \ll 1$ and $|a_i| \ll 1$, the first order solution to equation (2.9) is

$$u_i(t) \approx u_{1i} \cos(\omega_i t + \varphi_{\mathcal{S}i}) \left(1 + \frac{q_i}{2} \cos(\Omega_{RF} t)\right) \tag{2.12}$$

Phase $\varphi_{\mathcal{S}i}$ is determined by the initial position and velocity of the ion. The first term in Eq. (2.12) corresponds to a slower component of the motion, referred to as "secular" motion. When this term dominates, the dynamics of the ion can be approximated by that of a harmonic oscillator with frequency $\omega_i \cong \frac{1}{2}\Omega_{RF}\sqrt{a_i + \frac{1}{2}q_i^2}$ (known as the secular frequency) and amplitude u_{1i}. The second term, driven directly by the applied RF field, describes a faster oscillation at the RF drive frequency Ω_{RF}, known as "micromotion". An example of ion motion according to Eq. (2.12) is shown in Fig. 2.6. Typically, when trapping more than one ion, confinement along the axial direction is made significantly weaker than that in the radial (x and y) directions by adjusting the trap voltages. This results in a lower secular frequency along the z axis such that $\omega_x, \omega_y \gg \omega_z$. The resulting asymmetry in confinement causes the ions to align along the axial direction, forming a linear chain.

2.2.2 Surface-electrode traps

The 4-rod trap is one of the earliest implementations of a linear Paul trap. Over the years, various other ion trap architectures have been developed, including ring traps, blade-style traps, and microfabricated traps with multilayer electrode structures [61, 64]. In 2005, a surface mounted electrode geometry for miniature linear Paul traps was proposed [10], which has since gained significant popularity and is now commonly referred to as a surface-electrode trap.

Unlike traditional 3D electrode configurations, such as the one shown in Fig. 2.5, surface-electrode traps employ a planar architecture in which all electrodes are confined to a single surface. One can imagine the four cylindrical electrodes of a traditional 4-rod Paul trap being "unrolled" and flattened into a planar geometry, as illustrated in Fig. 2.7 a). A conceptually simple design approach for this is the so-called five-wire geometry [10] shown in Fig. 2.7 b). In this surface-electrode configuration, one of the ground electrodes is positioned at the center, flanked on both sides by RF electrodes. The second ground electrode is effectively split into two parts, each placed on either side of the RF electrodes. This layout provides radial confinement, with the potential minimum located a certain distance above the central ground electrode, as indicated by the electric field lines in Fig. 2.7 c). Axial confinement is achieved by segmenting the outermost ground electrodes and applying static DC voltages to them, as shown in Fig. 2.7 b). These segmented DC electrodes

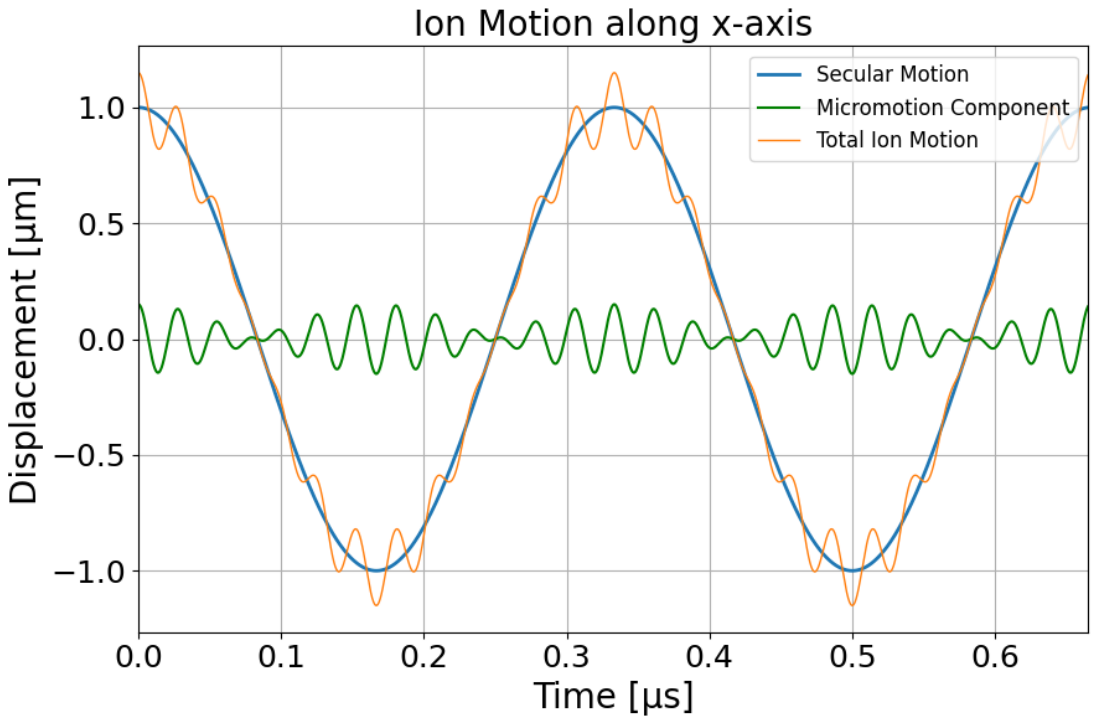


Figure 2.6: Simulated trajectory of a trapped ion according to Eq. (2.12). The plot shows the secular motion (blue), the micromotion component (green), and the total motion (thin orange). The secular motion corresponds to harmonic oscillations at the secular frequency $\omega_x = 2\pi \times 3\,\mathrm{MHz}$, with an amplitude $u_{1i} = 1\mu\mathrm{m}$. The micromotion arises from the RF drive at frequency $\Omega_{RF} = 2\pi \times 36\,\mathrm{MHz}$, with a Mathieu parameter $q_i = 0.3$.

serve the same function as the needle electrodes in a conventional 4-rod Paul trap, enabling confinement along the trap axis.

Surface-electrode traps offer several advantages over traditional 4-rod Paul traps, especially in the context of scalability and system integration. With all of the electrodes being in one plane, surface-electrode traps can be manufactured using techniques developed for the microelectronics industry like patterned metal deposition and photolithography. Using established microfabrication techniques, it is possible to produce much smaller ion traps with finer feature sizes and greater reproducibility, reducing the susceptibility to manufacturing defects compared to traditional hand-assembled traps. Microfabrication allows for the production of traps that adhere precisely to the intended design. This not only

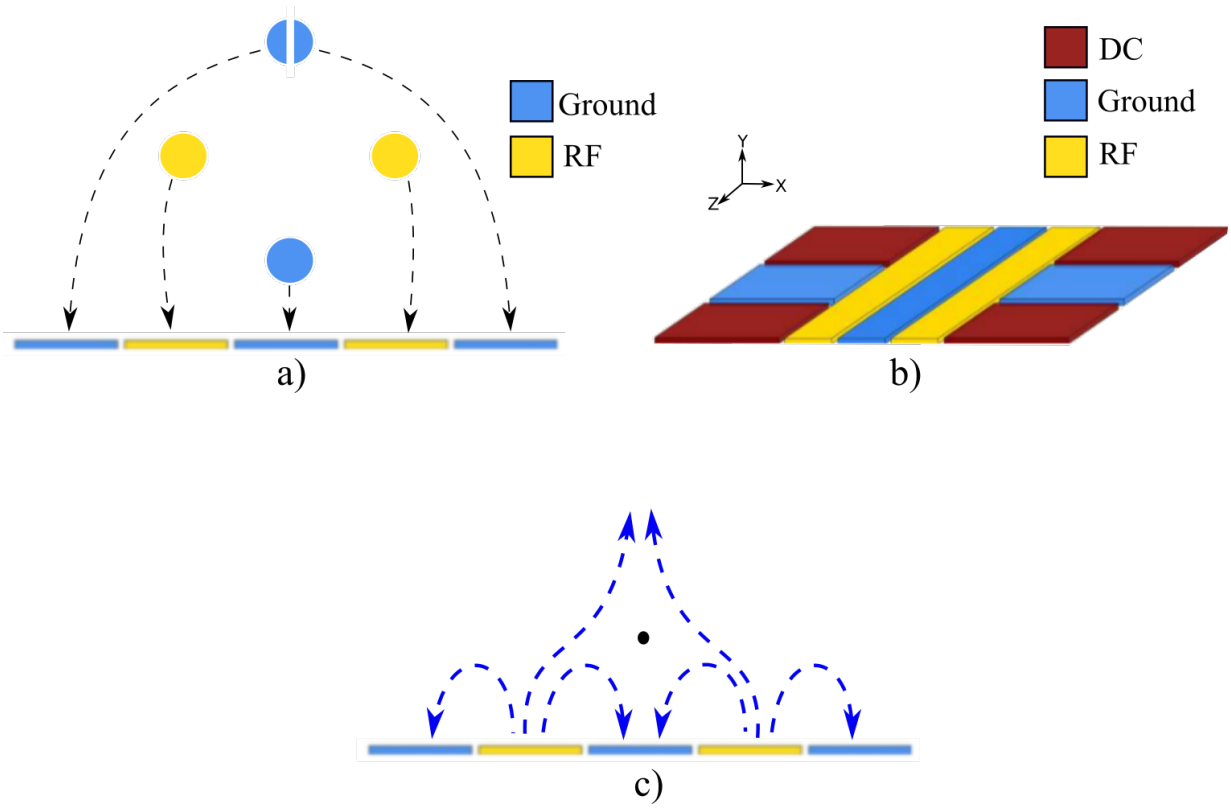


Figure 2.7: Schematic of a five-wire surface-electrode trap. a) Illustration of how a surface-electrode trap is essentially a "unrolled" 4-rod trap. b) Shows the five wire design with the DC electrodes in maroon for axial confinement. c) Shows the confining electric field lines generated by a surface-electrode trap. The potential minimum lies a certain distance above the trap. Adapted from [49].

allows for the fabrication of identical traps, but also results in highly predictable trapping potentials based on electrostatic models. The five-wire design shown in Fig. 2.7 contains four DC electrodes for axial confinement, however, modern surface-electrode traps can incorporate close to 100 independently controlled DC electrodes [54], enabling fine grained shaping of the axial potential. This level of control is essential for several key features:

1. **To achieve uniform ion spacing in a linear chain, a precisely tailored axial potential is required.** Equal ion spacing is crucial for individual optical addressing (a key feature of the QuantumIon system), minimizing cross-talk between qubits during laser-driven gate operations

2. **A precise and dynamically adjustable axial potential is required to shuttle ions between different regions of the trap.** This capability is essential for realizing the Quantum Charge-Coupled Device (QCCD) architecture [32], in which ions are transported between dedicated zones for computation, memory, and readout. Implementing such an architecture requires complex electrode geometries, including junctions, loading zones, and transport channels, which are only feasible using microfabrication techniques. This makes surface-electrode traps a natural platform for supporting the QCCD model of scalable trapped-ion quantum computing. Significant progress has been made towards realizing this architecture [40, 50, 7, 54]

Despite these advantages, surface-electrode traps also present several challenges. Compared to a four-rod Paul trap, surface-electrode traps have relatively shallow trap depths [10], typically on the order of 0.1–0.2 eV, which is only slightly above the mean kinetic energy of neutral atoms prior to ionization [57]. This can make it very difficult to trap highly energetic atoms such as those produced via laser ablation. Once trapped, the ions are more susceptible to escape and environmental perturbations. In addition to this, the planar geometry of surface-electrode traps inherently places the ions just tens of micrometers above the electrode surface, much closer than traditional 3D geometries- leading to significant motional heating rates due to electric field noise and surface related effects such as patch potentials [10, 66].

Practical issue further complicate the operation and reliability of surface-electrode traps. The larger number of DC electrodes requires a significantly more complex control system. Additionally, laser beam clipping on the trap electrodes can lead to charge build up due to photoelectric charging and a lower signal to noise ratio during state measurement. The close spacing between microfabricated electrodes, often on the order of a few microns, also increases the risk of electrical shorts during system assembly and contamination from laser ablation. Nevertheless, the potential for integration and scalability

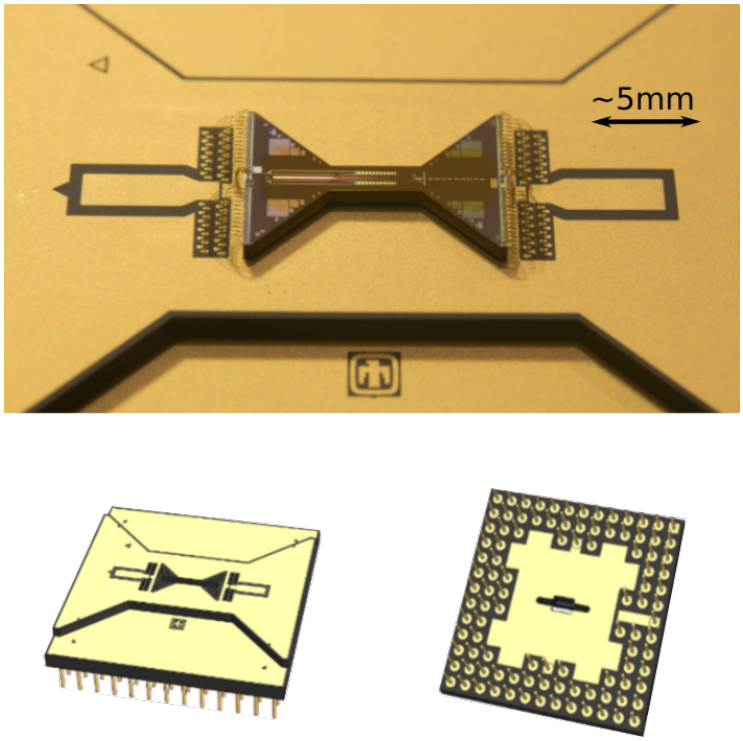


Figure 2.8: Close-up image of the Phoenix trap (Top) and CAD rendering of the trap CPGA (bottom). The bowtie shape of the trap gives high optical access by allowing beams to come from the vertical direction in the image above without clipping on the trap surface. The CPGA resembles a computer CPU with the trap on one side and connection pins on the other. Images taken from [54].

offered by the surface-electrode architecture continues to outweigh these difficulties. Several research groups have successfully demonstrated ion trapping, shuttling and quantum operations in microfabricated surface-electrode traps [57, 50]. For the QuantumIon project, we have chosen to use the Phoenix surface-electrode trap, developed by Sandia National Laboratories, which addresses many of these challenges while providing the advanced features needed for our 16-qubit quantum processor.

The Phoenix trap

The QuantumIon project uses the Phoenix trap [54] designed and fabricated by Sandia National Labs. Fig 2.8 shows a close up image of the trap and a rendering of the trap

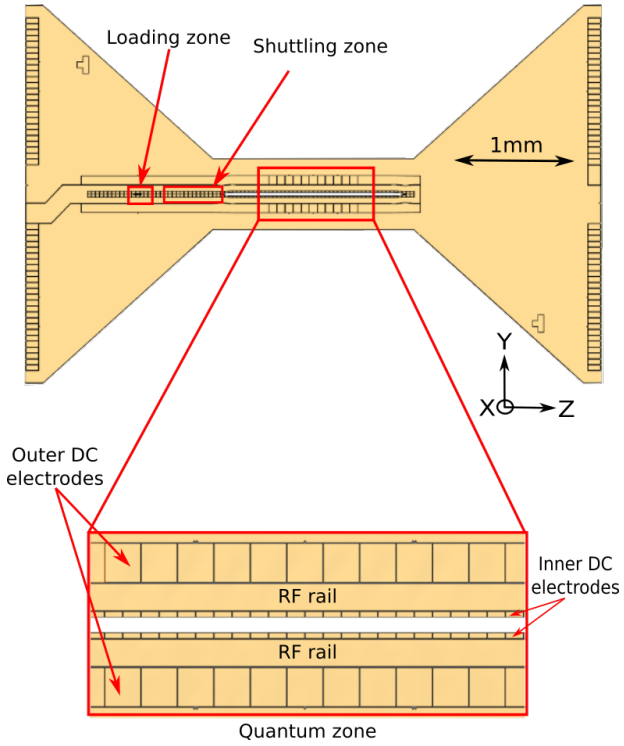


Figure 2.9: Electrode layout of the Phoenix trap with trap zones labeled. The quantum zone shows a close up of the symmetric six-rail design. Adapted from [54].

CPGA. A SEM image of the trap is shown in Fig. 2.10. The trap is built on Sandia's bowtie HOA platform [40] optimized for laser beam access that skims across or even passes through the trap surface.

The trap features a symmetric six-rail electrode layout with segmented inner and outer DC control electrodes for precise shaping of the axial potential and micromotion compensation. Radial confinement is achieved with an RF rail electrode that stretches the entire length of the trap. Fig. 2.9 shows a schematic of the electrode layout. There are a total of 88 DC control channels going to the trap which control a total of 152 DC electrodes. The trap comprises of three zones, a quantum zone, a loading zone and a shuttling zone. The quantum zone is in the center of the trap and is where all quantum login operation are to take place. This zone has 22 inner and 11 outer pairs of DC electrodes. The loading zone is where the ions are first trapped, its purpose is to hold a reservoir of ions which can be shuttled to the quantum zone when needed. The shuttling zone allows shuttling the ions between the quantum and loading zone. These zones are highlighted in Fig. 2.9.



Figure 2.10: SEM image of the Phoenix trap. The wire bonds making the electrical connections from the trap to the CPGA are kept away from the quantum zone to prevent laser beams clipping on them. Image taken from [54].

The trap is packaged on a High-Temperature Co-fired Ceramic (HTCC) Aluminum Nitride custom bowtie shaped package integrated onto a CPGA giving it a form factor reminiscent of a conventional computer processor. Additional features of the Phoenix trap include an RF sense line for monitoring the RF voltage applied to the trap, as well as integrated resistive elements used for substrate heating and temperature sensing. With its six-rail electrode geometry, the trap is designed to confine ions approximately 68 μm above the trap surface

2.3 Summary

In summary, the properties of the $^{133}Ba^{+}$ qubit were reviewed, highlighting how its favorable atomic structure makes it an excellent candidate for high-fidelity quantum operations. The challenges associated with the radioactivity of $^{133}Ba^{+}$, particularly its impact on ion loading methods, were discussed, emphasizing the necessity of laser ablation for ion generation. Conventional ion trapping experimental techniques, including Doppler cooling and SPAM, were also covered. This chapter established the foundations for understanding the QuantumIon trapped-ion quantum processor.

The trapping of charged particles using RF fields was discussed. The equations of motion for a charged particle in a four-rod linear Paul trap were derived, demonstrating how an ion undergoes a fast micromotion superimposed on a slower secular motion. Following this, the surface-electrode ion trap architecture was described along with its advantages for scaling up trapped-ion systems. Finally, the Phoenix trap and its key features were introduced.

Chapter 3

QuantumIon Vacuum chamber setup

This chapter describes the design of the QuantumIon vacuum chamber that houses the Phoenix trap. A UHV environment is needed for stable trapping of atomic ions to reduce disruptive collisions of the trapped ion with background gases. The design of the vacuum chamber in trapped-ion systems is a very important factor as low vacuum pressures directly affects the lifetime of trapped ions which directly affect how long a quantum simulation experiment can be conducted for. The chamber design also determines the optical access available to the ions for controlling the ion's state and ion-ion coupling. High optical access is necessary for addressing individual ions with minimal crosstalk on neighboring ions, which is essential for implementing precise gate operations and tunable interactions between qubits. Section 3.1 motivates the necessity of UHV pressures in trapped-ion systems and section 3.2 describes how our vacuum chamber is specifically designed to achieve low UHV pressures and HOA by mounting the surface-electrode trap at the center of the chamber, instead of a conventional flange mounted design.

The QuantumIon vacuum chamber was designed by former PhD student Dr. Noah Greenberg, with comprehensive details available in their master's and doctoral theses [21, 22]. The author was not involved in the original design process. This chapter provides an overview of the vacuum chamber design to familiarize the reader with its features, as they are relevant to and complement the content discussed in subsequent chapters

3.1 UHV for trapped-ions

A UHV environment is required for trapping an ion or a long chain of ions. This requirement is necessary to ensure that the probability of the ions colliding with background gases

is greatly reduced. Collisions with background gas molecules can disrupt the ion chain by inducing reordering events, melting the ion chain or ejecting ions from the trap altogether [46, 2]. Increased background collisions not only raises the rate of collision-induced motional heating via RF coupling [9, 46], but also accelerates the buildup of monolayers on electrode surfaces, which are known to enhance electric-field noise and increase heating rates. These events necessitate re-cooling or even reloading of the ions, halting experimental sequences and leading to significant downtime.

UHV environments refer to vacuum vessels with base pressures in the range $10^{-9} - 10^{-12}$ mbar. Room temperature ion trap systems typically operate at pressures in the low 10^{-11} mbar range which is sufficiently low to suppress background gas collision rates to minimize ion chain reordering events and loss of ions from the trap [2]. At $\approx 1.33 \times 10^{-11}$ mbar the background gas collision rate for a single trapped-ion was estimated in Ref. [39] using the Langevin collision model [46, 26] and found to be on the order of one collision per hour. Typical data acquisition times in quantum simulation experiments can range from several minutes to tens of minutes. Moreover, the collision rate is expected to scale approximately linearly with the number of ions in the chain, making the system increasingly vulnerable as it scales. This imposes even more stringent vacuum requirements on multi-ion systems, such as the QuantumIon system. These considerations highlight the critical importance of reaching and maintaining UHV conditions in trapped-ion platforms.

This UHV requirement becomes even more stringent in the QuantumIon system due to the radioactivity of the $^{133}Ba^{+}$ ions used. As discussed in Section 2.1.1, we are restricted to using only microgram quantities of $BaCl_2$ salt due to radiation safety regulations. Although laser ablation enables the loading of Barium ions thousands of times from only microgram quantities of $BaCl_2$ salt [22], it remains highly desirable to minimize the frequency of ion loading for the following reasons:

1. **Loss of sample during $BaCl_2$ deposition and chamber assembly.** We used an in-house developed procedure to prepare ablation targets with microgram quantities of $BaCl_2$ salt [22]. A significant portion of the material can be lost during both the preparation of these targets and their installation into the vacuum chamber. Due to the extremely small quantities involved, it is challenging to accurately measure how much salt is lost in this process. As a result, we must be conservative with how frequently we ablate the surface to avoid prematurely exhausting the available material.

2. **Low loading rates in surface-electrode traps**. As discussed in section 2.2.2, surface-electrode trap suffer from lower traps depths which significantly decreases

the probability of successfully loading ions into the trap. Ablation loading rates for Ba^+ ions in a surface-electrode trap were measured to be on the order of 1 ion trapped per 100 ablation pulses [59]. The loading rates measured in Ref [59] are for ablation targets made with metallic barium. For microgram quantity $BaCl_2$ ablation targets, the loading rate is expected to be much lower as the speed of neutral atoms generated from salt targets are much faster compared to metal ones. Therefore, we expect to require hundreds of ablation pulses to successfully trap ions from the $BaCl_2$ targets, which could quickly deplete the already limited supply of material

3. **Contamination of trap electrodes**. A plume of neutral atoms, ions, and impurities is ejected from the ablation target during each ablation pulse. This plume is directed toward the trapping region, and any material it contains can potentially deposit on nearby trap components, including the electrodes. Such contamination poses multiple risks. In severe cases, it can lead to electrical shorts between adjacent electrodes, rendering parts of the trap inoperable. Even when shorts do not occur, deposited contaminants can result in charge build-up on or near the electrode surfaces. This can distort the local trapping fields, introduce stray electric fields, and lead to increased motional heating rates of the trapped ions, ultimately degrading experimental performance.

The three points outlined above highlight the importance of retaining trapped-ions as long as possible to minimize the frequency of loading events. Achieving long ion lifetimes requires reducing the vacuum pressure to the lowest possible level, thereby minimizing collisions with background gas molecules, which are a primary cause of ion loss from the trap.

3.2 QuantumIon vacuum chamber setup

An image and schematic of the QuantumIon vacuum system is shown in Fig. 3.2. The system can be divided into 3 parts. A top chamber, known as the diagnostic chamber, the five-way cross, and the bottom chamber which we call the experimental chamber. The experimental chamber is the part that houses the surface-electrode trap and ablation targets.

The design of vacuum chambers for trapped-ion systems is primarily driven by need to achieve UHV pressures and providing sufficient optical access to the ions for performing quantum operations, such as state preparation, measurement, and quantum gates. Accordingly, the QuantumIon vacuum system was engineered to reach UHV conditions while

maximizing optical access. This enables the individual addressing of a 16-ion chain with minimal crosstalk and efficient collection of fluorescence during state readout.

One significant modification in the QuantumIon system concerns the mounting of the surface-electrode trap within the vacuum chamber. Traditionally, surface-electrode traps are mounted directly onto one of the chamber flanges, as illustrated in Fig. 3.1. Modern surface-electrode traps, which can have on the order of 100 DC electrodes, require a correspondingly large number of electrical connections. Routing such a high density of electrical connections into a UHV environment is challenging, as outgassing from the connections can increase the gas load inside the chamber, thereby degrading the vacuum pressure [21]. To mitigate this issue, most surface-electrode trap systems mount the trap directly on a chamber flange to minimize the complexity and length of electrical connections inside the vacuum chamber. However, mounting the surface-electrode trap directly on a flange imposes significant limitations on optical access. In such a configuration, positioning the trap close to the chamber walls restricts the angles at which laser beams can be delivered through surrounding viewports, as they must be aligned to avoid clipping on the electrodes or chamber structure. This can make it more difficult to achieve the precise beam geometries required for individual ion addressing and optimal fluorescence collection. Mounting the surface-electrode trap directly onto a flange typically requires custom-made flanges which may be more prone to leaks compared to standard, industry-tested vacuum flanges. Additionally, regions near the chamber walls often have reduced pumping conductance due to geometric constraints, such as narrow or obstructed pathways for gas flow. As a result, the local pressure near the trap can be higher compared to the center of the chamber, where there is typically better conductance to the pumping ports. Therefore, the flange mounted design not only restricts optical access, but also degrades the vacuum pressures.

3.2.1 The experimental chamber

To alleviate the issues of the flange mounted design, the QuantumIon system mounts the surface-electrode trap in the center of the vacuum chamber. Fig. 3.3 shows a schematic of the experimental chamber and how the surface-electrode trap is mounted centrally inside it. The trap is suspended in the geometric center of the chamber with optical access from the side and bottom. The experimental chamber consists of 8 viewports (3 re-entrants). The design of this experimental chamber was primarily driven around maximizing the NA for the Raman individual addressing beam (~ 0.37) and the numerical imaging aperture (~ 0.6).

A high NA is needed to be able to focus down the individual addressing beams as tightly as possible to mitigate crosstalk between beams addressing neighboring ions in an

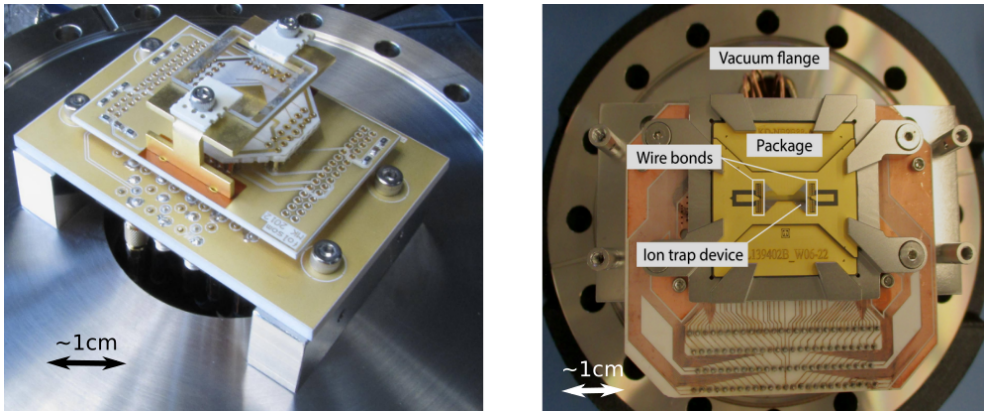


Figure 3.1: Two implementations of a flange mounted surface-electrode trap design. The trap being mounted onto a chamber flange makes electrical connections to the trap much less complex. Left image taken from [35] and right image from [25].

ion chain. The QuantumIon system uses a 532 nm mode locked pulsed laser to drive Raman transitions for coherent control of the $^{133}Ba^{+}$ qubits which are defined in the hyperfine clock states in the $S_{1/2}$ manifold (Fig. 2.1). With a NA of 0.37, the diffraction-limited spot size for 532 nm light is approximately 0.7 μm . In our system, the equilibrium spacing between ions in the chain was designed to be around 4 μm, which represents an optimal balance: it is small enough to ensure strong motional coupling between ions for high-fidelity two-qubit gates, yet large enough to allow individual optical addressing of ions with minimal crosstalk due to diffraction-limited beam focusing. Thus, the 0.37 NA of the Raman re-entrants allows for the quantum state of one ion to be manipulated without affecting that of the others.

A high NA is also required for the imaging system which is located at the bottom of the experimental chamber. This system is used to image the ions and collect ion fluorescence during state readout. The NA of the imaging re-entrant window directly determines the photon collection efficiency of the system. A higher NA increases the solid angle over which spontaneously emitted photons from the ions can be collected, thereby improving the signal-to-noise ratio and reducing state detection time. The experimental chamber also features four viewports to provide optical access at 45° relative to the trap axis (ion chain axis) for Doppler cooling (493 nm), repumping (650 nm) and photoionization (553 nm, 405 nm). Both the Raman and imaging viewports are re-entrants, meaning they are recessed into the vacuum chamber. This is essential for achieving the high NA as it allows for objective lenses to be brought into close proximity of the ions.

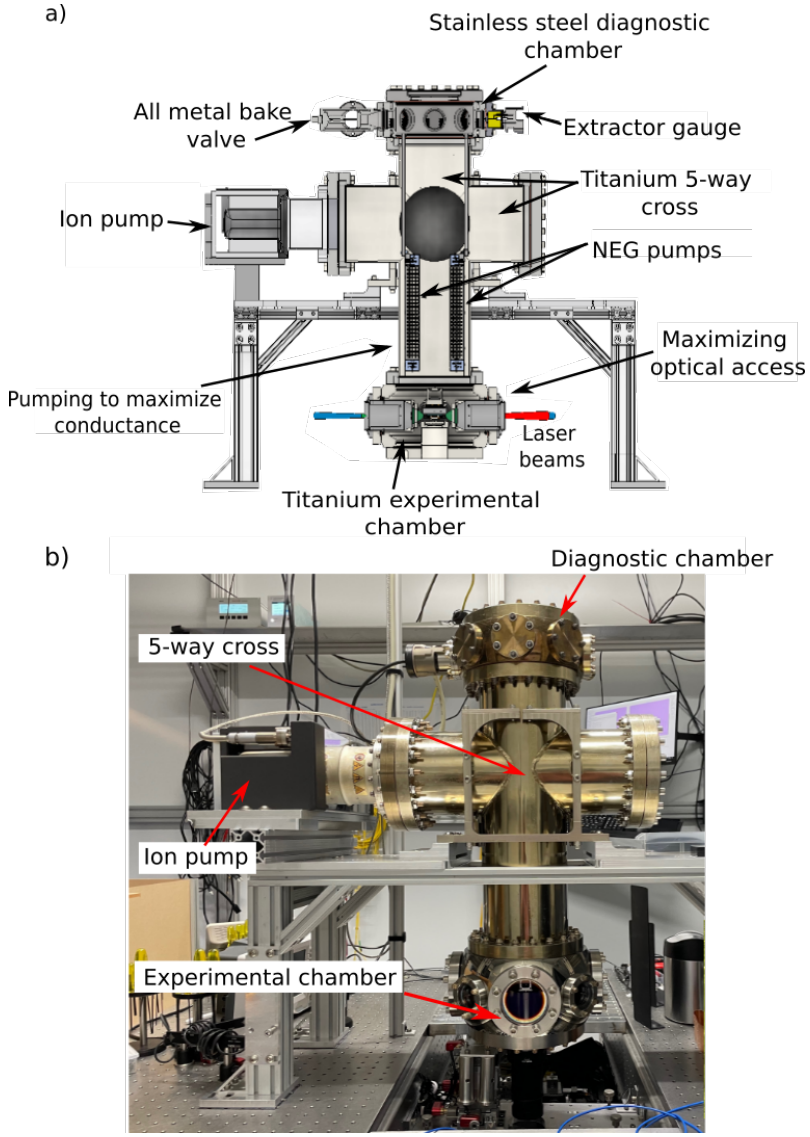


Figure 3.2: Schematic and image of the QuantumIon vacuum chamber. a) Internal cross-section view of the QuantumIon vacuum chamber. There are three main sections, the diagnostic chamber, the five-way cross and the experimental chamber. The view also shows where the ion pump and NEG pumps are connected on the chamber. b) Picture of the actual chamber in our lab. The experimental chamber houses the trap and is located at the bottom of the system directly above a valley in the optics table. We call this the imaging valley as it contains all the optics for imaging ions through the 0.6 NA re-entrant at the bottom of the experimental chamber. Adapted from [22].

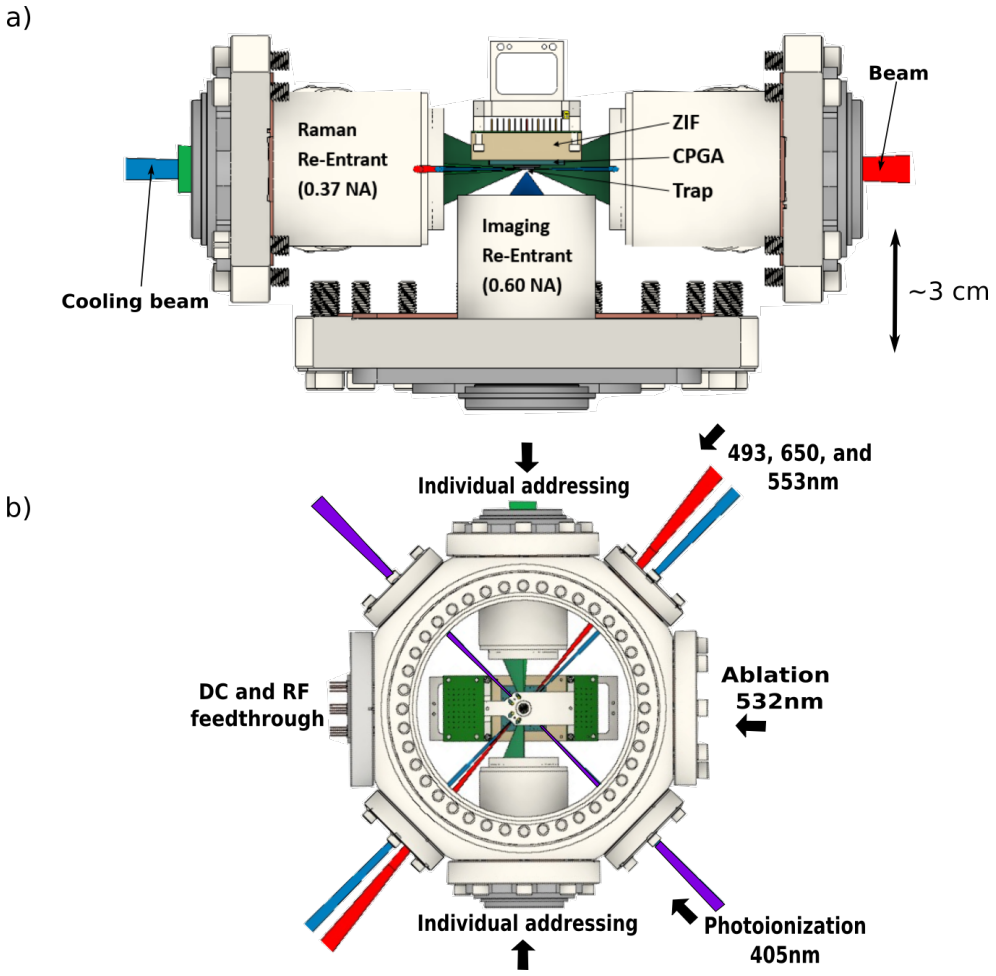


Figure 3.3: Schematic of the experimental chamber that house the surface-electrode trap and atomic sources. a) The trap is mounted in the geometric center of the chamber. The high NA re-entrants allow high optical access to the trap. b) Bottom view of the experimental chamber. The Raman individual addressing beams enter from the high NA re-entrants where as the 493, 650, 553, and 405 nm lasers enter from view ports on the diagonals of the chamber. The DC and RF electrical connections to the trap enter the vacuum chamber through an electrical feed-through. Adapted from [22].

Thus, by mounting the trap at the center of the chamber, we are able to achieve significantly improved optical access and lower vacuum pressures at the trapping region. However, this configuration does increase the complexity of routing electrical connections to the trap. To address this, we developed a custom in-house, UHV-compatible wire harness that enables reliable electrical interfacing with the centrally mounted trap. The implementation of this harness is detailed in Chapter 6 of this thesis.

3.2.2 The diagnostic chamber

The diagnostic chamber is a stainless steel octagon mounted at the top of the vacuum system. Its primary function is to provide an area of high conductance for attaching pressure gauges, a all metal bake valve and residual gas analyzer. The pressure of the chamber is measured with an extractor gauge that can measure from High-Vacuum (HV) to extreme high vacuum ($10^{-4} - 10^{-13}$ mbar). A Residual Gas Analyzer (RGA) is used to measure the partial pressure of the gases present in the system and is primarily used to diagnose problem with the vacuum system. One of its main uses is to detect leaks on the vacuum chamber flanges by spraying helium on the flanges from the outside. The all metal bake valve is used to connect the chamber to an external turbomolecular pump that is used to pump the chamber down to HV pressures ($\approx 10^{-5}$ mbar). Chamber pressures above 10^{-4} mbar were measured using the internal gauge of the turbomolecular pump.

3.2.3 The five-way cross

The five way cross consists of 5 ports, one for the diagnostic chamber, one for the experimental chamber, one to attach the ion pump at the side and two redundant ports. The five-way cross houses all the vacuum pumps required to reach and operate at UHV pressures. Its geometry is designed to maximize conductance between the experimental chamber and the pumps, thereby increasing the effective pumping speed. The ion pump is primarily used to remove non-getterable gases, such as noble gases, which are not efficiently captured by Non-Evaporable Getter (NEG) pumps. It operates by ionizing residual gas molecules and accelerating them into titanium cathodes, where they are either buried or chemically bonded to the surface, effectively removing them from the vacuum chamber. The other pump which is present inside the five-way cross are the NEGs. A NEG pump removes gases from the vacuum system by chemically binding them to a reactive metal or alloy surface. The NEG pumps are activated by resistive heating at 550° C, and once activated they continuously pump getterable gases such as hydrogen, oxygen, nitrogen, and

carbon monoxide, providing efficient, passive pumping without moving parts or electrical power during operation. The NEG pumps are one of the most important parts of the vacuum system as they are very effective at pumping hydrogen gas, which is usually the most abundant background gas in UHV systems.

3.3 Summary

In summary, the design of the QuantumIon vacuum chamber was described in detail, The conventional flange mounted design of surface ion trap systems was discussed and how it simplifies electrical connections to ion traps with close to 100 connections. The QuantumIon chamber's central trap-mounted design was described, highlighting how it provides increased optical access to the ions while also ensuring high conductance to vacuum pumps. This combination enables lower vacuum pressures and, consequently, longer ion lifetimes. The requirement for high NA re-entrants for individual addressing of ions and higher fluorescence collection was discussed and how the central mounted design of our system achieves that. Finally, the three sections of the chamber and their purposes were discussed. The experimental chamber contains the surface-electrode trap and ablation targets and is designed with high NA viewports in mind. The diagnostic chamber provides an area of high conductance for diagnostic components such as pressures gauges and RGAs. The geometry of the five-way cross maximizes the conductance between the experimental chamber and vacuum pumps leading to higher effective pumping speeds and lower vacuum pressures.

Chapter 4

Simulating Ion trajectories for Micromotion compensation

In section 2.2.1 we found that the motion of an ion in a RF ion trap is given by Eq. 2.12 which is restated below for convenience.

$$u_i(t) \approx u_{1i} \cos(\omega_i t + \varphi_{\mathcal{S}i}) \left(1 + \frac{q_i}{2} \cos(\Omega_{RF} t)\right) \tag{2.12}$$

where u_{1i} is the amplitude of the ion's secular motion, ω_i is the secular frequency, $\varphi_{\mathcal{S}i}$ is a phase determined by the initial conditions of the ion and Ω_{RF} is the RF drive frequency. Eq. 2.12 showed us that the motion of a trapped ion is given by a slower "secular" motion and a fast "micromotion" which is driven by the oscillating RF field. For trapped-ion experiments, we would like to work in a regime where the micromotion can be assumed to be small and the motion of the ion can be treated as a harmonic oscillator at frequency ω_i. The harmonic approximation enables the quantization of ion motion into discrete motional states (Fock states), which is essential for techniques such as resolved sideband cooling and the Mølmer–Sørensen gate. The latter is a two-qubit entangling operation that leverages the shared motional modes of an ion chain to mediate interactions between qubits.

If a trapped ion sits exactly at the null of the RF potential, then there would be no micromotion. However, an ion does not sit exactly still in a trap as it undergoes secular motion under the RF pseudopotential, which displaces the ion from the RF null. As the RF potential is non-zero away from the null, this leads to an unavoidable residual driven oscillation at the RF frequency. This is referred to as "intrinsic micromotion". However, there are other effects that can lead to more micromotion, the most detrimental of which

is the presence of stray electric fields. This type of micromotion is known as "excess micromotion" and can have severe effects on the performance of a trapped-ion system by modulating atomic transitions and increasing heating rates. Excess micromotion has to be compensated for by applying compensating electric fields to cancel out the stray electric fields in the system. This chapter estimates the level of stray electric fields that can be compensated for by the Phoenix trap used in our system. This is done via numerical simulations of the trajectory of a single ion under the electric potential generated by the Phoenix trap. By looking at the ion motion in the presence of stray and compensating fields, we are able to estimate an upper bound for the largest stray fields that can be compensated for with our trap. Section 4.1 describes excess micromotion, its effects and common experimental compensation methods used in trapped-ion laboratories. Section 4.2 describes the ion trajectory simulations and their results.

Author contributions: The author conducted the ion trajectory simulations and analyzed the results following discussions with Prof. Rajibul Islam. Fabien Lefebvre is acknowledged for insightful discussions on the trajectory simulations, as he was working on a related project in another trapped-ion system at the University of Waterloo. Collin J. C. Epstein is acknowledged for his assistance in understanding the *controlgen* software package used for calculating electric fields in the Phoenix trap.

4.1 Excess micromotion

We discussed how the trapping potential of an ion trap is decomposable into a static DC part and a dynamic RF part. In a perfect environment, with no stray electric fields, the nulls of the DC and RF potential coincide exactly in space. The presence of a static stray electric field will displace the null of the DC potential from the null of the RF potential. This will move the equilibrium position of the ion from the RF null to some new position, which is the average of the DC and RF potential nulls depending on their relative strengths. Now, the ion will see a much higher amplitude of the RF field and will consequently experience a much higher amplitude of micromotion. This is illustrated in Fig. 4.1. This type of micromotion is known as "excess micromotion" and can be very detrimental to trapped-ion systems. In the presence of a static stray field $\mathbf{E}_{DC}$, the Mathieu equation changes to

$$\ddot{u}_i + [a_i + 2q_i \cos(\Omega_{RF} t)] \frac{\Omega_{RF}^2}{4} u_i = \frac{Q\mathbf{E}_{DC} \cdot \hat{u}_i}{m} \tag{4.1}$$

As before, in the case where $|q_i| \ll 1$ and $|a_i| \ll 1$, the first-order solution to (4.1) is

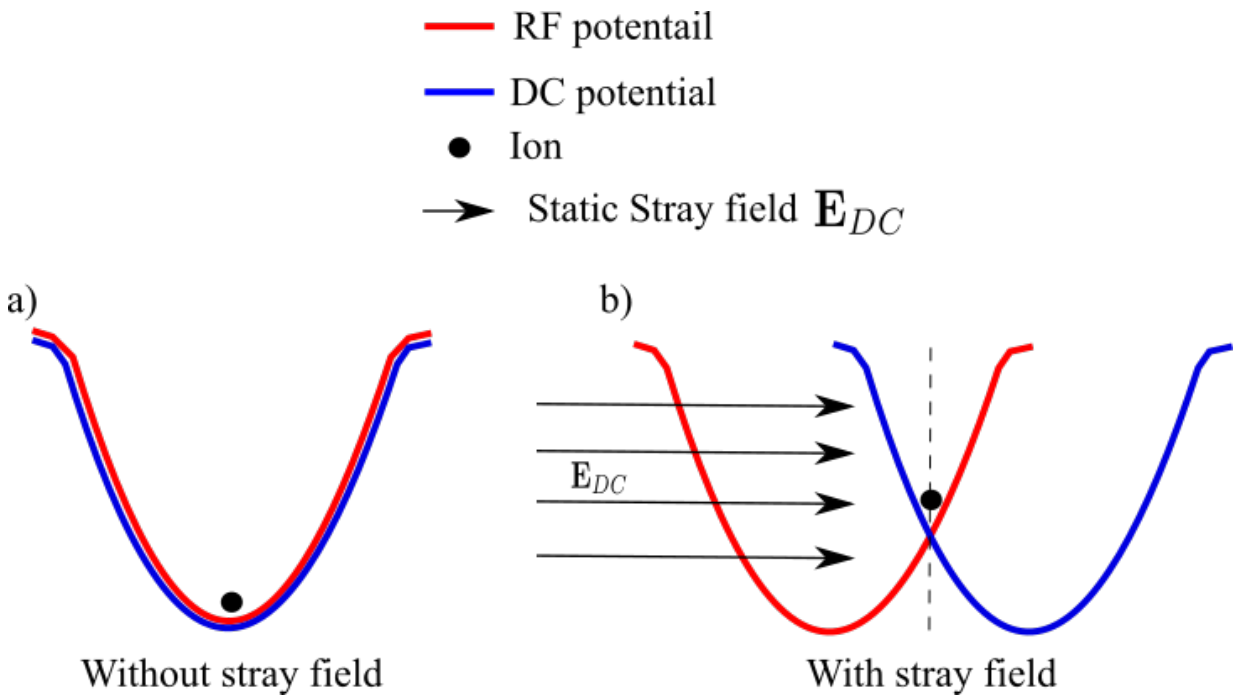


Figure 4.1: Illustration of how a static stray electric field $\mathbf{E}_{DC}$ can induce excess micromotion. a) Without any stray electric field both the DC and RF potential nulls coincide in space where the ion sits. b) In the presence of a stray electric field the DC null is displaced from the RF null, the ion moves to a new average position and experiences a higher RF potential leading to excess micromotion.

$$u_i(t) \approx [u_{0i} + u_{1i}\cos(\omega_i t + \varphi_{\mathrm{Si}})]\left[1 + \frac{q_i}{2}\cos(\Omega_{RF}t)\right], \tag{4.2}$$

The new term in equation 4.2

$$u_{0i} = \frac{4Q\mathbf{E}_{DC}\cdot\hat{u}_i}{m(a_i + \frac{1}{2}q_i^2)\Omega_{RF}^2} = \frac{Q\mathbf{E}_{DC}\cdot\hat{u}_i}{m\omega_i^2} \tag{4.3}$$

shows the displacement of the ion and how it depends on the static stray field $\mathbf{E}_{DC}$. The ion is displaced to some new average position $\mathbf{u}_0 = u_{0x}\hat{x} + u_{0y}\hat{y} + u_{0z}\hat{z}$, and the amplitude of excess micromotion at this new position is $\frac{1}{2}u_{0i}q_i$ in the direction u_i. In a trapped-ion system, stray electric fields can arise from various sources, including electromagnetic interference from nearby electronic equipment and photoelectric charging of the trap surface,

where scattered laser light, particularly in the ultraviolet range, induces the emission of electrons [69]. Additionally, imperfections in trap fabrication and materials, as well as contamination introduced during system assembly or operation, can cause patch potentials on the trap surface, leading to stray electric fields.

For the 4-rod linear Paul trap shown in Fig 2.5 excess micromotion can also be caused by a phase mismatch between the RF voltages V_{RF} sent to the two RF electrodes. However, this issue is mitigated in the Phoenix trap employed in the QuantumIon system, as it utilizes a single RF rail that symmetrically splits to both sides of the six-rail layout, ensuring phase coherence across the trap.

4.1.1 Effects of micromotion

Micromotion in trapped-ion systems, especially when not well compensated (i.e., excess micromotion), can have several detrimental effects on both quantum information processing and precision metrology. It leads to time-dependent Doppler shifts that degrade the stability and fidelity of laser-ion interactions [19], causing errors in quantum gates and reducing coherence times. Micromotion also increases the ion's kinetic energy, which cannot be removed by standard cooling techniques, resulting in motional mode heating [6] and inefficient cooling [9]. Moreover, excess micromotion can modulate fluorescence during state detection, lowering readout fidelity, and introduce systematic frequency shifts such as the second-order Doppler and AC Stark shifts—critical in atomic clock applications [31]. For multiple trapped ions, micromotion of one ion can drive parametric heating of another ion which can lead to destabilizing the ion chain. [9, 67, 55]. In surface-electrode traps, micromotion is even more pronounced due to the close proximity of the ions and laser beams to the trap surface. Therefore, precise compensation of micromotion is essential to ensure high-fidelity control and stability in ion trap experiments.

4.1.2 Compensating Micromotion

As discussed earlier, laser cooling techniques such as Doppler cooling and RSC can be used to reduce the kinetic energy of a trapped ion by damping its secular motion. However, these methods have no direct effect on micromotion, since it is a driven motion at the RF drive frequency and not subject to dissipative cooling. The only way to reduce micromotion is by applying static DC compensating electric fields to shift the ion back to the RF null point. These compensating fields are generated by applying precise DC offset voltages to specific electrodes such that the stray electric field that displaced the ion is canceled out. Since the

RF fields are primarily used for confinement in the radial directions (x and y in Figs. 2.5 and 2.7), micromotion amplitude is much higher in the radial directions compared to axial. However, compensation can still be required in the axial direction as there is always some component of the RF fields in that direction. In order to know what DC voltages to apply, we need to be able to detect the micromotion first.

Coarse micromotion compensation can be performed by adjusting DC voltages to minimize the broadening of a relatively wide atomic transition (on the order of 10 MHz) caused by micromotion sidebands. Another approach involves detecting shifts in the position of the ion as the RF amplitude is varied, either by imaging the ion on a CCD camera or by tracking how much a focused laser beam must move to maintain peak fluorescence. The DC voltages are then adjusted until the ion remains stationary as the RF amplitude changes, effectively placing it within $\approx 1\,\mu$m of the RF null

For finer compensation, various methods have been developed over the years. One common method is using resolved sideband spectroscopy on a narrow atomic transition. The micromotion from the ion being displaced from the RF null leads to a time dependent Doppler shift of the laser in the ions frame. This leads to micromotion sidebands, which are spectral features offset from the carrier transition by integer multiples of the RF drive frequency. By scanning the laser across the transition and detecting the presence and amplitude of these sidebands, the magnitude and direction of excess micromotion can be inferred. Compensation is achieved by adjusting DC voltages to null the sidebands, thereby minimizing micromotion. This method allows us to position the ion to within 10s of nanometers of the RF null, but requires an atomic transition with a linewidth much narrower than the RF drive frequency in order to resolve the micromotion sidebands which might not be available in all ion species. A less complex micromotion compensation method that does not require a narrow linewidth optical transition is the RF-correlation method. This technique relies on measuring the correlation between the ion's photon scattering rate and the phase of the RF drive cycle. Due to micromotion, the ion experiences a velocity-dependent Doppler shift of the laser frequency in its own frame. This Doppler shift periodically modulates the effective laser detuning at the RF frequency, which in turn causes a corresponding periodic modulation in the ion's photon scattering rate. As a result, the photon scattering rate becomes correlated with the RF drive phase. By using a single-photon detector with high time resolution to record photon arrival times relative to the RF cycle, this correlation can be measured directly. The value of fluorescence can be calculated by Eq. (4.4) [31].

$$S(t) = S_0 + \Delta S \cos(\Omega_{RF} t + \phi) \tag{4.4}$$

Here S_0 is the mean number of photons emitted and ΔS is the modulation amplitude of the fluorescence rate due to micromotion. By applying an appropriate combination of voltages to the compensation electrodes, we aim to minimize the ratio $\frac{\Delta S}{S_0}$, which directly corresponds to the amplitude of the excess micromotion. Both of the methods described above are only sensitive to micromotion components along the direction of the incident laser beam. Therefore, to fully compensate for micromotion in all spatial directions, multiple laser beams with different propagation directions are typically required. This requirement poses particular challenges for surface-electrode traps, where directing laser beams perpendicular to the trap surface can cause unwanted effects such as charging of the trap surface and increased background light scattering.

A recently developed method for micromotion compensation employs RF amplitude modulation to parametrically excite the ion's secular motion [44]. In this approach, the amplitude of the RF trapping potential is modulated at a frequency close to one of the ion's secular frequencies. If the ion is displaced from the RF null (due to a stray electric field), this modulation coherently excites secular motion. The amplitude of the resulting motion is proportional to the component of the stray electric field along the direction of the probed secular mode.

This induced motion leads to a modulation of the fluorescence rate. By recording the photon arrival times and correlating them with the RF modulation frequency, a signal is obtained whose strength reflects the amplitude of the induced secular motion, and thus the magnitude of the excess micromotion. By applying suitable DC compensation voltages, the correlated motion amplitude can be reduced to zero, indicating effective cancellation of the stray electric field. This zero-crossing provides a robust signal for precise micromotion compensation. Each secular mode can be selectively excited, provided the laser beam has a non-vanishing projection along that mode's direction. As a result, this technique requires only a single laser beam, which has made it especially attractive for surface-electrode trap systems.

4.1.3 Micromotion compensation in the Phoenix trap

In the case of a 4-rod Paul trap, micromotion compensation along the radial direction is done by applying appropriate DC offset voltages to two opposite RF rod electrodes. Compensation along the axial direction can be done via the needle electrodes. For surface-electrode traps, micromotion compensation is done by applying appropriate DC voltages to the segmented DC electrodes shown in Fig 2.7 b). The Phoenix trap used in the QuantumIon system has dedicated electrodes for micromotion compensation. These are

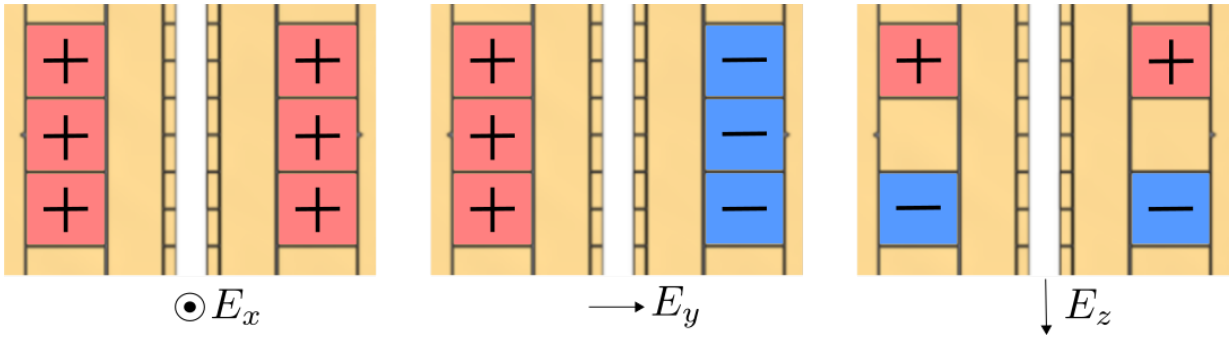


Figure 4.2: Voltage configurations for stray electric field compensation. Shows a cut out of the center of the quantum region of the Phoenix trap with voltages configurations to generate micromotion compensation fields along x, y, and z directions. Adapted from [18].

the 11 outer DC electrode pairs shown in Fig. 2.9 in the Quantum zone of the trap. With this large number of outer DC electrodes, various combinations of voltages and electrodes can be used to generate compensation fields along all directions. Fig 4.2 shows voltage configurations for generating compensation fields along all 3 spatial directions in the Phoenix trap.

The stray electric field can have components along all spatial directions, making the task of determining the optimal compensation voltages a multidimensional optimization problem. This complexity arises because applying a DC compensation voltage to cancel the field in one direction can inadvertently introduce electric fields in other directions. As a result, compensation along individual axes cannot be treated independently. In practice, a iterative approach is typically employed, where fine-grained adjustments are made to the DC compensation voltages. Through successive measurements and corrections, the stray electric field is progressively reduced until the micromotion is minimized as much as possible.

4.2 Simulating Ion trajectories

For the Phoenix trap, it is important to understand the range of stray electric fields that can be effectively compensated. The micromotion compensation methods described above—such as RF-correlation, resolved sideband spectroscopy, and RF amplitude modulation, require the presence of a trapped ion to perform the necessary measurements.

However, during the course of my master's degree, the experimental setup was still under construction, and ion trapping had not yet been achieved. At the time of writing this thesis, the research group is in the process of attempting to trap ions for the first time. As a result, direct experimental characterization of the compensation range has not yet been possible.

Nevertheless, we can still estimate the micromotion compensation capabilities of the trap using numerical simulations of the trajectory of a single ion. By modeling the ion's motion under stray fields and compensation voltage configurations, we can evaluate the effectiveness and range of micromotion compensation achievable in our system prior to experimental implementation.

To simulate the ion's motion classically in the Phoenix trap, we can use Newton's first law

$$\mathbf{F} = m\mathbf{a} = Q\mathbf{E}(u_x, u_y, u_z, t) \tag{4.5}$$

this leads to the classical equations of motion

$$\begin{aligned} m\ddot{u}_x &= QE_x \\ m\ddot{u}_y &= QE_y \\ m\ddot{u}_z &= QE_z \end{aligned} \tag{4.6}$$

where m is the mass of the ion, Q is its charge and $u_{x,y,z}$ and $E_{x,y,x}$ is the position of the ion and the electric field in the x, y, z directions respectively.

We know the charge and mass of the ions, so the only thing we have to find is the electric fields generated by our trap in its trapping region. The total electric field is a sum of the DC and RF fields.

$$\mathbf{E}_{total} = \mathbf{E}_{DC} + \mathbf{E}_{RF} \tag{4.7}$$

4.2.1 *controlgen*

For a custom-designed ion trap, the electric fields and potentials are typically computed by modeling the electrodes in finite element simulation software such as COMSOL. However, our group was given access to a software package called *controlgen* which was also developed by Sandia National labs. This software package is able to read pre-computed voltage

array files which are specific to the Phoenix trap and were also pre-computed and provided to us by Sandia National labs. The voltage array file is basically a precomputed data file that stores the basis electrode potentials and electric fields for all of the trap's electrodes assuming 1 V is applied individually to each one with all other electrodes grounded. The pre-computed basis potentials in the voltage array file are computed for a pre-determined set of positions around the RF null of the trap. These basis solutions can be linearly combined, weighted by the desired electrode voltages, to quickly compute the resulting electric potential or field for any arbitrary voltage configuration applied to the trap electrodes. Mathematically this looks like

$$\begin{aligned} \phi_{total}(u_x, u_y, u_z, t) &= \phi_{DC} + \phi_{RF} \\ \phi_{total}(u_x, u_y, u_z, t) &= \sum_i V_i \, \phi_i(u_x, u_y, u_z, t) + V_0 \cos(\Omega_{RF} t) \phi_{RF-rail} \end{aligned} \tag{4.8}$$

where ϕ_{total} is the total potential generated by the trap, V_i is voltage applied to the i^{th} DC electrode, ϕ_i is the basis potential for the i^{th} DC electrode, V_0 is the RF voltage amplitude and $\phi_{RF-rail}$ is the basis potential for the RF rail electrode. The DC potential remains static during most operations and the time term in ϕ_i is only relevant when performing shuttling operations. A similar approach is used to generate the total electric field.

The *controlgen* package has many useful functions

1. **Generate DC voltage configurations for trapping**. *controlgen* has a built in solver where a user can define a set of constraints such as electric field and potential at specific locations, desired secular frequencies, specific voltages and electrodes etc and *controlgen* calculates what DC voltages to apply to the trap.

2. **Generating the electric potential and electric fields in the quantum region**. It can also work in the opposite direction to the one described in the previous point, where a user can give it a set of DC voltages and it can calculate the potential and fields generated from those voltages.

3. **Calculate trapping parameters**. For a given set of DC and RF voltages, it can calculate useful trapping parameters such as the secular frequencies, exact location of the RF null etc

4.2.2 Ion trajectory simulations

So, using *controlgen*, the total electric field generated by the Phoenix trap in the quantum zone can be computed and used to solve Eq. (4.6), thereby enabling simulation of an ion's trajectory. To do this, we first need to know what DC and RF parameters we want to use. For surface-electrode traps, typical RF voltage amplitudes are around 150-200 V and desired drive frequencies are typically 36-40 MHz. In trapped-ion experiments, the RF drive required for ion confinement is supplied through a helical resonator. A helical resonator is a high-Q resonant circuit consisting of a coil enclosed in a conducting shield, which efficiently couples RF power into the ion trap. It provides a substantial voltage step-up at its resonance frequency while simultaneously suppressing all other frequency components, thereby reducing noise on the trap electrodes. The RF drive frequency in trapped-ion experiments is determined by the resonance of the helical resonator, which can be sensitive to construction details and loading from the trap. As a result, the resonator effectively sets the operating drive frequency for the system. The resonator in our system has a resonance frequency of 32.9 MHz, which sets the RF drive frequency used in our simulations.

For the DC voltages, we would like to trap in the center of the quantum zone so we can set that as a constraint in *controlgen* and generate a set of DC voltages that provide axial confinement in the center of the trap. This voltage solution is shown in Fig. 4.3 together with plots of the corresponding potential. For the voltage arrays of the Phoenix trap, the trap center is the origin of the coordinate system used, so trapping in the center corresponds to trapping at $(u_x, u_y, u_z) \approx (70, 0, 0)\,\mu$m. The $\approx 70\,\mu$m comes from the ions being trapped $\approx 70\,\mu$m above the trap surface, which is what the Phoenix trap was designed for.

We can now simulate the trajectories of a $^{133}Ba^{+}$ ion under the potential shown in Fig. 4.3 b) and c). These trajectories should resemble Fig. 2.6 which plots the solutions of the Mathieu equations. To look at the secular and micromotion components of these trajectories, we can analyze the FFT spectrum of the trajectories near the secular and RF drive frequencies. The trajectories are shown in Fig 4.4 and their corresponding FFTs are shown in Fig. 4.5. These trajectories are indeed in agreement with Eq. (2.12) and Fig. 2.6 as we clearly see the large secular oscillations along with the small micromotion. We can determine the secular frequencies from the FFT spectrum in Fig. 4.5. The axial frequency is around 600 KHz and the radial frequencies are around 2.8 MHz which are typical for trapped-ion systems. As discussed in section 2.2.1, the axial frequency is lower than the radial frequencies so that when multiple ions are trapped they line up in a linear chain along the axial direction. To observe micromotion, we can examine the FFT spectrum of the ion's trajectory and focus on the region around the RF drive frequency. In the presence of both intrinsic and excess micromotion, we expect to see three distinct peaks:

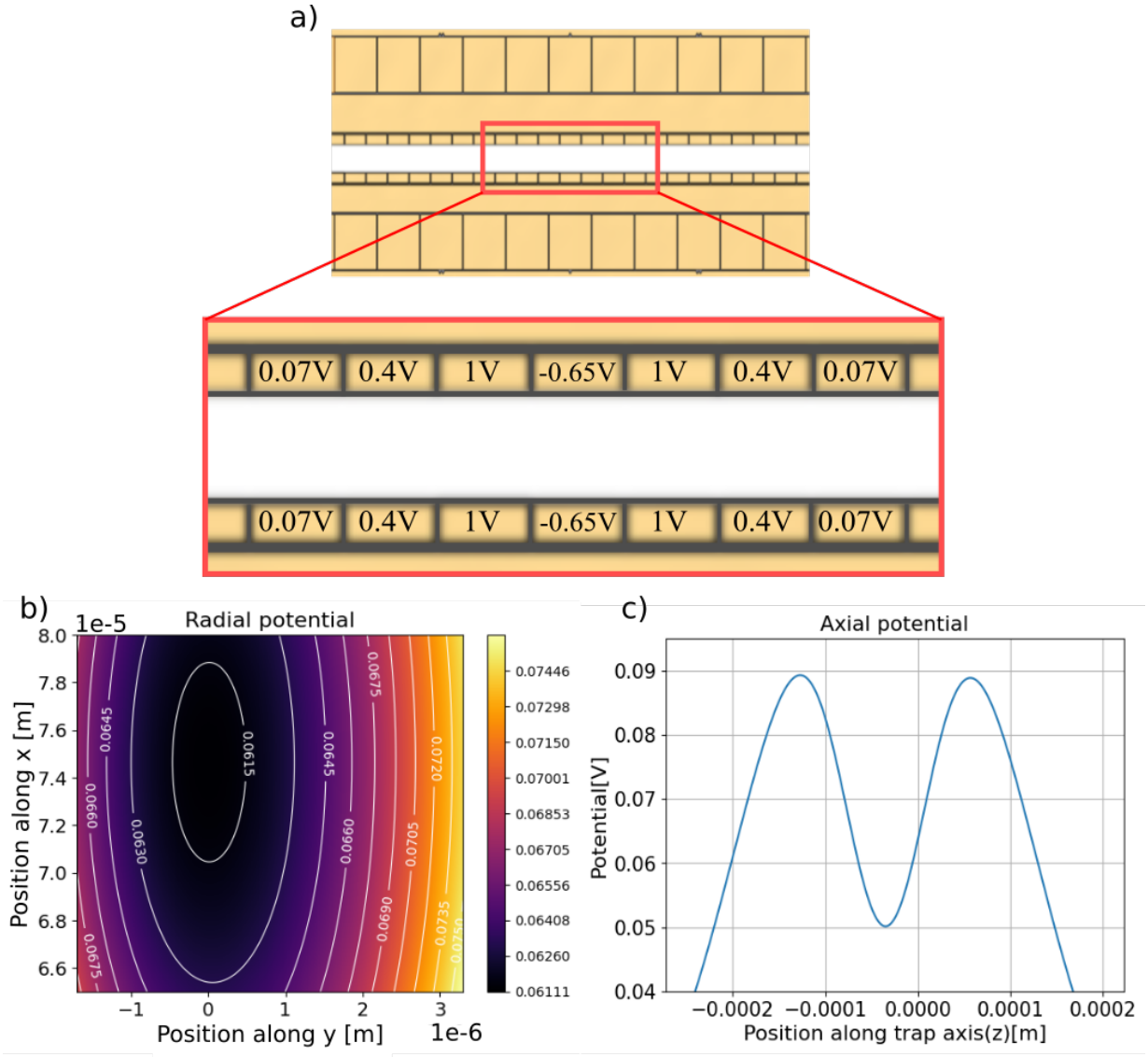


Figure 4.3: DC voltages and the corresponding electric potential for trapping an ion in the Phoenix trap. a) Shows the DC voltages for axial confinement in the center of the quantum zone of the Phoenix trap. b) Shows the Radial DC potential + RF pseudopotential for $V_0 = 150V$ and $\Omega_{RF} = 32.9$MHz. C) Shows the potential along the axial direction for the DC voltages in a). We can see the minimum close to 0 which is the center of the trap.

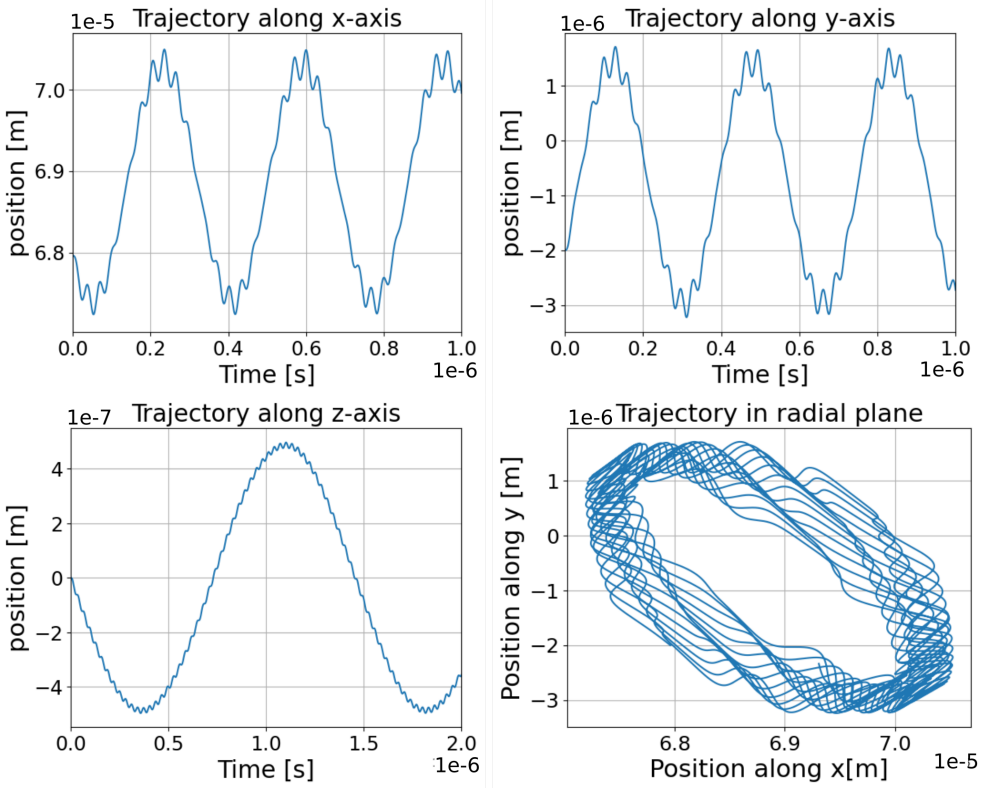


Figure 4.4: Trajectories of a $^{133}Ba^{+}$ ion in all directions as well as the radial plane. We can clearly see that the trajectories follow Eq. (2.12) with a slow secular motion and fast micromotion. RF voltage amplitude $V_0 = 150V$, RF drive frequency $\Omega_{RF} = 32.9\,\text{MHz}$ and the DC voltage from Fig. 4.3 a) where used for these trajectories.

1. A peak at Ω_{RF} corresponding to excess micromotion,
2. And two sidebands at $\Omega_{RF} \pm \omega_i$ associated with intrinsic micromotion, where ω_i is the secular frequency along a particular axis.

Intrinsic micromotion appears as two sidebands at $\Omega_{RF} \pm \omega_i$, as it arises from the ion's secular motion in the trap being modulated by the RF field. In contrast, excess micromotion results from a static displacement of the ion from the RF null and therefore shows up as a single peak at the RF drive frequency. This is exactly what we see in Fig. 4.5, two larger intrinsic micromotion peaks and barely any excess micromotion. This is expected as there are no stray fields introduced into the simulations yet, so there shouldn't be any

excess micromotion. We also observe that there is almost no micromotion in the axial direction compared to the radial directions. This is expected as the RF fields primarily act along the radial directions.

By introducing stray electric fields, we should see the central micromotion peak become much larger in amplitude. Then we can apply DC voltages to the micromotion compensation electrodes in the Phoenix trap and verify if and to what extent we can minimize the central (excess micromotion) peak.

The largest stray electric field we can compensate for with the Phoenix trap depends on the largest compensating field the trap can produce in each direction. This depends on the largest DC voltage that can be safely applied to the compensation electrodes. The Phoenix trap is able to handle a maximum voltage of $\pm 30\,\mathrm{V}$ on its DC electrodes. However, the QuantumIon system uses the Advanced Real-Time Infrastructure for Quantum physics (ARTIQ) control system, a state-of-the-art solution for quantum information experiments developed by M-Labs in collaboration with the Ion Storage Group at National Institute of Science and Technology (NIST) [38, 43]. ARTIQ is now widely adopted and supported by a growing number of research institutions worldwide. The ARTIQ system uses a 32-channel, 16-bit Digital-to-Analog Converter (DAC), which we use to deliver DC voltages to our trap. This DAC has a maximum output range of $\pm 10\,\mathrm{V}$, which sets the upper limit on the DC voltages that can be applied through the ARTIQ system. While it would be relatively straightforward to use a separate voltage source capable of exceeding $\pm 10\,\mathrm{V}$, doing so would forgo the tight integration and synchronization features offered by the ARTIQ control system.

Therefore, given the $\pm 10\,\mathrm{V}$ output limit, we aim to determine the maximum electric field strengths that can be simultaneously generated by the Phoenix trap along all spatial directions at the ion's location. By applying voltages to four pairs of the outer DC micromotion compensation electrodes and computing the resulting fields using *controlgen*, field strengths of approximately $E_x \approx 3000\,\mathrm{V/m}$, $E_y \approx 3800\,\mathrm{V/m}$, and $E_z \approx 600\,\mathrm{V/m}$ can be achieved. Now, we can introduce stray electric fields of the same magnitude and verify, using the simulated ion trajectories, whether these fields can be effectively compensated. Figure 4.6 shows the ion trajectories along with the corresponding FFT spectrum that highlights the micromotion peaks in the presence of a stray electric field. From the trajectories, we observe that the presence of stray electric fields increases the amplitude of both the secular and micromotion components in the radial directions, whereas the motion along the axial direction remains largely unaffected. The micromotion amplitude increases to $\approx 1\,\mu\mathrm{m}$ in the radial direction, compared to $\approx 0.25\,\mu\mathrm{m}$ in the absence of stray fields. Similarly, the secular motion amplitude increases to $\approx 11\,\mu\mathrm{m}$, up from $\approx 4\,\mu\mathrm{m}$ without stray fields. This clearly indicates that the ion is heating up due to the excess micromotion.

In the FFT spectrum, the central excess micromotion peaks in the radial directions are significantly larger compared to the case without stray electric fields, as shown in Fig. 4.5. This confirms that the ion experiences substantially enhanced micromotion when displaced from the RF null by a stray field.

4.2.3 Results

Next, we aim to verify whether the excess micromotion can be compensated by applying electric fields using the Phoenix trap's micromotion compensation DC electrodes. In this case, since the components of the stray electric field along each spatial direction are already known, it is straightforward to determine the appropriate DC voltages required for compensation. The resulting ion trajectories, along with the corresponding FFT spectrum highlighting the micromotion peaks in the presence of both stray and compensating fields, are shown in Fig. 4.7. The trajectories clearly indicate that we are able to push the ion back to the RF null and reduce micromotion significantly. Both the micromotion and secular motion amplitudes in the radial directions have gone back down to $\approx 0.25\,\mu$m and $\approx 4\,\mu$m respectively. We see the central excess micromotion peak in the FFT go down to approximately the small amplitude as when there was no stray field.

Thus, the simulations indicate that the Phoenix trap is capable of compensating for stray electric fields on the order of $E_x \approx 3000\,\mathrm{V/m}$, $E_y \approx 3800\,\mathrm{V/m}$, and $E_z \approx 600\,\mathrm{V/m}$, effectively returning the ion to the RF null and significantly reducing excess micromotion. Typical stray electric fields observed in surface-electrode trapped-ion systems range from several tens to a few hundred volts per meter [58, 30, 44], with fields as large as $1300\,\mathrm{V/m}$ also reported [58]. Therefore, the Phoenix trap should be well capable of compensating any stray electric fields that may be present in the QuantumIon system.

In addition to analyzing the micromotion compensation capabilities of our trap, these trajectory simulations serve as an effective tool for rapidly verifying whether a given set of RF and DC voltage parameters result in stable ion trapping. For example, by examining the ion trajectories, we can extract the amplitude of the secular motion and determine whether the ion possesses excessive kinetic energy—i.e., if it is too "hot". Moreover, by modifying the initial conditions of the ion to include some initial velocity, we can estimate how energetic the incoming plume of atoms from the ablation process can be while still allowing successful trapping.

4.3 Summary

In summary, we estimated the maximum compensatable stray electric field strengths achievable using the Phoenix trap's compensation electrodes, limited by the $\pm 10\,\mathrm{V}$ range of the DAC in our system. Numerical simulations indicate that stray fields up to $E_x \approx 3000\,\mathrm{V/m}$, $E_y \approx 3800\,\mathrm{V/m}$, and $E_z \approx 600\,\mathrm{V/m}$ can be compensated which are well above the typical stray fields encountered in trapped-ion systems. These results suggest that the trap has sufficient tuning range to perform robust micromotion compensation. Once an ion is successfully trapped in our system, the next step will be to experimentally verify micromotion compensation using standard techniques such as the RF-photon correlation method or sideband spectroscopy. These measurements will provide a practical benchmark for the effectiveness of the compensation range and inform further refinements to the control voltages applied to the compensation electrodes.

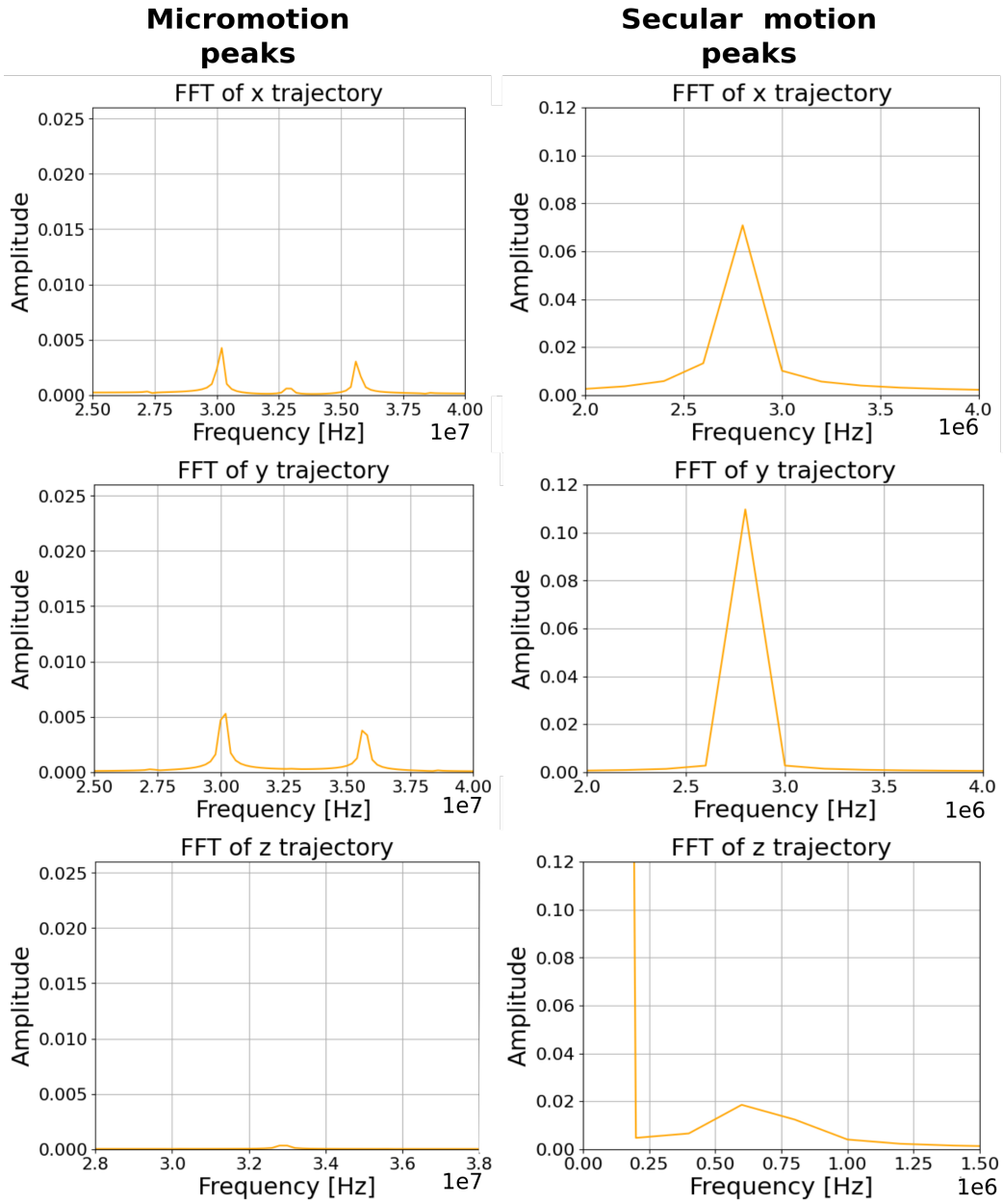


Figure 4.5: FFT spectrum of the ion's trajectories. The plots in the right column show the secular frequencies. Plots in the left column show the two sidebands and central peak for intrinsic and excess micromotion respectively. The central peak at the RF drive frequency is very small as there are no stray electric fields and hence no micromotion.

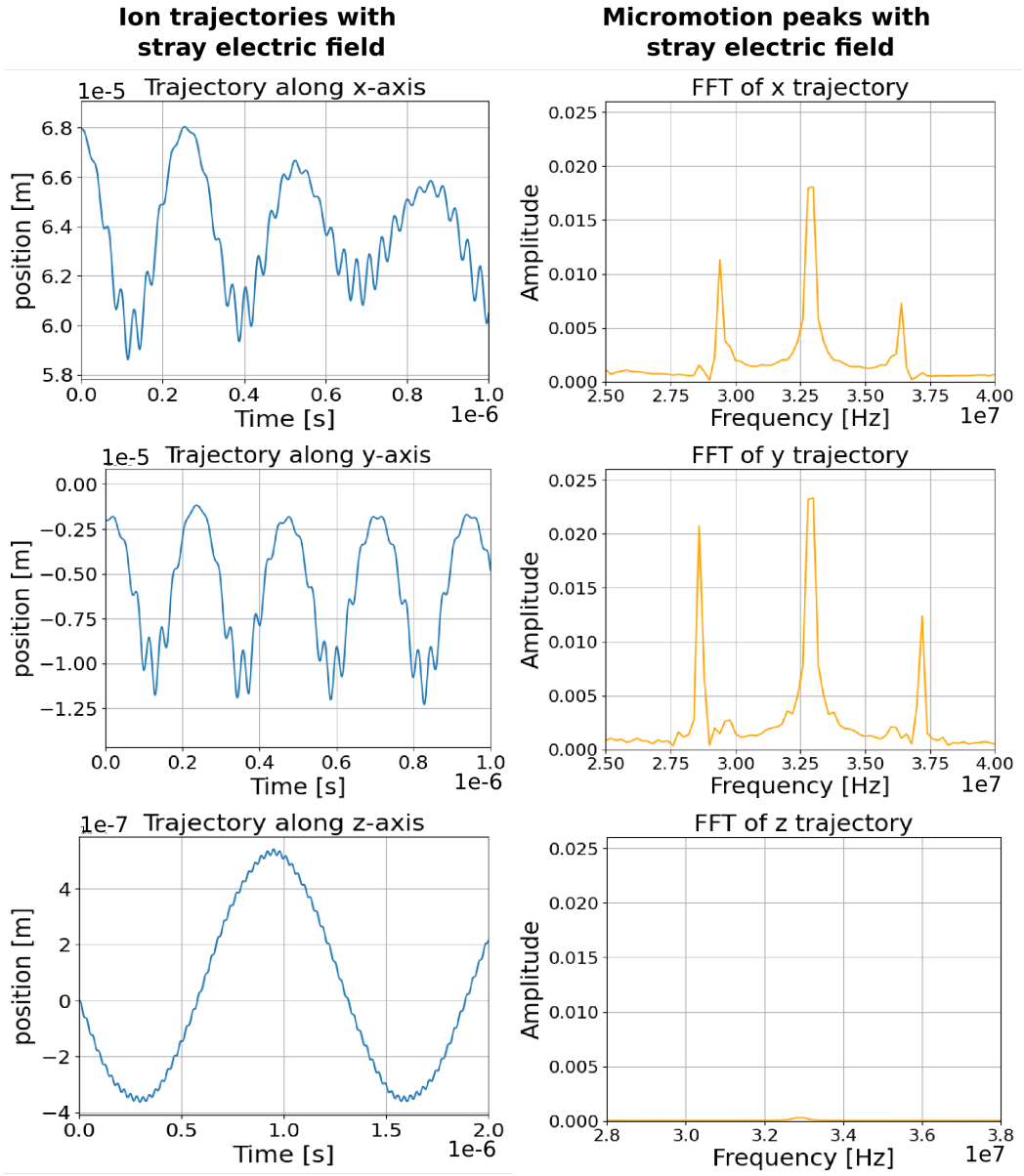


Figure 4.6: Ion's trajectories and their FFT spectrums in the presence of a stray electric field $E_x \approx 3000\,\mathrm{V/m}$, $E_y \approx 3800\,\mathrm{V/m}$, and $E_z \approx 600\,\mathrm{V/m}$. We see a significant increase the the micromotion and secular motion amplitude in the radial directions (x and y) compared to Fig. 4.4. The FFTs show a much larger excess micromotion peak in the radial directions compared to Fig. 4.5. Motion along the axial direction remains mostly unchanged.

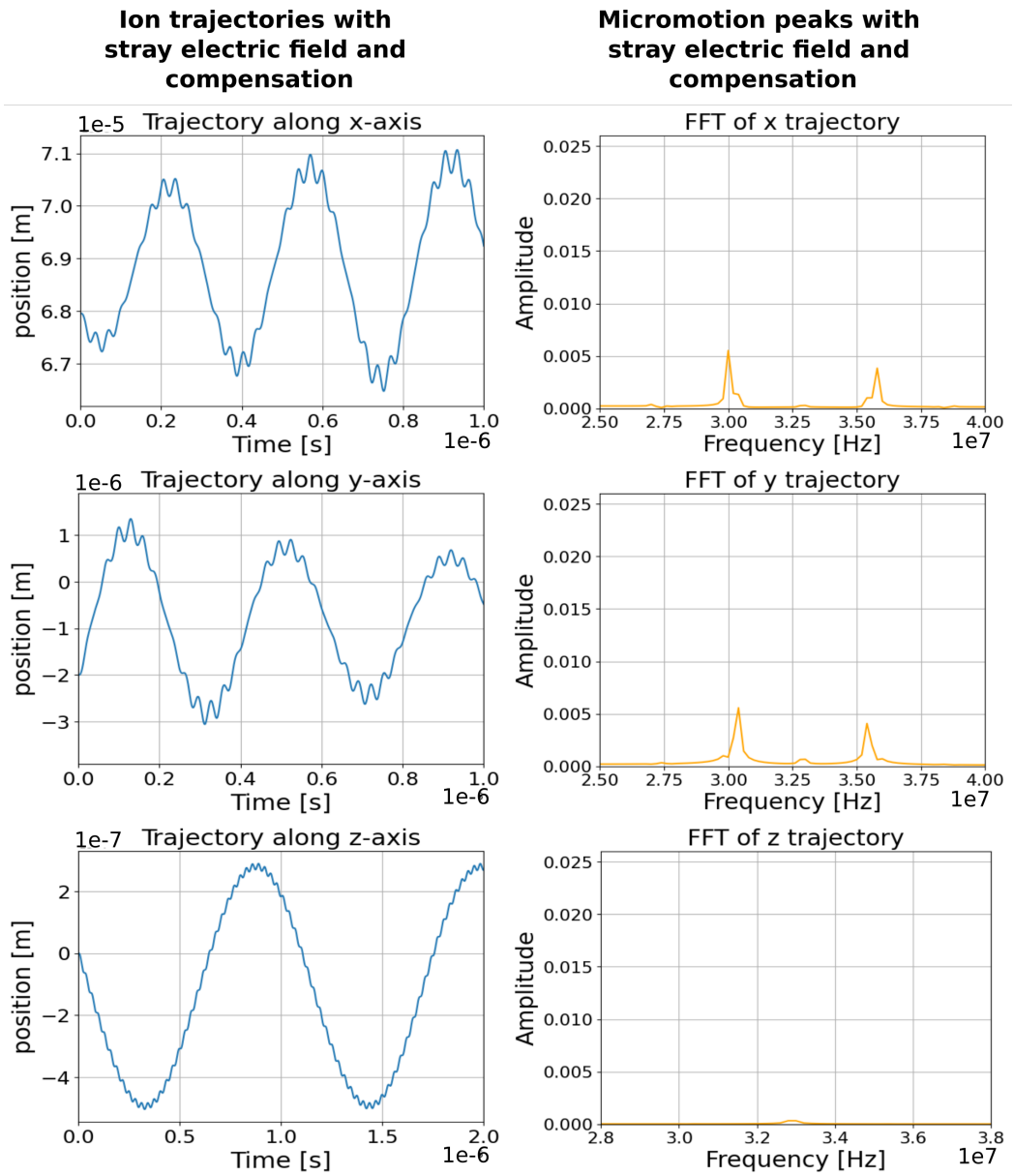


Figure 4.7: Ion's trajectories and their FFT spectrums in the presence of a stray electric field and compensation fields turned on. The micromotion and secular motion amplitudes go back down what they were with no stray electric field (see Fig. 4.5). This shows that we have successfully pushed the ion back to the RF null and almost completely eliminated the excess micromotion.

Chapter 5

Barium atomic sources

Surface-electrode traps are known to have low trap depths (typically in the range of 0.1-0.2 eV), which are typically not much higher than the mean kinetic energy of the neutral atoms before they are ionized [57]. Atoms produced from laser ablation typically have a wide distribution of velocities, and in order to trap atoms with high probability, it is essential that a large majority of those ablated atoms have kinetic energies below the trap depth. This can become problematic as the majority of the atoms produced from ablation of salt targets such as $BaCl_2$ will have kinetic energy much higher than the typical trap depth of a surface-electrode trap. Therefore, a surface-electrode trap would only be able trap slower moving atoms which would be very low in number, which greatly reduces the probability of successful trapping. However, metallic barium targets have been shown to produce ablated atoms much slower than $BaCl_2$ [59]. This greatly increase the probability of trapping ions especially during initial trapping attempts. This chapter describes the $BaCl_2$ targets used in our system and compares atom velocities from these targets to the trapping depth of the Phoenix trap. The chapter then presents a feasibility study on the use of metallic barium as an ablation target.

Section 5.1 describes how the $BaCl_2$ ablation targets used in our system are made. Section 5.2 compares the velocity of atoms produced from $BaCl_2$ to the maximum trap depth of the Phoenix trap which was calculated to be 0.168 eV. Section 5.3 presents neutral fluorescence and TOF spectroscopy measurements of a metallic barium ablation target to confirm the production of neutral atoms and their velocities with our ablation setup. Finally, section 5.4 describes a ablation target holder that mounts the three different types of targets used in our vacuum chamber.

Author contributions: The idea of using a metallic barium ablation target arose during

the initial assembly stages of the QuantumIon vacuum chamber, motivated by concerns regarding the high velocities of atoms produced from salt-based targets. The author is credited with sourcing metallic barium suitable for our application, and for conducting neutral fluorescence and TOF spectroscopy experiments, as well as performing the data analysis that led to Fig. 5.4 and Fig. 5.5. The experimental setup was originally constructed by former PhD student Dr. Noah Greenberg and postdoctoral researcher Dr. Akbar Jahangiri Jozani for testing $BaCl_2$ ablation targets. The author used this setup to carry out the barium metal experiments. Acknowledgment is given to Dr. Akbar Jahangiri Jozani for assisting with the experiments, supporting the data analysis, and fruitful discussions on understanding the underlying physics.

5.1 $BaCl_2$ ablation targets

We discussed in section 2.1.1 how the radioactivity of the $^{133}Ba^+$ ion restricts the method of producing ^{133}Ba atoms to laser ablation. In the QuantumIon system, ^{133}Ba atoms are produced by laser ablating a $BaCl_2$ ablation target. These targets are made using a preparation method developed in the QuantumIon lab by previous PhD student Dr. Noah Greenberg [22, 23]. The development of these $BaCl_2$ targets was motivated by inconsistent and unreliable loading of Ba^+ ions in a surface-electrode trap [59] and a 4-rod trap at another lab in the University of Waterloo.

^{133}Ba is procured in the form of $BaCl_2$ dissociated in a vial of weak hydrochloric acid. The radioactivity of the vial purchased by us was assumed to be $\sim 37\,\mathrm{MBq}$, which is equivalent to $6\,\mu\mathrm{g}$ of $BaCl_2$. Nonradioactive $BaCl_2$ is obtained in powder form, which is dissolved in deionized water. The solutions are then deposited onto platinum substrates with a pipette, one drop at a time. The substrate is then heated on a hot plate at 115°C to evaporate the solution, leaving the salt behind. This temperature is used to ensure that the solution does not evaporate too vigorously, which will lead to splattering of the $BaCl_2$ causing contamination and material loss.

After the solution is completely evaporated, the salt is left behind in a 'ring pattern'. This is due to the "coffee ring effect," which arises as a result of a difference in evaporation rates at the edge of the targets compared to the center. The formation of these rings leads to an uneven distribution of the $BaCl_2$ salt on the substrate, which would lead to inconsistent atom production during laser ablation. To fix this, the platinum substrates are heat treated by running a large amount of current through them ($I \approx 55\mathrm{A}$). This process heats the material to the melting point of $BaCl_2$ (962° C), causing the salt to melt,

adhere to the substrate, and redistribute uniformly across its surface. These microgram-scale ablation targets have been demonstrated to consistently and reliably generate neutral barium atoms via laser ablation, with average ablation spot lifetimes of approximately 185 laser pulses [22, 23].

5.2 Velocity of ablated atoms and trap depth

5.2.1 Velocity of atomic plume from $BaCl_2$ targets

An extremely important factor that determines whether atoms produced via laser ablation can be trapped is the velocity of the atomic plume generated from the ablation pulse. In order to reliably trap ions, the mean kinetic energy of the neutral atoms produced from laser ablation before they are ionized must be lower than the trap depth of the ion trap. Barium ions have been trapped using $BaCl_2$ ablation targets in a 4-rod trap at the Qudit lab at the University of Waterloo. They have performed TOF spectroscopy to extract a velocity distribution of the atomic plume generated from laser ablation of $BaCl_2$ targets, to obtain estimates of the plume temperature and peak velocity [70, 8].

TOF spectroscopy uses a pulsed ablation laser focused onto a $BaCl_2$ target to generate a plume of atoms. A resonant detection laser, tuned to the $6s^2\,{}^1S_0 \leftrightarrow 6s6p\,{}^1P_1$ transition in neutral barium at 553 nm, intersects the atomic plume at a fixed known distance from the ablation target. Following the ablation pulse, the fluorescence signal is recorded as a function of the time delay t_d after the pulse using a PMT. Since faster atoms arrive at the detection region earlier, while slower atoms take longer, the recorded fluorescence as a function of time directly corresponds to the velocity distribution of the neutral atoms in the plume. The time delay between the ablation laser pulse and the peak of the fluorescence signal provides an estimate of the peak velocity, $v_{peak} = d/t$ where d is the distance between the ablation target and the 553 nm beam, and t is the delay time corresponding to the signal maximum. Fig. 5.1 shows the ablation TOF distributions for $BaCl_2$.

From the velocity distribution a plume temperature of $37{,}000 \pm 1{,}000\,\mathrm{K}$ and a peak velocity of $2{,}600 \pm 50\,\mathrm{m/s}$ is estimated. We can also see that there is still a significant number of atoms with velocities between $1000 - 2000\,\mathrm{m/s}$ and a small number of atoms between $500 - 1000\,\mathrm{m/s}$. This means that in order to consistently trap atoms produced from laser ablation of $BaCl_2$ we would need a ion trap with a trapping depth high enough for atoms with velocities of $\approx 2,600\,\mathrm{m/s}$. One can get away with a lower trap depth corresponding to $500 - 1000\,\mathrm{m/s}$ but the loading rates would be much lower due to the

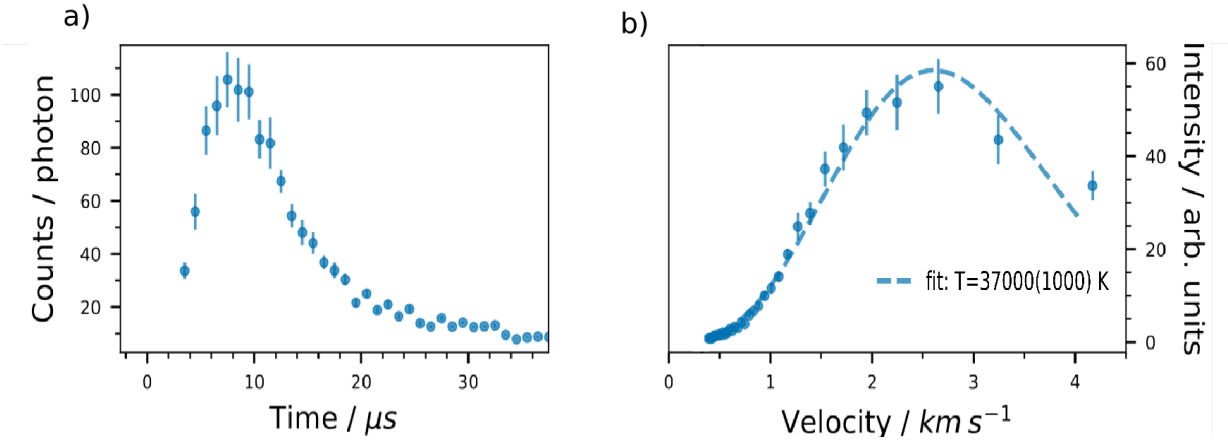


Figure 5.1: Ablation TOF spectrum of $BaCl_2$. a) shows the time of flight distribution. b) Shows the velocity distribution fitted to a Maxwell-Boltzmann distribution. A plume temperature of $37{,}000 \pm 1{,}000$ K and a peak velocity of $2{,}600 \pm 50$ m/s is estimated from this data. Taken from [70, 8].

.

small number of atoms in that velocity class. Here, loading rate refers to the number of ions trapped per ablation pulse. The experimental setup in [70, 8] uses a linear 4-rod trap and they reported loading rates of 1 ion trapped per ablation pulse for ^{138}Ba from $BaCl_2$ ablation targets. This is expected to be much lower for a surface-electrode trap due to its shallow trap depth, especially during initial trapping attempts when experimental parameters have not yet been optimized with a trapped ion.

5.2.2 Trap depth of the Phoenix trap

To estimate what the highest velocity of atoms we would be able to trap with the Phoenix trap, we need to estimate its trap depth. The trap depth is the maximum potential energy barrier the ion must overcome to escape the trap. It corresponds to the difference between the RF null and the saddle point of the potential. From the Phoenix trap manual [54], the trap depth in the radial directions is expressed as

$$D = \alpha \frac{1}{2} m \omega_i^2 R^2 \quad \alpha = 0.028 \tag{5.1}$$

where α is a geometric factor, m is the mass of the ion, and ω_i are the radial secular frequencies

In section 2.2.1, we found that the secular frequency is given by $\omega_i \cong \frac{1}{2}\Omega_{RF}\sqrt{a_i + \frac{1}{2}q_i^2}$. Under normal operating conditions $a_i \approx 0$, and the expression simplifies to

$$\omega_i = \frac{QV_0}{\sqrt{2}\Omega_{RF}mR^2} \tag{5.2}$$

for the 4-rod Paul trap, R was the distance from the RF electrodes to the center of the trap. This formula can be used to calculate the secular frequency of the Phoenix trap by replacing R with the characteristic distance of the Phoenix trap. The characteristic distance corresponds to the distance at which hyperbolic electrodes (such as in the 4-rod trap) operating at the same RF voltage and drive frequency would generate the same secular frequency as in a surface-electrode trap [54]. For the quantum zone of the Phoenix trap, the characteristic distance is

$$R = 140\,\mu\text{m} \tag{5.3}$$

The radial secular frequency is directly proportional to the RF voltage amplitude. The RF rail electrode on the Phoenix trap is rated for maximum RF voltage of $\pm 180\,\text{V}$. This corresponds to a secular frequency $\omega_i = 2\pi \times 3.62\,\text{MHz}$ and a trap depth of $D = 3.14 \times 10^{-20}\text{J}$ or $0.196\,\text{eV}$ for $^{133}\text{Ba}^+$ ions. This should be the maximum achievable trap depth given the $\pm 180\,\text{V}$ voltage limit. However, we need to be careful when increasing the RF voltage of trap, as that also increase the q-parameter q_i in the Mathieu equation. The q-parameters determines how strongly the ion feels the oscillating RF field. If q_i is too small, the RF field is too weak to confine the ion. If q_i is too large, the ion's motion becomes unstable. For surface-electrode traps, a q-parameter between 0.1 and 0.3 is generally recommended [27]. In section 2.2.1, we found that the q-parameter is given by

$$q_y = -q_x = \frac{2QV_0}{mR'^2\Omega_{RF}^2} \quad \text{or} \quad q_y \approx \frac{2\sqrt{2}\omega_y}{\Omega_{RF}} \tag{5.4}$$

For $V_0 = \pm 180\,\text{V}$ we get a q-parameter of 0.311 which means we would like to have a lower RF voltage amplitude for stable trapping. For a q-parameter of 0.29, the RF voltage must be $\approx 167\,\text{V}$. This gives us a secular frequency of $\omega_i = 2\pi \times 3.36\,\text{MHz}$ and a trap depth of $D = 2.70 \times 10^{-20}\,\text{J} = 0.168\,\text{eV}$. To estimate the maximum velocity v_{max}, the ablated atoms can have in order to be confined by the trap, we can equate the trap depth to the atom's kinetic energy.

$$D = \frac{1}{2} m v_{max}^2 \Rightarrow v_{max} = \sqrt{\frac{2D}{m}} \tag{5.5}$$

For a trap depth of 0.168 eV, the corresponding maximum trappable velocity is $v_{max} \approx 495\,\mathrm{m/s}$. As shown in Fig. 5.1, this velocity falls at the lower end of the ablation plume's velocity distribution, where relatively few atoms reside. As a result, successful trapping in this regime depends on the sparse population of slow-moving atoms in the low-energy tail of the Boltzmann distribution, resulting in reduced loading rates when using $BaCl_2$ targets.

5.3 Barium metal

The predominance of fast moving atoms in the ablation plume from $BaCl_2$ targets leads to lower loading rates, making ion trapping with salt targets particularly challenging especially during initial trapping attempts when system parameters such as trap voltages, laser powers and frequencies, and beam alignment have not yet been optimized. These parameters need the presence of trapped ion to be optimized to the full extent. A metallic barium source could fix this issue as metallic ablation targets have been shown to have plume velocities that are typically two orders of magnitude slower compared to salt ablation targets [59]. The slower plume velocities mean that atoms generated from metallic targets are more easily confined within the trap's potential well leading to higher loading rates.

This is no known commercial source of radioactive metallic ^{133}Ba. A recipe for producing ^{133}Ba metal from ^{133}Ba in the form of $BaCl_2$ is outlined in [22], but this has not yet been attempted. Therefore, it is not yet possible to produce ^{133}Ba atoms from a metallic ablation target. However, barium metal with natural isotopic abundance is commercially available. The most abundant isotope in naturally occurring barium is ^{138}Ba. Fig 5.2 shows a neutral fluorescence frequency scan after ablation of a $BaCl_2$ target, showing the relative abundance of different isotopes. ^{138}Ba has a nuclear spin of $I = 0$, which means it exhibits no hyperfine structure and cannot be used to encode hyperfine qubits. Nonetheless, it can still be trapped. Due to its abundance in natural barium metal and the relatively slow velocities of atoms emitted from metal ablation, ^{138}Ba is well-suited for initial loading attempts in surface-electrode ion traps with low trap depths. Thus, for early stage trapping experiments, ^{138}Ba can be trapped from a metallic barium ablation target and used for optimization and system calibration before we move on to $BaCl_2$ ablation targets.

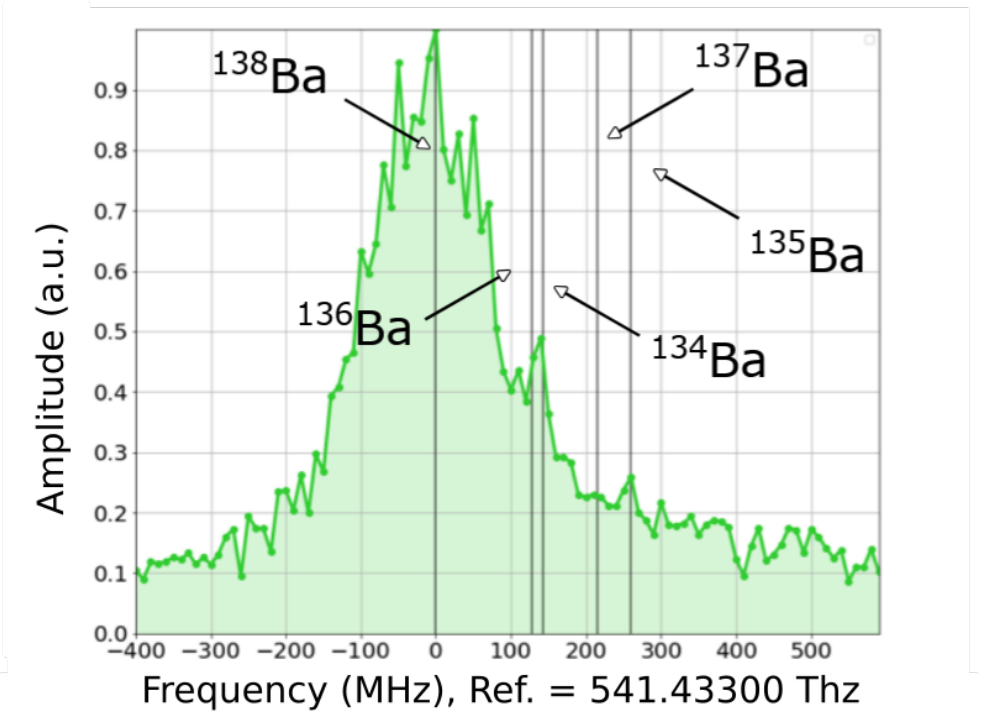


Figure 5.2: PMT counts as a function of the frequency of the 553 nm laser after ablation of $BaCl_2$ ablation targets. We can see that the most abundant isotope is ^{138}Ba, but other isotopes are also clearly present. The ^{138}Ba peak occurs at 541.43300 THz. Taken from [22].

5.3.1 Neutral fluorescence and TOF

Before incorporating a metallic barium ablation target into our system, we need to first check two key points:

1. That our ablation setup can successfully produce neutral barium atoms from a metallic target. This is done by confirming neutral fluorescence of barium atoms after an ablation pulse. Basically, a 553 nm laser will intersect the atomic plume generated from an ablation pulse and if barium atoms are present in that plume, the $6s^2\,{}^1S_0 \leftrightarrow 6s6p\,{}^1P_1$ transition in neutral barium will be excited. The atoms in the plume will emit lots of photons which will be collected by a PMT. We can see from Fig. 5.2 that ^{138}Ba is the most abundant isotope whose peak occurs at 541.4330 THz, so the 553 nm laser will be locked to that frequency.

2. That the resulting atomic plume from the metallic target contains a significantly larger number of slower moving atoms compared to the $BaCl_2$ target. Specifically, atoms with velocities $\leq 495\,\mathrm{m/s}$, which are trappable given our current trap depth. This velocity of the plume can be measured using TOF spectroscopy just as was done in the plots shown in Fig 5.1. The TOF measurements of metallic barium can then be compared to those in Fig. 5.1 and the depth of our trap.

Experimental setup

The neutral fluorescence and TOF experiments are conducted in a small vacuum chamber at HV ($\approx 1 \times 10^{-4}\,\mathrm{mbar}$) from Kimball physics (53-180000). The pressure does not need to be in the UHV regime like our main experimental chamber used for trapping ions, as neutral fluorescence measurements are typically performed immediately following laser ablation and over short timescales (on the order of microseconds to milliseconds). During this brief period, collisions with background gases are minimal and do not significantly affect the dynamics or detection of the neutral atoms.

The experimental setup is depicted in Fig. 5.3. The barium metal samples were procured from Luciteria Science and supplied in the form of small chunks, each a few millimeters in size. Fig. 5.6 a) shows the barium metal chunks. The metal is mounted in the chamber with adhesive tape approximately 11 mm from the center of the chamber, as shown in the inset of Fig. 5.3 a). The 553 nm laser passes through the center and drives the $6s^2\,{}^1S_0 \leftrightarrow 6s6p\,{}^1P_1$ transition and is positioned orthogonal to the surface norm of the ablation target to reduce Doppler broadening. The ablation laser used is a solid state Nd:YAG laser operated at 532 nm, sourced from RPMC Lasers Inc. The pulse fluence of the ablation laser used in the experiments was $0.665\ \mathrm{J/cm^2}$. The photons emitted from the atoms after each ablation pulse are collected using a 1 inch diameter objective lens with a NA of 0.26 and a working distance of 43 mm, and detected by a Hamamatsu (H10682-210) PMT.

The pulse sequence for the neutral fluorescence and TOF experiments is shown in Fig. 5.3 d). The ablation pulse arrives at the metal target $\sim 75\,\mu\mathrm{s}$ after the start of the experiment. The pulse width is $< 1\,\mathrm{ns}$, photons are collected after a delay of $t_d\,\mu\mathrm{s}$ after the ablation pulse with a collection window of $\Delta t\,\mu\mathrm{s}$. For the neutral fluorescence experiment, $t_d = 10\,\mu\mathrm{s}$ and $\Delta t = 20\,\mu\mathrm{s}$. For the TOF experiments, the delay time t_d is scanned, allowing selective detection of fluorescence from atoms arriving at the 553 nm laser beam at different times, corresponding to different atomic velocities. Since faster atoms reach the detection region (intersection of the 553 nm laser and the atomic plume) earlier and slower atoms

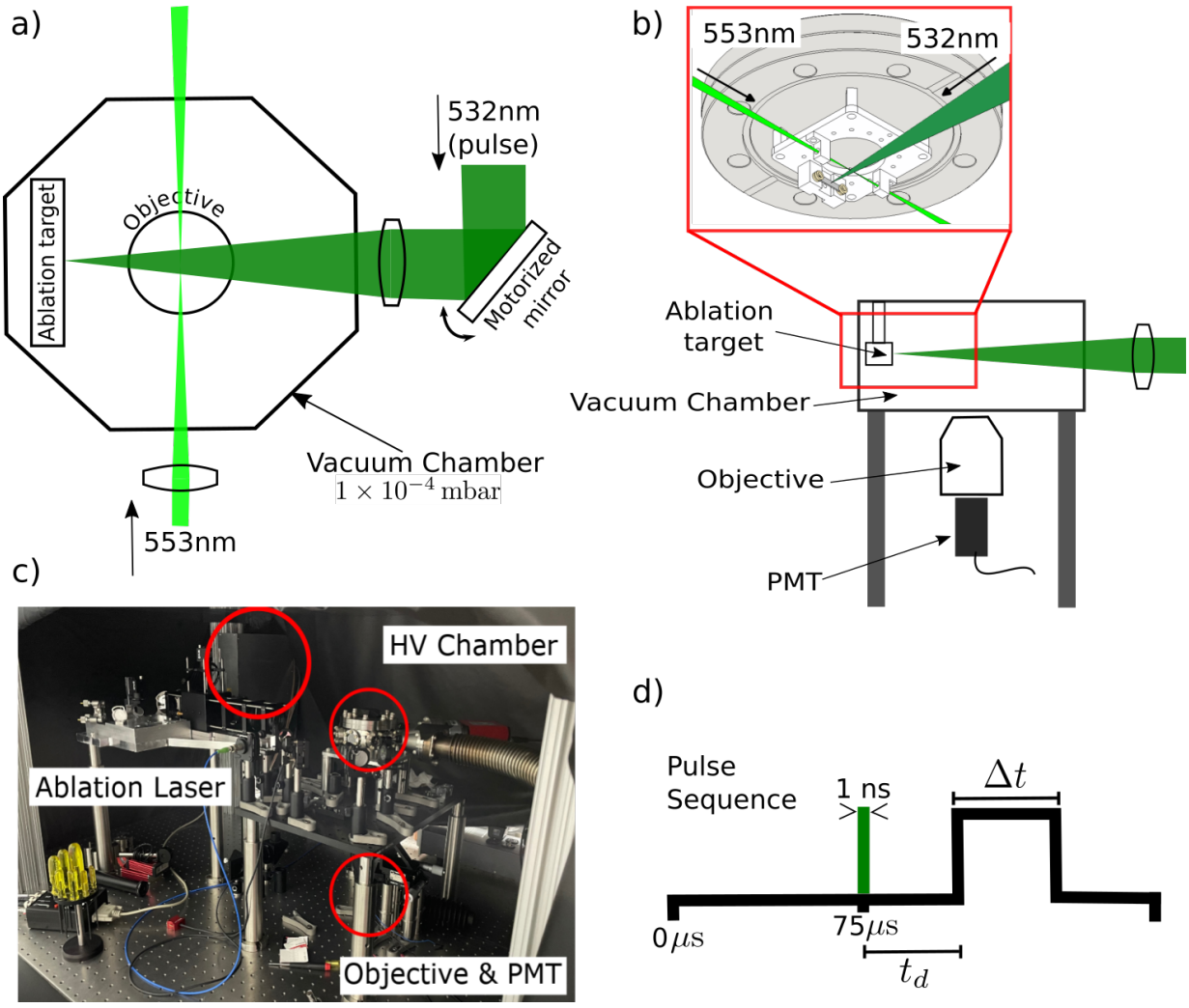


Figure 5.3: Experimental setup of the barium metal neutral fluorescence and TOF experiments. a) and b) show a diagram of the experimental setup, showing the beam orientations. The target is placed d=11.35 mm from the 553 nm laser . The inset in b) shows a CAD rendering of the ablation target holder. c) Shows an image of the actual setup in the lab. d) Pulse sequence for the experiments. 0 μs marks the beginning of the experiments when the trigger signal is sent to the ablation laser. The ablation pulse arrives $\sim 75\,\mu$s after the experiment is started. The PMT starts registering photon counts after a delay of t_d after the ablation pulse for a collection window of Δt. Adapted from [22].

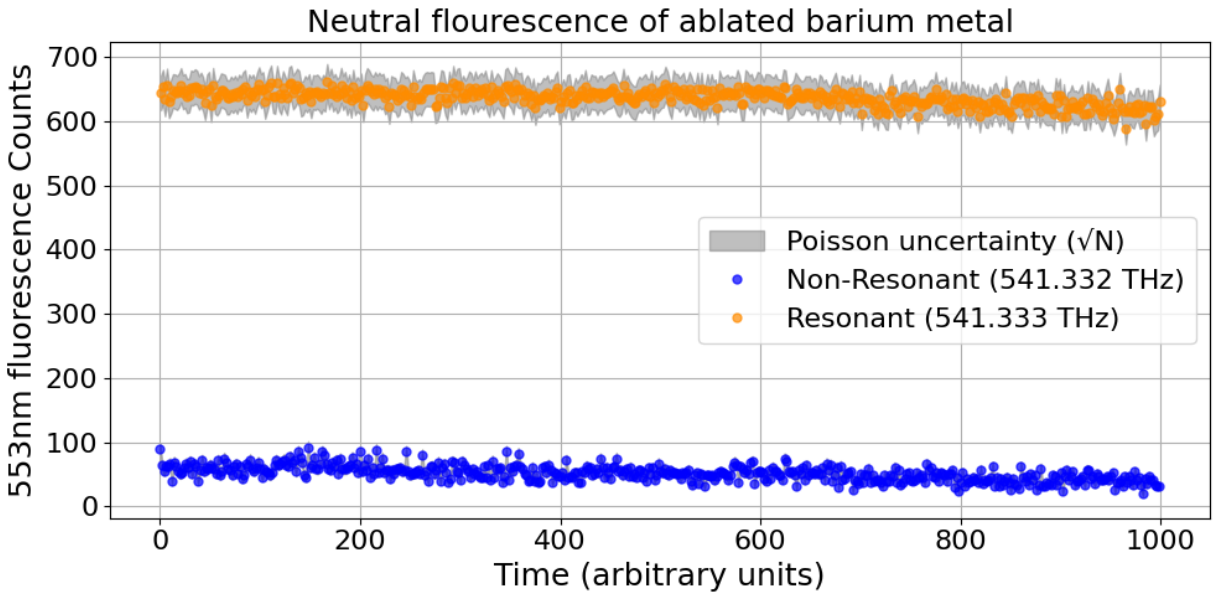


Figure 5.4: Neutral fluorescence of ablated barium metal. Each ablation pulse of the 553 nm laser is switched between the resonant and non-resonant (1 GHz detuned) frequency to compare background counts to the signal from the barium atoms. We see a clear distinction in fluorescence counts between the resonant and non-resonant case which confirms that we are able to produce neutral barium atoms from ablation of barium metal.

arrive later, varying t_d effectively samples the velocity distribution of the ablated atoms. $\Delta t = 2\,\mu$s for the TOF experiments.

The 553 nm laser is frequency locked with a Highfiness wavemeter (WS8-2). For both the neutral fluorescence and TOF experiments, the frequency of the 553 nm laser is detuned 1 GHz off-resonance for every other ablation pulse, which allows background counts to be compared to counts from ^{138}Ba atoms.

Experimental results

Fig. 5.4 shows the results of the neutral fluorescence experiments. It shows the 553 nm photon counts for both when the 553 nm laser was on-resonance and off-resonance (1 GHz detuned). We can clearly see much higher counts when the 553 nm was on resonance. This confirms the production of neutral barium atoms from laser ablation of barium metal.

Fig. 5.5 shows the TOF results. Fig. 5.5 a) tells us the distribution of times atoms

arrive at the 553 nm beam. We know the fixed distance from the ablation target to the beam, d = 11.35 mm and we can use that to find how fast the atoms are moving. We need to account for the transit time of the atoms through the 553 nm beam. Faster atoms produce less fluorescence as they spend less time in the beam and vice versa. Therefore, slower moving atoms are overrepresented in the arrival time distribution. We must scale the data by $1/t_d$. The result is the velocity distribution shown in Fig. 5.5 b).

In Fig. 5.1 a), the fluorescence signal is almost gone at around 38 μs. However, for barium metal the signal lasts much longer, extending to around 1750 μs. We would like to compare the peak velocity of the barium metal targets to the $BaCl_2$ targets. Ideally, we would fit the velocity distribution of the barium metal to a Maxwell–Boltzmann distribution similar to Fig. 5.1 b). However, this was not possible for the data shown in Fig. 5.5, as the ablation laser pulse coincided with the fastest-moving atoms produced during the barium metal ablation. Another possible explanation for the discrepancy is that the photomultiplier tube becomes momentarily blinded by the intense initial flash of light from the ablation. During recovery, the PMT can exhibit artificially elevated counts, leading to an overestimation of the fluorescence signal in the early part of the time-of-flight trace. Therefore that part of the data was discarded which explains why Fig. 5.5 b) does not have the high-energy tail of the Boltzmann distribution which is present in Fig. 5.1 b). So, the data in Fig. 5.5 b) could not be fit to a Maxwell-Boltzmann distribution to extract a peak velocity.

However, the maximum in the observed velocity distribution in Fig. 5.5 b) corresponds to a well-populated velocity class and can be taken as a lower bound for the peak velocity. From the velocity distribution in Fig. 5.5 b), this peak velocity is $v_{\text{peak}} = 333.8\,\text{m/s}$, which is below the maximum velocity of 495 m/s corresponding to the trap depth of our ion trap. We see a significant level of neutral fluorescence near velocities of $v_{\text{peak}} = 333.8\,\text{m/s}$, which confirms the presence of many atoms with velocities slower than 495 m/s. In Fig. 5.1 b) the fluorescence signal from $BaCl_2$ for atoms slower than 495 m/s is very small. This suggests that we should expect a larger number of atoms at speeds slower than 495 m/s from the barium metal source, although we cannot be more quantitative about the exact proportion. Thus, with a large number of atoms in the ablated plume from barium metal having velocities lower than 495 m/s, we can be certain that significantly higher loading rates will be observed when trapping from the barium metal atomic source. We can therefore incorporate this source into our system and use it for initial trapping attempts to optimize and calibrate our system.

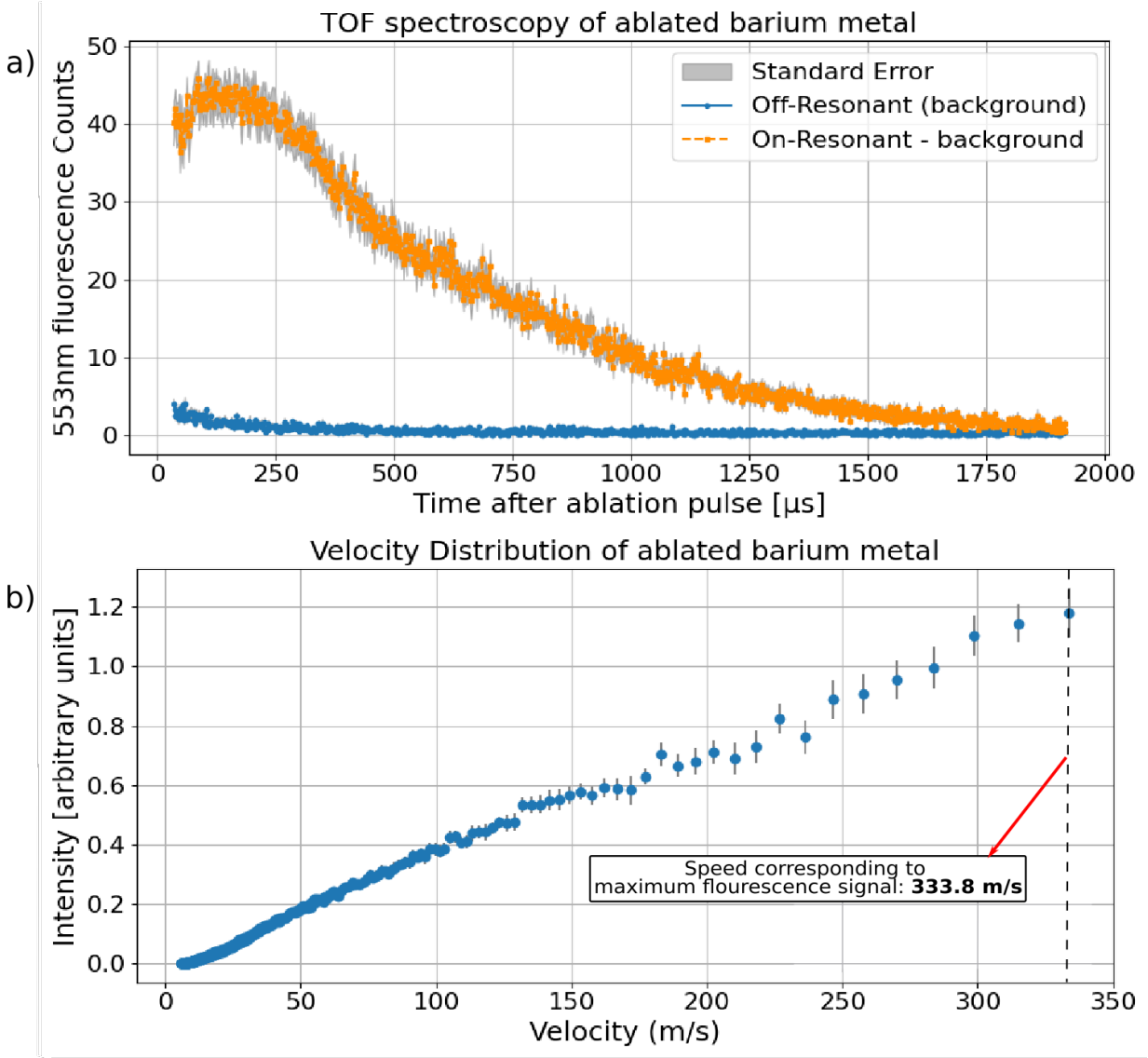


Figure 5.5: TOF spectroscopy results of ablated barium metal. a) Shows the TOF distribution. b) Velocity distribution obtained by scaling the TOF data in a) by $1/t_d$ and converting to velocity. A "peak" velocity corresponding to the maximum fluorescence signal $v_{peak} = 333.8\,\mathrm{m/s}$ is obtained.

5.3.2 Barium metal oxidation

The relatively slow velocity of the atomic plume generated from barium metal makes it an attractive atomic source for barium-based trapped ion systems. However, barium's high reactivity poses a significant challenge, as it readily oxidizes, making it difficult to handle and maintain in experimental conditions.

Barium is a highly reactive alkaline earth metal, classified in Group IIA of the periodic table. Due to its extreme reactivity, barium is never found in nature in its elemental form, it only exits in a combined state with other elements. Pure barium metal is soft and initially exhibits a silvery-white appearance. However, this metallic sheen rapidly disappears upon exposure to moist air, forming a dull gray layer of barium oxide (BaO) on the surface. To prevent this rapid oxidation, commercially available barium metal is typically packaged either under oil or sealed in glass ampules filled with inert argon gas. For use in UHV systems, barium packaged under argon is preferred, as oil is incompatible with UHV environments due to its high outgassing rates. Figure 5.6 shows the barium metal chunks procured from Luciteria Science, sealed in an argon-filled glass ampule. Figure 5.6 illustrates how quickly the metal oxidizes when exposed to air after breaking the glass ampule.

A surface layer of barium oxide on the metal target can severely affect system performance by

1. **Altering the atomic plume**. The oxide layer on the barium metal can lead to unreliable atom production during laser ablation and introduce unwanted scattering of the ablation beam. Additionally, the presence of oxide can alter the surface geometry of the ablation target such that the surface normal no longer points toward the trapping region. This misalignment can significantly reduce ion loading rates. In our experiments, we found that the oxide layer could be effectively removed by operating the ablation laser at a higher fluence. Once the oxide was cleared from a particular spot, we were able to reliably generate neutral barium atoms from that location, consistent with the observations in Ref. [59]. However, the underlying surface geometry may still remain distorted, so it is preferable to minimize the formation of the oxide layer in the first place.

2. **Introduces contamination**. As seen in Fig.5.6 b), the BaO layer on the barium metal appears rough and flaky. This oxide layer tends to flake off the ablation target and can be ejected during ablation, posing a significant contamination risk to the surface-electrode trap. The ablation target is located approximately 14 mm from

the trap electrodes and has a direct line of sight to the trap. Consequently, BaO particles may reach and contaminate the electrodes, potentially leading to issues such as electrical shorting or charge build-up. While it is possible to produce barium atoms from an oxidized metal target, minimizing the formation of BaO is crucial to reduce these contamination risks.

The barium metal is most susceptible to air exposure during the assembly of the ablation targets and vacuum chamber. To minimize oxidation during this stage, we implemented several precautionary methods, which are discussed in chapter 6 of this thesis.

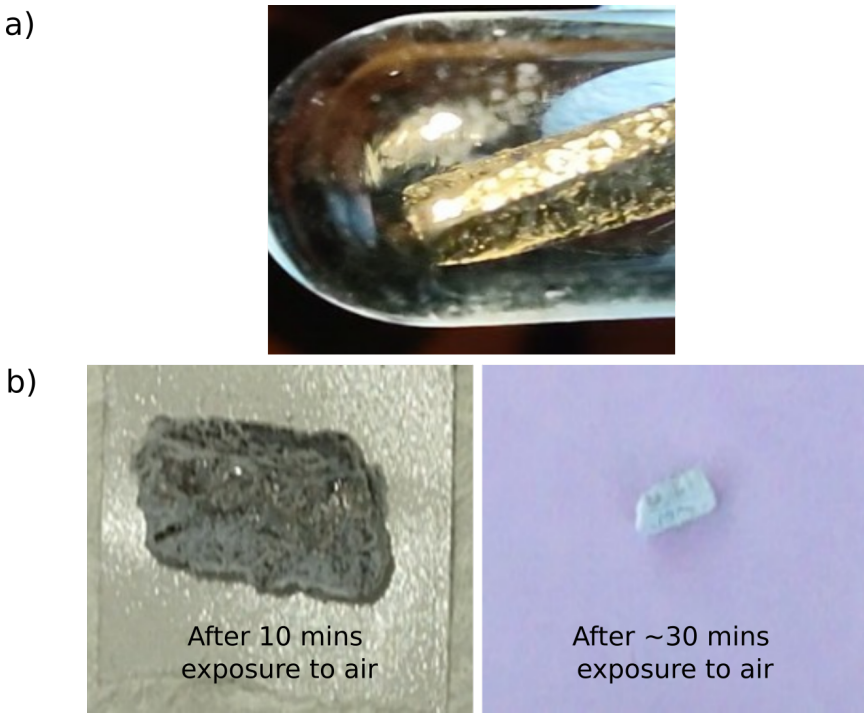


Figure 5.6: Images of the barium metal source and its oxidation. a) Image of the barium metal chunk inside a sealed glass ampule filled with inert argon gas to prevent oxidation. We can see it has a clear metallic sheen before it oxidizes. b) Images of the barium metal after being exposed to air for 10 and 30 minutes respectively. After 10 minutes we can see some white BaO appear on the surface and after 30 minutes it turns completely white. The oxide easily flakes off the metal and can contaminate the surface-electrode trap.

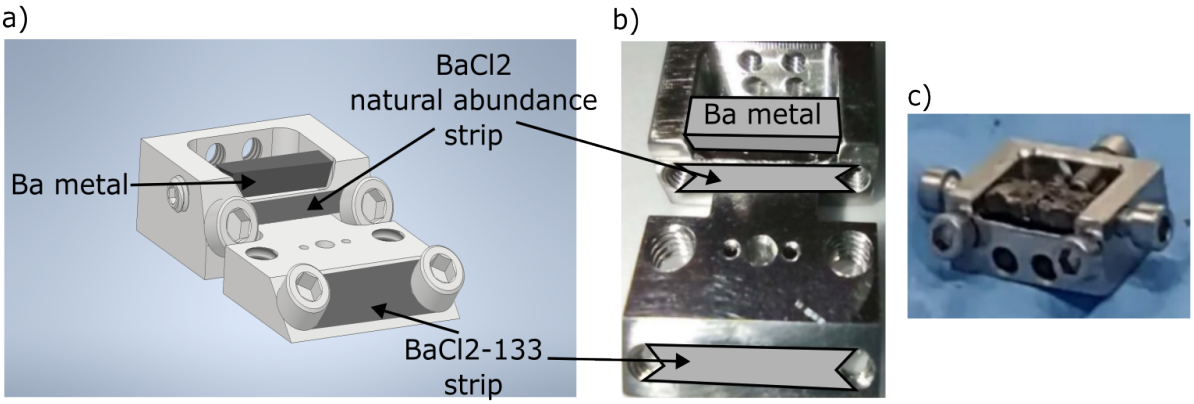


Figure 5.7: The ablation target holder used in the QuantumIon system. a) Shows a CAD rendering of the ablation target holder. b) Shows an image of the ablation target holder indicating where each type of source will be installed. c) Shows the back part of the holder with a chunk of barium metal installed in it.

5.4 Ablation target holder

We have analyzed the feasibility of using a metallic barium target in our system and determined that the velocity of the atomic plume is indeed much slower compared to the $BaCl_2$ targets. With this, we will be including a total of 3 different types of atomic sources in our system

1. **$BaCl_2$ – 133**: This is the primary source of barium-133 used in our experiments.
2. **$BaCl_2$ – Natural abundance**: Used for system calibration for the salt targets before using the radioactive target. Can also be used for experiments involving other isotopes such as ^{137}Ba.
3. **Ba metal - Natural abundance**: Used for initial trapping attempts for system calibration and optical alignment of laser beams to the ions.

The internals of the QuantumIon vacuum chamber, including how the ablation targets are mounted inside, were designed without the metallic target in mind. Therefore, the previous ablation target holder had to be redesigned to incorporate the metallic target. The new target holder was designed by PhD student Akimasa Ihara and is shown in Fig. 5.7. The target is separable into two parts, one for the platinum strip with the

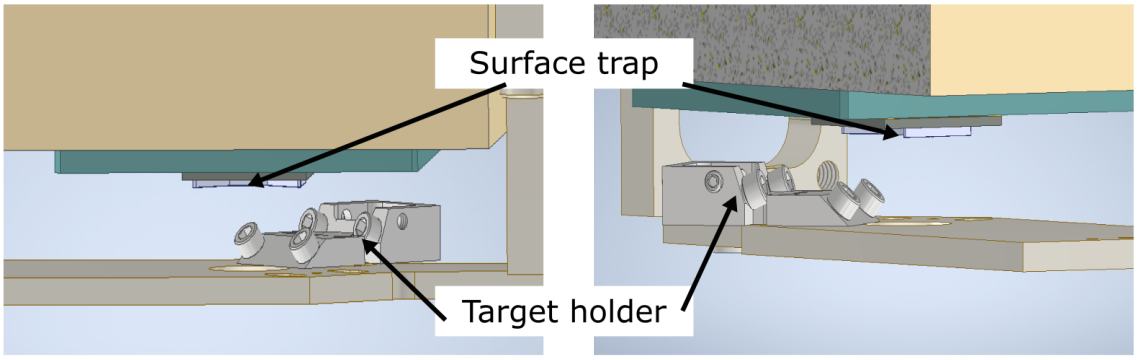


Figure 5.8: CAD rendering of two views of the ablation target holder and the surface-electrode trap. The targets are approximately 14 mm away from the trap. The surface normals of each target is directly pointed at the trapping region of the trap so that that atomic plume generated during laser ablation goes straight to the trapping region.

radioactive $BaCl_2$, and one for the nonradioactive $BaCl_2$ and barium metal. This is done so that the radioactive source can be prepared separately with the required radiation safety precautions, and the metallic source can be prepared inside a nitrogen filled glove box to minimize oxidation. The two parts are joined together before being installed in the vacuum chamber. Figure 5.8 shows a CAD rendering of how the ablation target holder is mounted relative to the surface-electrode trap.

5.5 Summary

In summary, this chapter demonstrates the difficulty of reliably trapping barium ions using $BaCl_2$ ablation targets in a surface-electrode trap due to the trap's shallow depth. The feasibility of a metallic barium target was investigated, and it was shown that atoms produced via ablation of metal targets are significantly slower than those from $BaCl_2$, making them more compatible with the limited trap depth. This suggests that using a barium metal target can lead to more reliable ion trapping, particularly during initial trapping attempts when experimental parameters have yet to be optimized. The ability to reproducibly generate slower atoms makes metallic barium a more convenient and systematic choice for initial ion loading in surface-electrode trap experiments. The chapter then discusses some of the technical challenges associated with using barium metal, particularly

its rapid oxidation, and presents the design and implementation of a multi-target holder that allows three different ablation targets to be mounted simultaneously in the vacuum chamber.

Chapter 6

In-vacuum wire harness and vacuum chamber assembly

We discussed in section 3.2 how the QuantumIon system distinguishes itself from most other surface-electrode ion trap systems by mounting the trap in the center of the vacuum chamber which provides improved optical access with low vacuum pressures. However, this configuration requires bringing the ~ 100 electrical connections to the Phoenix trap inside the vacuum chamber from a feed-through on the chamber to its center where the trap is mounted. Bringing such a high density of electrical connections inside a UHV environment without compromising the vacuum pressure can be non-trivial due to the high outgassing from the connections. This chapter discusses the implementation of a UHV compatible wire harness with ~ 100 individual connections made with commercially available components. Several iterations of the wire harness were built and tested with new issues being discovered at each iteration.

This chapter then proceeds to describe the assembly process of the QuantumIon vacuum chamber. This includes the installation and alignment of the wire harness and surface-electrode trap assembly, as well as the integration of both radioactive and metallic barium ablation targets. It also covers the procedure for sealing the chamber, achieving UHV pressures, and transporting the assembled chamber from the cleanroom to the laboratory. Several factors make this assembly process far more complicated than a typical vacuum chamber assembly

1. **Radioactive atomic source.** Extra precautions must be taken to ensure minimal radiation exposure to lab personnel. Additionally, we have only one sample of the radioactive source, and obtaining a replacement could take several months. Therefore,

it is crucial that we handle the source with great care to avoid any waste or failure during the procedure.

2. **Rapid oxidation of the barium metal source.** The barium metal oxidizes within seconds upon exposure to air, forming a surface layer of barium oxide that negatively affects atom production. Because of this, chamber assembly steps involving the barium metal target are highly time-sensitive and must be performed quickly and carefully to minimize air exposure. .

3. **Limited baking window for Phoenix trap.** Vacuum chambers must be baked for several days to a few weeks to achieve UHV pressures. The baking is necessary to remove adsorbed gases (most dominant being water vapor) from the chamber walls. The Phoenix trap, however, has a strict thermal constraint: it must not be baked for more than seven days in total, and at temperatures no higher than 200° C. Exceeding these limits can lead to the formation of gold–aluminum intermetallic compounds at the wire bonds connecting the trap electrodes to the trap CPGA, which are extremely brittle and can cause bond failure, rendering the trap inoperable. Because this seven-day limit is cumulative, we aim to bake for significantly less time (typically around two days) with the trap installed to allow headroom for potential reassembly and re-baking if necessary. Therefore, it is crucial that all parts of the assembly are done correctly to ensure we achieve low UHV pressures within 2 days of baking with the trap and to ensure we do not have to repeat the baking process. As we only possess one Phoenix trap and procuring a replacement can take several months, strict adherence to these baking constraints is critical.

These factors make the assembly of our vacuum chamber quite complicated. The process requires a high degree of coordination, careful timing, and detailed planning to ensure that all steps are carried out successfully without compromising any components. Each constraint adds a layer of complexity that demands precise execution and collaboration between lab members. To manage this complexity, we conducted multiple practice runs of the assembly procedure, which allowed us to refine our workflow and minimize the risk of errors during the final assembly.

Author contributions: The assembly of such a large and complex vacuum chamber system required the coordinated efforts of many people. For the work presented in this chapter, the author led the assembly of the in-vacuum wire harness and carried out much of the soldering and mechanical assembly. This harness required numerous assembly steps and multiple iterations, so wire preparation and electrical testing were distributed among lab members, including PhD students Akimasa Ihara and Hawking Tan.

The author, together with PhD students Akimasa Ihara and Hawking Tan, and post-doctoral researcher Dr. Akbar Jahangiri Jozani, assembled the vacuum chamber system. This process involved several months of test fitting various chamber internals, pre-treating components, aligning the trap assembly, sealing, baking, and leak-checking the chamber. For the final assembly, specific roles were assigned: Hawking Tan prepared the $BaCl_2$ ablation target strips; Dr. Akbar Jahangiri Jozani prepared the metallic barium ablation target; and the author, along with Akimasa Ihara, assembled and installed the ablation target holders and the Phoenix trap. All members contributed to the final sealing and bakeout of the chamber.

During this final stage, PhD student Collin J. C. Epstein and the group's PIs, Prof. Rajibul Islam and Prof. Crystal Senko, were present for key decision-making and documentation. Special thanks go to Lewis Hahn from the QITI lab for assistance during final assembly, and to Katelyn Versteeg, the university's radiation safety officer, for supervising the radiation safety of the entire procedure.

6.1 UHV compatible in-vacuum wire harness

The ultimate pressure of a vacuum chamber is determined by the rate at which gases are entering or being produced inside the chamber and the rate at which those gases are being pumped out. At UHV, most of the gas originates inside the chamber from the chamber's walls and internal components. This is known as outgassing. Different surfaces in a chamber outgas at different rates which are typically measured in mbar l/s. The gas load inside the chamber is removed by means of vacuum pumps. The rate at which a vacuum pump removes the gases is known as the pumping speed, measured in liters per second (l/s). The ultimate pressure inside the chamber is given by

$$P_{ult} = \frac{Q_{gas}}{S_{eff}} \tag{6.1}$$

where P_{ult} is the ultimate pressure, Q_{gas} is the gas throughput/outgassing in the chamber. S_{eff} is the effective pumping speed available at the chamber which depends on the pumping speed of the vacuum pump and effective conductance of the fittings and pipes that connect the pump to the chamber. It is clear from Eq. (6.1) that in order to achieve lower vacuum pressure we either need to reduce the outgassing inside the chamber as much as possible or increase the effective pumping speed.

The local pumping speeds for various gas species typically range from around 1 l/s to around 1000 l/s, while the outgassing rates for different elements encompass at least eight orders of magnitude, from 10^{-7} mbar l/s cm^2 to 10^{-15} mbar l/s cm^2 [34]. Consequently, only augmenting the pumping speed is not invariably the optimal approach for attaining low pressures; the mitigation of the outgassing rate of components is equally critical to vacuum efficacy. Therefore, when devising a wiring solution to provide around 100 electrical connections to the centrally positioned surface-electrode trap in our chamber, it is imperative to ensure that this solution does not result in outgassing rates sufficient to hinder us from achieving UHV pressures.

Fig. 6.1 a) shows a CAD rendering of how the Phoenix trap is mounted inside the experimental chamber. The trap CPGA mounts into a ZIF socket made out of PEEK (Tactic Electronics, part no. 100-4680-003A). PEEK is a high performance thermoplastic polymer commonly used in UHV applications due to its excellent mechanical strength, thermal stability, and chemical resistance. It can withstand bake-out temperatures up to around 250° C and has relatively low outgassing compared to most plastics, making it suitable for use in UHV systems when used in limited quantities. The ZIF socket has conductive pins on the opposite side, which slot into a custom-designed PCB and are soldered in place using UHV compatible solder and flux. This PCB+ZIF socket assembly is then mounted onto a stainless steel bridge that is secured inside the experimental chamber. The PCB+ZIF assembly is shown in Fig. 6.1 b). We can see in Fig. 2.8 and Fig. 6.1 b) that the pin layout of the trap CPGA and ZIF socket is very dense, making it difficult to directly solder wires to them. To address this, a custom PCB is used to fan out the connections to a more manageable and accessible layout that facilitates easier soldering.

To bring the approximately 100 DC and RF electrical connections from outside the vacuum chamber to the inside, the minimum standard connector that can be easily welded onto a vacuum flange is a micro-D connector, which provides 100 pins with a 0.05-inch pitch. Now, the difficult part is to bring electrical connections from the vacuum side of this feedthrough to the PCB. The solution for this was to use a commercially available in-vacuum wire harness. This wire harness features a micro-D connector made from PEEK which is connected to 100 Kapton insulated wires. Kapton insulated wires are the industry standard for UHV applications due to their high temperature tolerance (bakeable upto to 250°) and low outgassing. The micro-D connector mates with the micro-D feedthrough inside the chamber and then each Kapton insulated wire is soldered on the PCB. The in-vacuum wire harness and how it's soldered to the PCB is shown in Fig. 6.2.

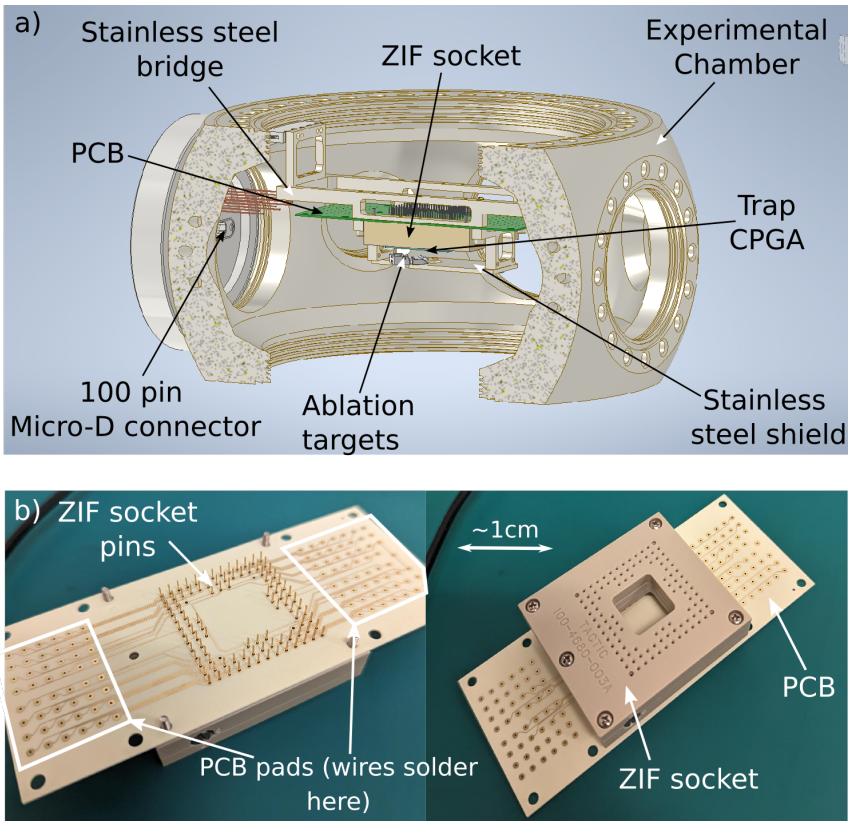


Figure 6.1: Mounting of the Phoenix trap inside the experimental chamber and the PCB + ZIF socket assembly. a) Shows a CAD rendering of how the Phoenix trap is mounted inside the experimental chamber. b) Shows images of the PCB + ZIF socket assembly. The trap CPGA mounts in the ZIF socket. The PCB distributes the dense pin layout of the ZIF socket to a more accessible layout for easier soldering.

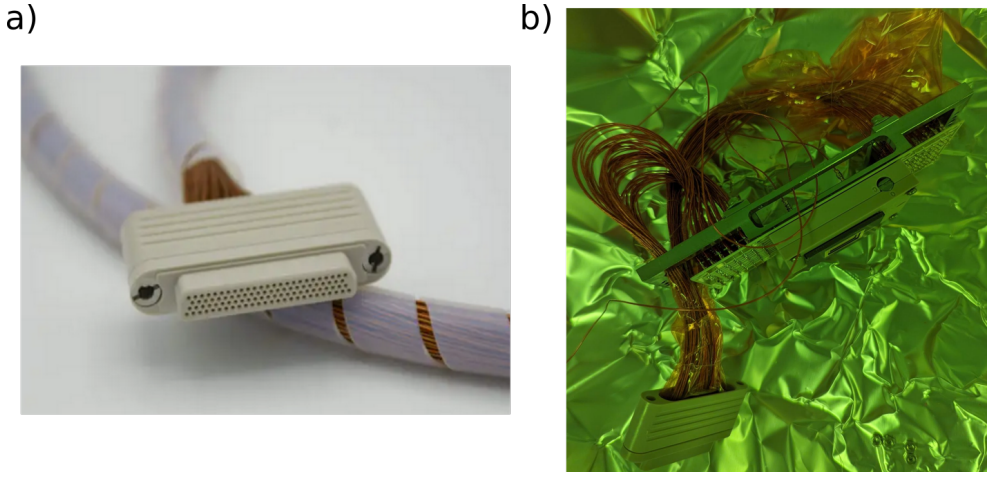


Figure 6.2: Image of the Micro-D wire harness and how it interfaces with the Phoenix trap. a) Image of the commercially available Micro-D connector wire harness made with PEEK (beige connector in b) and Kapton insulated wires. The PEEK connector mates with the Micro-D socket on the feedthrough flange and the wires are soldered onto the PCB shown in Fig. 6.1. b) Image of the wires harness soldered to the PCB.

Base pressure tests with all of these components installed in the vacuum chamber were conducted by previous students, and it was confirmed that UHV pressures could be reliably achieved. All of these components except the Phoenix trap are pre-treated before installation into the vacuum chamber. This includes pre-baking them for $\sim$ 5 days in a tube furnace to remove water, bulk hydrogen and any other gases that may be adsorbed onto their surfaces, which could otherwise outgas during operation and prevent the system from reaching UHV pressures. They are also cleaned by sonicating them in IPA to remove any surface contaminants that could compromise vacuum quality. Pre-baking of stainless steel parts is done at 400°C first under vacuum and them exposed to air to let a very thin oxide layer form on it. This oxide layer prevents any residual moisture or gases in the steel from escaping and contributing to the pressure load of the chamber. The PCB and ZIF socket are pre-baked at 150°C.

6.1.1 Issues encountered

Several iterations of the wire harness assembly were built, with new issues identified during each stage. These issues are discussed below.

Difficulty in soldering

Soldering the ZIF socket and wires to the PCB proved to be quite difficult due to the high density of the PCB pads and traces which can be seen in Fig. 6.1 b). Some of the PCB traces are only separated by a 1 mm gap. The PCB was designed to make the pads and traces as far apart as possible given the spatial constraints of the experimental chamber. The high density of the pads and traces made it difficult to access certain pads with a soldering iron without accidentally touching neighboring pads and traces. Touching neighboring PCB traces with a hot soldering iron can very easily damage and brake the traces which can render parts of the PCB inoperable. This also leads to the frequent development of shorts between neighboring traces and pads during soldering which in some cases was fixable but very risky as attempting to fix them easily ended up in irreversible damage to the PCB. The shorts can be caused by accidentally soldering two neighboring traces or pins together or even by any conductive contaminant settling between two traces. Such issues are not found during soldering of standard PCBs as they usually come with a solder mask (typically blue or green in color), which protects the sensitive PCB traces from high-temperature and mechanical forces. However, we can see that our PCB is completely white with no solder mask. This was done intentionally because when the PCBs with solder masks were pressure tested in our chamber by previous students, it was found that the solder mask outgasses too much which prevented the chamber from reaching UHV pressures. This makes sense as solder masks are typically epoxy based with organic compounds that have high outgassing rates. Therefore we had to use a PCB with no solder mask which left the PCB traces fully exposed and open to thermal and mechanical damage from the soldering iron.

Breaking of wires from the PCB

Initially the Kapton insulated wires were directly soldered to the PCB, but we quickly found out these wires were too weak and would easily break off at the solder joints especially after thermal cycling when the chamber was baked. We fixed this to some extent by adding crimp pins to the ends of the wires and soldering those onto the PCB. However, the wires were still quite sensitive to lateral forces at the crimp joint and we would occasionally find wires that had broken off during assembly and baking.

Flaking of Kapton insulation

Another unexpected issue that we ran into was that we started noticing flakes of the Kapton insulation coming off the Kapton wires especially after repeated sonication in IPA. The

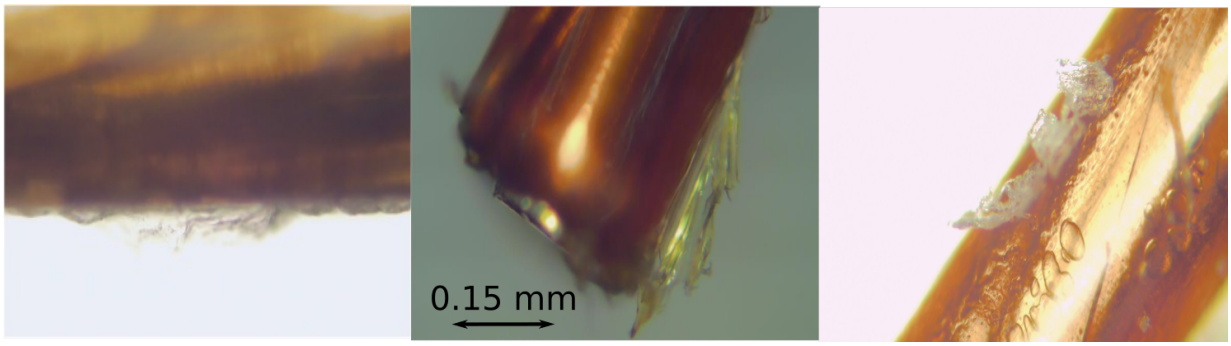


Figure 6.3: Microscope images of the flakes on the Kapton insulated wires. The images clearly show little flakes of the Kapton coming off of the wires. These flakes were found on the commercially available wires harness out of the box. The flaking got worse when the wires were sonicated in IPA to clean them. The Kapton wires are in close proximity of the surface-electrode trap (few centimeters) which means it is highly likely for these flakes to contaminate the trap's electrodes.

wires needed to be sonicated in IPA repeatedly to clean off solder flux from the soldering process as the flux is not compatible with UHV environments. Fig. 6.3 shows microscope images of the Kapton wires with the flakes clearly visible. We even found that a brand new wire harness that was claimed to be clean and ready for use by the manufacturer also produced Kapton flakes out of the box. Due to the close proximity of these wires to the surface-electrode trap, these Kapton flakes can contaminate the surface-electrode traps electrodes or wire bonds. This is highly probable especially during the initial pump down of the chamber from atmospheric pressures to low vacuum levels of around 10^{-3} mbar (known as roughing the chamber). During the initial pump down, the gas flow in the chamber can become turbulent or highly directional, potentially mobilizing the Kapton flakes and depositing them onto the surface-electrode trap. Such contamination can be highly detrimental as they can create electrical shorts on the trap or charge the trap electrodes.

6.1.2 Custom wire harness solution and assembly

The presence of these flakes on the commercially available wire harness meant that we had to implement one of our own with flake free Kapton wires sourced from a different vendor. It also meant we had to figure out a way to thoroughly clean the Kapton wires without sonication. Our implementation required careful selection of UHV compatible components.

Each component was chosen based on both vacuum compatibility and mechanical stability requirements, with special attention to preventing breakage of connections from the PCB during thermal cycling and installation. The components and tools used in the wire harness assembly are detailed in Appendix A.

The wire harness assembly follows a systematic procedure developed to address the issues discussed above. This procedure was refined over several months through multiple failed iterations of the wire harness. It consists of four critical stages: PCB and ZIF socket assembly, wire preparation, wire-to-PCB soldering, and connection of the PEEK micro-D connector. These steps, along with implemented solutions to minimize wire breakage and flaking, are detailed below.

PCB and ZIF socket assembly

The assembly begins with the soldering of the ZIF socket to the PCB. The ZIF socket pins slide into the through holes in the center of the PCB as can be seen in Fig. 6.1 b). We can see that the pins of the ZIF socket are very close together ($\sim 2\,\mathrm{mm}$). Soldering the ZIF socket pins onto the PCB is particularly challenging due to the high pin density, which makes it difficult to access the base of the pins without risking damage to nearby PCB traces. Unfortunately, the ZIF socket pin pattern is fixed, and the PCB trace layout cannot be significantly altered without increasing the board size which is constrained by the limited space available in the experimental chamber. As such, the only way to avoid damaging the PCB during soldering is through extreme caution and patience. The soldering is done with UHV compatible solder and flux made by Accu-Glass Products, Inc. The flux cannot be present inside a UHV environment, it is branded as UHV compatible as it is soluble in IPA which makes it easily to clean off after soldering. I gained considerable practice performing this soldering, and in the process, damaged several PCBs. Over time, I developed techniques to avoid damaging traces, such as approaching the PCB pads with the soldering iron from the direction opposite to the traces. I also determined that a soldering iron temperature of 400°C provided the best results, as it minimized contact time while ensuring proper solder flow. With sufficient experience, I was eventually able to complete the soldering reliably and without damaging the PCB.

As these parts are meant to go inside a UHV environment, the final assembly was soldered inside a class 10,000 cleanroom. The soldering station is prepared with a new soldering tip and the work area is covered with UHV compatible foil. The work area and all tools used are cleaned with IPA and cleanroom grade wipes. After the soldering is completed, the PCB + ZIF socket assembly undergoes sequential four-minute ultrasonic cleaning in soapy water, acetone, and IPA, with complete submersion during each stage.

After cleaning, each connection is visually inspected to verify proper solder flow and to check for any damage to the PCB traces.

Kapton wire preparation

The Kapton wires used in our harness were sourced from Accu-Glass Products, Inc. These wires exhibited less flaking compared to the commercially made wire harness shown in Fig. 6.2. However, any remaining flakes or contaminants had to be thoroughly cleaned before soldering and installation in the vacuum chamber to avoid compromising the integrity of the vacuum or contaminating the surface-electrode trap. Unlike other parts of the assembly, the wires cannot be cleaned through ultrasonic sonication in IPA as that leads to degradation of the Kapton insulation producing Kapton flakes. Thus, each of the 102 wires undergoes multiple cleaning passes by hand using cleanroom wipes dampened with IPA, alternating the wipe direction between passes to ensure complete surface cleaning. Following the IPA cleaning, the wires are given a final wipe with dry cleanroom wipes to remove any remaining solvent residues and particulates. To verify the effectiveness and safety of the cleaning process, random samples of the wires were inspected under a microscope. These inspections confirmed that the Kapton insulation remained intact and that the wires were thoroughly free of Kapton flakes and other contaminants.

In Fig 6.1 b) we can see that the PCB pads the wires solder to are organized in a grid pattern which means the length of each wire from the feedthrough to the PCB can be different depending on which row on the PCB that wire solders to. We could just cut each wire the same length and have extra wire in the vacuum chamber, but this is not great for vacuum quality as more wire means more outgassing from the wire harness which increases the gas load in the chamber. Thus, the distance from the micro-D feedthrough to each row on the PCB must be measured, and each corresponding wire must be cut to a length that ensures it reaches its PCB pad without tension while also minimizing excess wire within the chamber. Shorter wire lengths also ensures the wires maintain adequate clearance from high-temperature regions such as the close to the NEG pumps. To allow routing adjustments and crimp preparation, each wire is cut approximately 6–8 cm longer than its final measured length.

To alleviate the issue of wires breaking at the solder joints on the PCB, each wire is terminated with a crimp pin, which is then soldered onto the PCB. This approach provides a much stronger mechanical connection compared to soldering the wire directly to the PCB. To reduce wire density near the PCB pads and make soldering more manageable, some wires were soldered directly onto the ZIF socket pins (ZIF side) instead of the PCB pads (PCB side), with different types of crimp pins used for each connection. Initial mechanical

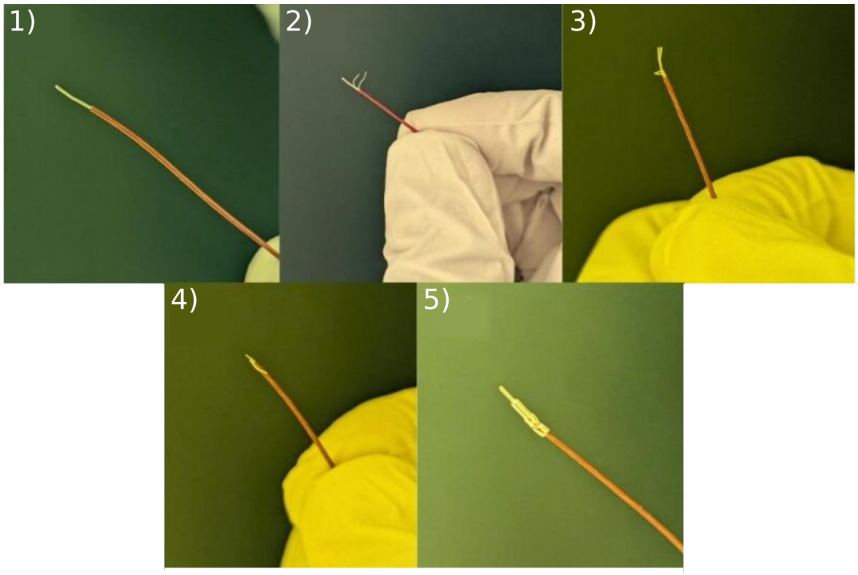


Figure 6.4: Wire crimping procedure for the PCB side crimp pins. 1) Strip a 4 mm section of the Kapton insulation. 2) Two strands of the stranded core wire are separated from the main bundle. 3) The two separated strands are trimmed 1 mm above the Kapton insulation. 4) Fold the stripped wire over the Kapton insulation. 5) Insert wire into the pin making sure the Kapton part is inside the pin and then crimp the pin.

tests revealed that wires remained prone to breakage at the crimp points. To address this, we developed a crimping procedure that ensured the Kapton insulation, not just the bare wire, was inserted into the crimp pins. This allowed the crimp pins to form a tighter, more secure grip on the wires. Since the Kapton insulation is more flexible and robust than the thin 28 AWG stranded metal wire, this significantly improved the mechanical stability of the connections by increasing resistance to tension and lateral forces. This method ensures reliable electrical contact while providing mechanical stability. The crimping procedure for both the PCB side and ZIF side crimp pins is illustrated and described in Fig. 6.4 and Fig. 6.5.

Each crimped connection undergoes mechanical testing, including the application of lateral forces, to verify its integrity and stability. This step is particularly crucial given prior issues with connection failures caused by mechanical and thermal stress during chamber assembly.

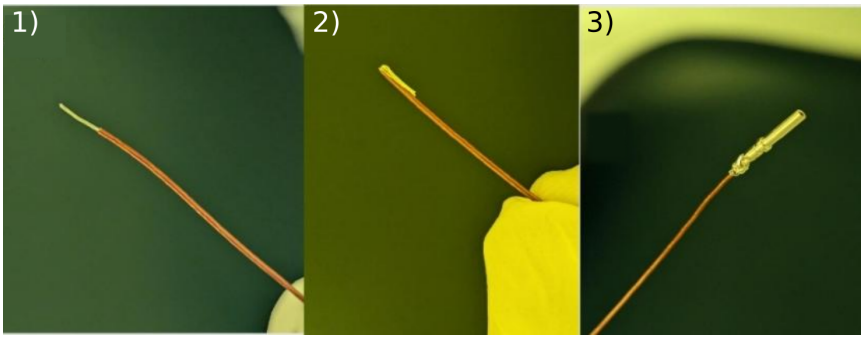


Figure 6.5: Wire crimping procedure for the ZIF side crimp pins. 1) Strip a 5 mm section of the Kapton insulation. 2) Fold the wire over the Kapton insulation. 3) Insert the wire into the crimp pin making sure the Kapton part is inside the pin and crimp the pin right above the vent hole. In this case the entire stranded core is folded over the Kapton insulation, as these connections interface with wider crimp pins that accommodate the full wire gauge.

Wire to PCB soldering

Just like the soldering of the PCB + ZIF socket assembly, soldering the wires to the PCB pads and ZIF pins requires precision and care to avoid damaging the PCB traces. The same soldering techniques and settings described in Section 6.1.2 were used. This stage of the process also required significant practice, with several failed attempts before a reliable and repeatable procedure was established.

Out of the 102 wires, 21 are soldered directly to the ZIF socket pins, 19 DC and 2 RF, while the remaining wires are soldered to the PCB side. This sequence is chosen to ensure accessibility, as the ZIF socket pins located near the center of the PCB would be difficult to reach if the PCB-side wires were soldered first. The crimped pins are carefully slid onto their corresponding ZIF socket pins, followed by the precise application of solder at the base of each pin. Maintaining proper pin orientation during soldering is critical at this stage. Each crimped pin must remain perpendicular to the PCB surface while the solder flows, to prevent unintended contact with neighboring traces or pins. Precision tweezers are used to hold each pin in place until the solder solidifies, ensuring a stable and properly aligned final connection. Following this the PCB side wires are soldered in a similar fashion.

To ensure cleanliness during soldering, each completed wire connection is immediately wrapped in UHV-grade aluminum foil. As soldering progresses, each newly soldered wire is carefully added to the protected bundle to prevent contamination. Once all the wires are soldered, the assembly undergoes a final cleaning step to remove residual solder flux.

During soldering, flux can seep into the crimp pins and into regions of the ZIF sockets that are inaccessible from the outside. As a result, the only effective method to fully remove this trapped flux is to sonicate the entire assembly in IPA. However, care must be taken during sonication, as Kapton-insulated wires are not compatible with ultrasonic cleaning. To address this, the assembly is carefully positioned in a sonicator bath filled with IPA, with the liquid level maintained precisely just above the crimp pins. This ensures that only the crimped regions, PCB, and ZIF socket are submerged, while the Kapton wires remain above the solvent and are not subjected to sonication. The assembly is sonicated for 4 minutes. After cleaning, all 102 solder joints are visually inspected and mechanically tested using a gentle pull test to identify any weak connections that could fail during handling or thermal cycling. Fig 6.6 shows the wire harness assembly at this point of the procedure.

Once the wires are cleaned, the stainless steel bridge is installed onto the assembly. This bridge is what mounts the wire harness and trap assembly inside the vacuum chamber. A wire strain relief system is also added at this point. This consists of two stainless steel plates with through holes in the same gird patterns as the PCB pads. Each wire soldered onto the PCB then passes through its corresponding hole in the strain relief plate. These plates effectively fix the wires in place and prevent any lateral forces from being transferred to the wire-crimp joint where the wires are the weakest. This adds another layer of protection to prevent the PCB wires from breaking during handling and installation. The wire strain relief plates and bridge are shown in Fig 6.7.

PEEK micro-D connector assembly

Following wire soldering and cleaning, the last step is the assembly of the PEEK 100 pin micro-D connector that mates the wire harness to the vacuum feedthrough. This is the same beige PEEK connector that comes with the commercially available wire harness imaged in Fig. 6.2. We were not able to source just the connector itself so we salvaged one from a previous failed commercial harness. The connector was easily removable by unscrewing it, which separated it into two halves. The wires are held in place between the two halves with crimp pins that fit into the connector. Once unscrewed the wires can easily be pulled out. Now we can replace the removed wires with the clean wires we prepared and soldered to the PCB. This connector is designed to hold wires that have been terminated by a specific type of crimp pin which we were able to source from the wire harness manufacturer. Each wire is passed through it's corresponding pin hole in the connector. At this step, careful attention has to be paid to the wire mapping from the PCB to the micro-D connector. We made a specific mapping which minimizes the wires

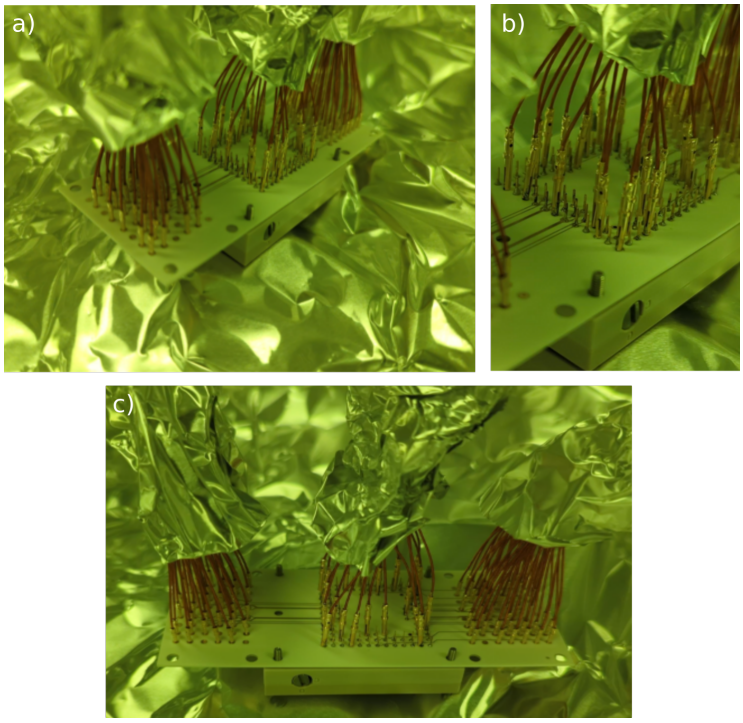


Figure 6.6: Soldered PCB+ZIF socket assembly. a) Shows the entire wire harness assembly after the wires are soldered onto the PCB+ZIF socket assembly. b) Shows a close up of the wires that were soldered directly onto the ZIF socket pins instead of the PCB for easier soldering. c) Shows a side view of the assembly. This assembly was cleaned in a sonicator bath with IPA with the IPA level just above the gold crimp pins to ensure the Kapton wires were not sonicated.

entangling with each other. This mapping was thoroughly documented as this is what determines what voltages will be sent to specific trap electrodes from the outside of the vacuum chamber once it is sealed. After passing all the wires through the connector, the Kapton insulation on each wire is stripped by 0.5 mm, inserted into the crimp pin and crimped by a specialized crimping tool specifically designed for these crimp pins which was also sourced from the wire harness manufacturer. Once all the wires are crimped, the crimp pin can be aligned and pushed into the PEEK connector and the two halves of the connector can be joined together.

This concludes the assembly of the wire harness. The finished product is shown in Fig. 6.7. Now we have to perform thorough electrical tests on it to make sure the correct PCB to connector mapping was followed and that there were no shorts developed between

PCB traces and wires anywhere along the assembly process. This is done with a custom made testing jig that has a PCB that mimics the Phoenix trap's CPGA. This mock CPGA is inserted into the ZIF socket and the micro-D connector is connected to the vacuum electrical feedthrough. The testing jig has contact points which can be probed with a multimeter. The other multimeter probe contacts the connection pins on the electrical feedthrough. This way we can check for electrical continuity all the way for the ZIF socket (where the trap is) to the outside of the electrical feedthrough (where we will send voltages to the trap from). The electrical contacts on the testing jig are also labeled with the PCB pad labels. This lets us verify the PCB to micro-D connector mapping. By probing all 100 contact points on the testing jig against all 100 pins on the electrical feedthrough, we can check for electrical shorts between every possible pair of connections. This amounts to 4950 possible shorting paths, making the process extremely time consuming but necessary to ensure all trap electrodes would be functional.

The PCB to micro-D connector mapping only has to be verified once after the assembly is completed, but the electrical shorts need to be tested multiple times as the assembly of the vacuum chamber progresses. This is because we found that shorts can easily develop during handling of the assembly and chamber baking. These shorts are most likely caused by small (< 1 mm) conductive particles making their way onto the PCB traces or connector pins during assembly and installation. Therefore, it is essential to test for electrical shorts at each stage of the vacuum chamber assembly. Since this process is highly time-consuming, multiple lab members take turns conducting the tests. Involving multiple people not only distributes the workload but also increases the reliability of the results by reducing the likelihood of oversight or human error.

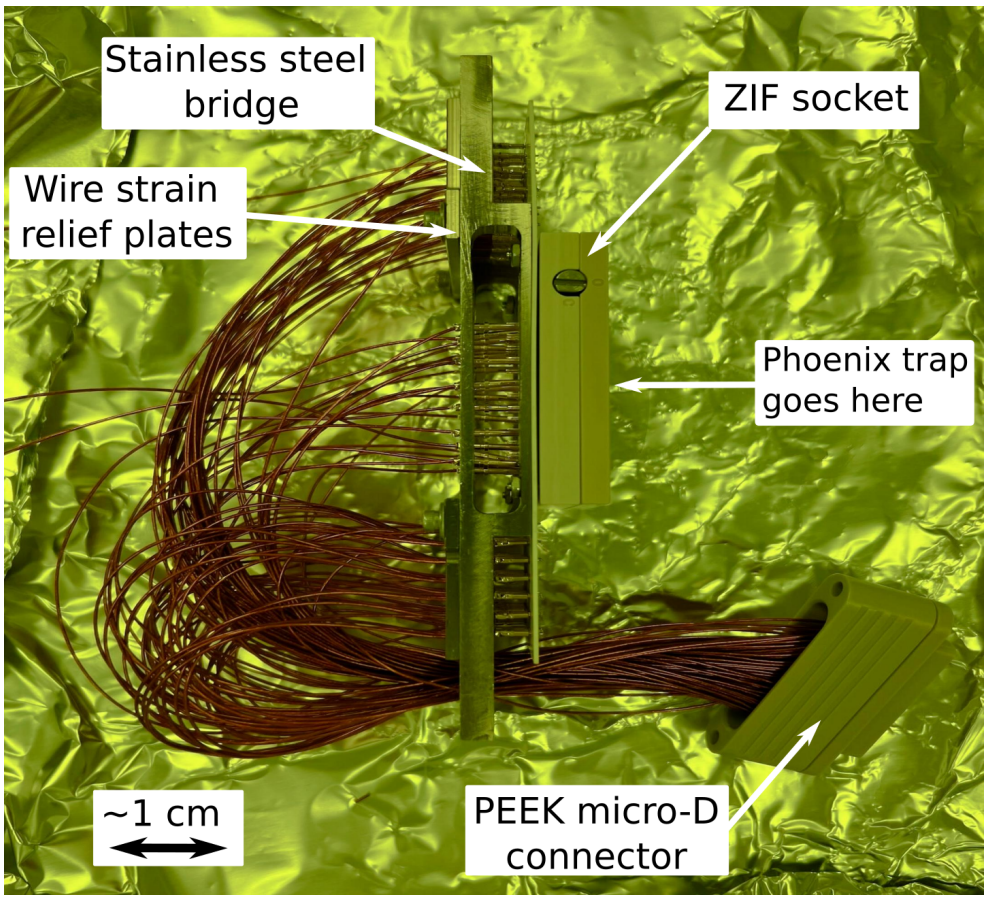


Figure 6.7: Image of the completed in-vacuum wire harness ZIF socket assembly. The CPGA of the Phoenix trap mounts into the ZIF socket. The stainless steel bridge attaches the assembly inside the vacuum chamber by screwing into brackets inside the chamber. The PEEK micro-D connector connects to the UHV electrical feedthrough on the vacuum chamber flange which makes the electrical connections accessible from outside the vacuum chamber.

6.2 Vacuum chamber assembly

The wire harness ZIF socket assembly can now be installed into the vacuum chamber. The system is designed for the surface-electrode trap to sit at the geometric center of the experimental chamber. Precision position of the trap in the exact center of the chamber is necessary for optimal optical access and ion loading. Therefore, custom made alignment jigs are used to ensure that the assembly is correctly positioned inside the chamber. This jig is referenced to the experimental chamber by being bolted to the chamber via the same bolting holes used for the Raman laser re-entrants. The jig has precisely machined notches where the trap CPGA slides into. A mock mechanical sample of the trap CPGA is installed in the ZIF socket which works as a stand in for the actual Phoenix trap. The jigs are installed onto the chamber followed by the wire harness assembly and it is ensured that the mock CPGA sits snugly inside the alignment notches in the jigs. This system ensures that the trap is positioned to within 150 μm of the chamber's center. Fig. 6.8 shows this alignment jig and it being used to align the wire-harness assembly. The alignment jigs are removed once the wire harness ZIF socket assembly is aligned and screwed in. The whole process of the chamber assembly is carried out in a class 10,000 cleanroom to prevent contaminating the chamber which can adversely affect vacuum pressures. Even so much as the presence of a single hair inside the vacuum chamber can prevent the chamber from reaching UHV pressures, so it is vital to carry out the assembly process in a cleanroom environment. The cleanroom environment is also essential for the microfabricated Phoenix trap. The trap has micron-sized features that can easily be damaged by dust particles or contaminated by microscopic debris. Fig. 6.9 shows the assembly station and cleanroom setup where there vacuum assembly was done

6.2.1 Chamber sealing and Bake-out

After the chamber internals are installed, the chamber needs to be sealed closed and baked. UHV systems needs to be baked whilst being evacuated using vacuum pumps to remove the adsorbed gases from the walls of the chamber. The most common gas species that needs to be removed is water vapor which gets adsorbed in the chamber walls when the chamber is exposed to atmosphere. This baking is done at temperatures between 150° and 250° usually for about two weeks. The longer the chamber is baked, the more gases are removed. However, after approximately two weeks, the pressure typically begins to plateau, and extending the bake duration beyond this point yields diminishing returns. Typical trapped ion vacuum chambers just go through one of these long baking cycles to reach UHV. However, such a long baking cycle is not possible with the Phoenix trap

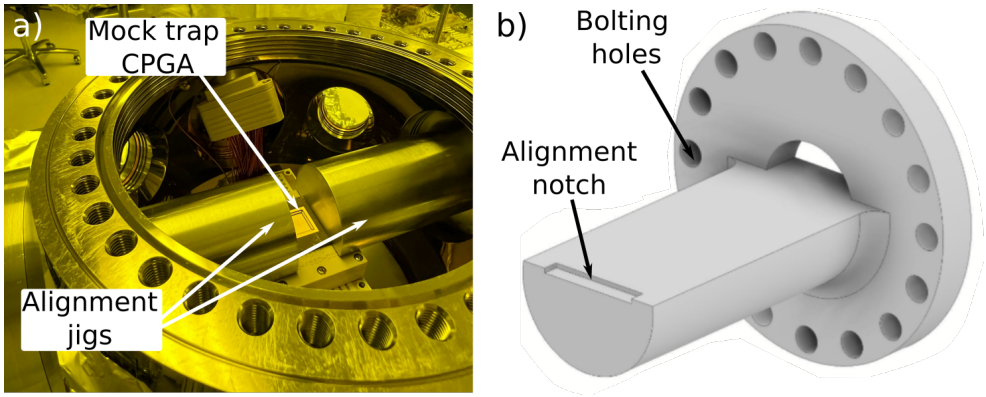


Figure 6.8: Alignment jigs used to center the Phoenix trap. a) Shows an image of the alignments jigs installed in the chamber and being used to align the wire harness ZIF socket assembly. b) Shows a CAD rendering of the alignment jig. The mock trap CPGA fits into the notches in the alignment jigs. These notches and the jig are referenced to the experimental chamber and attached to it via the multiple bolts that are used for attaching the Raman re-entrants. The large number of bolts tightly constrains the jig to the chamber. This ensures the traps is within 150 μm of the chamber's center.

installed due to the trap's limited baking window. To get around this, our chamber goes through two baking stages: A long bake for approximately two weeks to remove the bulk of the water vapor in the chamber without the Phoenix trap and ablation targets installed. Once this long bake is completed, the trap and ablation targets are installed and the chamber is baked again for about two days to remove any water that was introduced back into the system whilst the trap was being installed. Once the chamber is brought back to atmosphere after the long bake, it is imperative to install the trap and ablation targets as fast as possible to limit the amount of water that gets introduced to the inner chamber walls. This limitation is specific to our version of the Phoenix trap, as Sandia National Laboratories has recently introduced an upgraded model capable of withstanding a cumulative bake time of up to 79 days [25].

During baking, the desorped gases are pumped out using vacuum pumps. Pumping down a chamber from atmospheric pressures to UHV requires several types of pumps. The internal pumps of the chamber are the ion pump and the NEG pumps shown in Fig. 3.2. However, these internal pumps can only be activated once the pressure of the chamber is below 10^{-6} mbar level. A turbomolecular pump is usually used to bring the pressure from atmosphere to the 10^{-6} mbar level. The turbomolecular pump is the pump that is turned on whilst the chamber is baking and it removes the bulk of the gases desorped from the



Figure 6.9: Shows the assembly station and cleanroom setup where the vacuum chamber was assembled. We can see the chamber connected to the turbomolecular pump in red.

chamber. All the components used during and after chamber evacuation and bakeout are listed in Table 6.1

Component	**Manufacturer**	**Model**	**Pumping Speed**	**Purpose**
Ion Pump	Agilent Technologies	VacIon Plus 75	75 liter/sec	Primary UHV pumping
Ion Pump Controller	Agilent Technologies	IPCMini	NA	System control
NEG Modules	SAES Getters	CapaciTorr HV1400 (x2)	1400 liter/sec (H_2)	Primary UHV pumping
turbomolecular pump	Pfeiffer Vacuum	HiCube 300	240 liter/sec (N_2)	Initial pump-down
Extractor Gauge	Pfeiffer Vacuum	IMG 430	NA	Pressure monitoring
Residual Gas Analyzer	Stanford Research Systems	RGA 200	NA	Gas analysis

Table 6.1: Vacuum components used to achieve UHV pressures.

Before the baking begins, the chamber needs to be sealed closed. Sealing the chamber is a whole process in itself. This involves attaching the experimental chamber back onto the five-way cross (see Fig. 3.2). The experimental chamber was removed from the five-way cross to install the wire harness assembly. Then, all the ports on the experimental chamber need to be closed which includes viewports, re-entrants and the electrical feedthrough. All ports on our chamber use CF flanges, which are standard in UHV systems. These flanges employ what is known as a knife-edge seal. Both the flange and the corresponding port on the vacuum chamber feature a sharp, machined knife-edge. A soft copper gasket is placed between the two knife-edges and compressed as the flange is tightened with bolts, creating a metal-to-metal vacuum-tight seal capable of withstanding extreme pressures and temperatures. When the flange is being tightened and the copper gasket is compressed, it is imperative that the compression occurs evenly across the entire circumference of the gasket. Uneven compression can result in microscopic leaks at the gasket–knife-edge interface, which can significantly compromise the vacuum seal and prevent the chamber from reaching UHV pressures.

To ensure the copper gasket is evenly compressed and a vacuum-tight seal is achieved, the bolts are tightened in a specific sequence using a three-stage torque procedure. The process begins with an initial torque of 60 in-lbs, followed by a second stage at 130 in-lbs, and concludes with a final torque of 190 in-lbs. Uniform gasket compression is verified by measuring the gaps between flanges with feeler gauges to ensure consistency across all bolt positions. The bolt tightening sequence is shown in Fig. 6.10.

Once the chamber is sealed, the turbomolecular pump is attached to it via an all metal bake valve on the diagnostic chamber. To minimize turbulent airflow during the initial pump-down, which can mobilize contaminants within the chamber and potentially lead to wire breakage, we modify the standard flange configuration. The turbomolecular pump is connected to the chamber via a 2.75-inch CF flange, which typically uses a copper gasket with a 1.475-inch Inner-Diameter (ID). However, to suppress turbulence, we replace this gasket with a modified version containing an approximately 1 mm aperture. With this modified gasket, the pump is connected, the valve is opened and the pump is turned on. The initial pump-down is performed using a roughing pump that is integrated into the turbomolecular pump assembly. Once the chamber pressure reaches approximately 7 mbar (with atmospheric pressure being around 1000 mbar), the valve is closed, and the pump is turned off and removed. At this point, the modified copper gasket, with the ≈ 1 mm aperture, is replaced with the standard 1.475-inch ID gasket. Since most of the air has now been evacuated, the risk of turbulent airflow is minimal, and the standard gasket can be used without concern.

After re-connecting, the turbomolecular pump is turned on and we should expect to

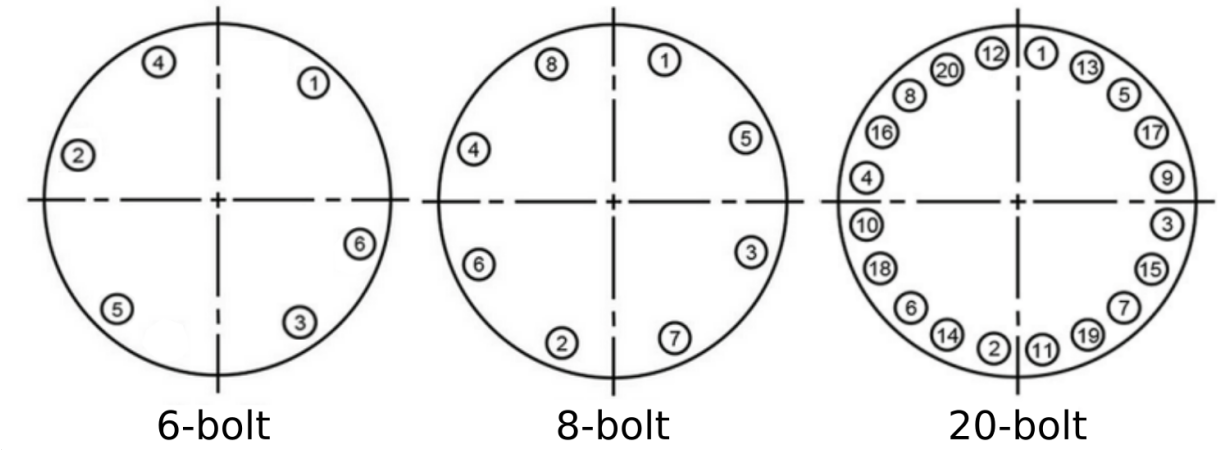


Figure 6.10: Bolt tightening sequence used for sealing the CF flanges on our vacuum chamber. The chamber has 2.75 inch CF flanges with 6 bolts, 4.5 inch CF flanges with 8 bolts, and 8 inch CF flanges with 20 bolts.

reach pressures of 10^{-5} mbar level within 10 minutes. If this pressures isn't achieved within that time frame, it indicates that there is a leak on one or more of the vacuum flanges. These leaks need to be detected and fixed by either re-tightening the flange bolts or by completely re-placing the copper gasket on those flanges. Leaks are detected by spraying the outside of the flanges with helium gas. If there is a leak, the helium enters the chamber and is detected via the RGA connected to the diagnostic chamber. The RGA has a special leak testing setting that makes it extra sensitive to helium gas. Helium is great for leaking testing due to is small atomic size, inert nature, and low natural abundance in air. The flange–chamber interface is sprayed with helium, and the partial helium pressure is monitored using the RGA. Any spike in the helium signal above the baseline indicates a leak at the location being sprayed at that moment.

The long bake

Once the $\approx 10^{-5}$ mbar pressure is achieved with just the turbomolecular pump. We can begin the long bakeout of the chamber. For our chamber, this bakeout is done at 150° C. The bakeout temperature is limited by the temperature rating of the electrical contact pins on the ZIF socket, as recommended by the socket manufacturer.

The turbomolecular pump is removed, and the chamber is moved into the environmental temperature chamber. This environmental chamber is the TestEquity 1027C Temperature

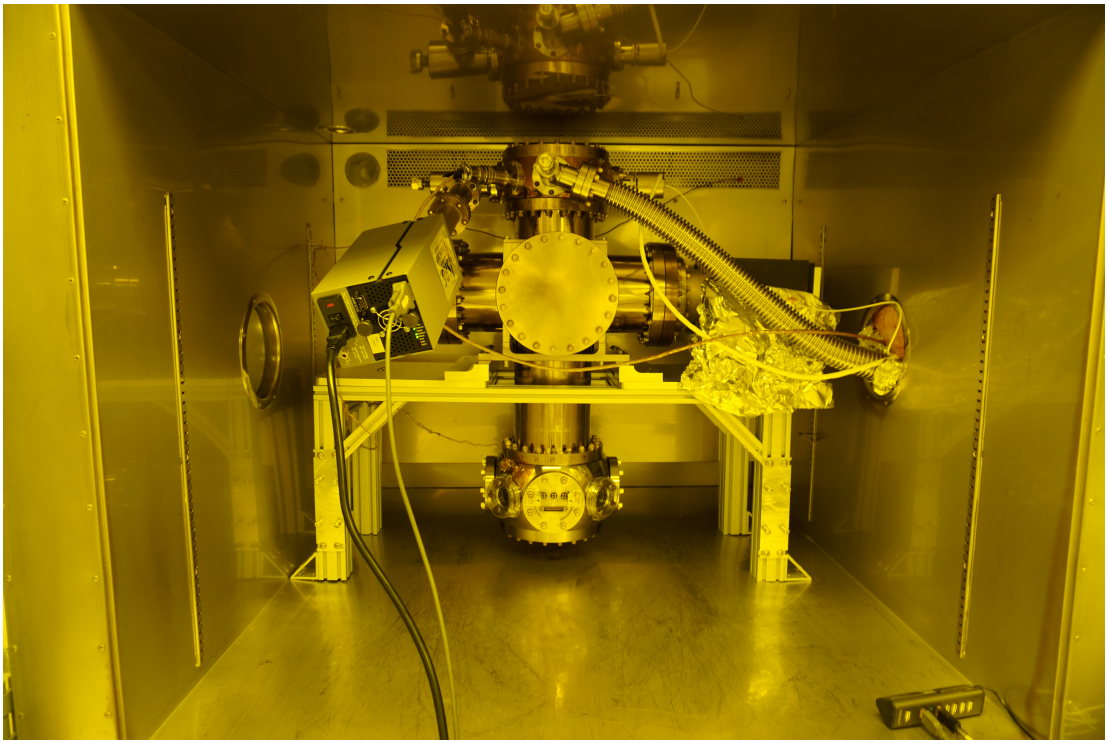


Figure 6.11: Image of the vacuum chamber inside the TestEquity 1027C Temperature Chamber. The bellows for the turbomolecular pump are feed into the temperature chamber through a feedthrough on the right.

Chamber which has a temperature range between $-73°$ C and $200°$ C. The turbomolecular pump is connected back to the chamber through a feedthrough on the temperature chamber. Fig 6.11 shows the vacuum chamber inside the environmental chamber. An important step before starting the long bake is the degassing of the extractor gauge, ion pump and RGA. These components have filaments/electrodes that can accumulate deposits during operation. The degassing procedure involves operating these electrodes at higher-than-normal temperatures, which removes the accumulated deposits and contaminants. This process must be carried out while the turbomolecular pump is running so that the released materials are efficiently pumped out of the chamber. The degassing can also only be done at chamber pressures of 10^{-7}mbar or below as these components cannot operate at higher pressures as the filaments/electrodes can burnout under the higher gas load. The degassing procedure is described below:

1. Turn ON the turbomolecular pump

2. Wait for the turbomolecular pump and its connections to reach 10^{-5}mbar
3. Open the all metal bake vale
4. Ramp the temperature from room temp (30° C) to 150° C at a rate of 20° C/hr
5. Once the pressures reaches 10^{-7}mbar, turn ON the extractor gauge
6. Ramp the temperature down to 30° C at a rate of 20° C/hr
7. First degas the RGA filament
8. Then degas the extractor gauge

Now the long bakeout can begin. The long bakeout procedure is described below:

1. Turn ON the turbomolecular pump
2. Turn OFF the extractor gauge. As the pressure will go up with rising temperature
3. Ramp the temperature from room temp (30° C) to 150° C at a rate of 20° C/hr
4. Once the pressures reaches 10^{-7}mbar, turn ON the extractor gauge
5. Ramp the temperature down to 80° C at a rate of 20° C/hr. This is the temperature at which the NEG pumps are activated as per the manufacturers recommendation
6. Activate the NEG pumps (550° C for 1 hour and 15 minutes)
7. Ramp the temperature up to 150° C at a rate of 20° C/hr
8. Leave the chamber at 150° C for 2 weeks or until the pressure reaches a stable plateau.
9. Ramp the temperature down to 80° C at a rate of 20° C/hr.
10. Re-activate the NEG pumps (550° C for 1 hour and 15 minutes)
11. Ramp the temperature down to 30° C at a rate of 20° C/hr
12. Degas the ion pump
13. Turn ON ion pump

At the end of the long bakeout, the chamber went down to a lowest pressure of 3.64×10^{-11} mbar. The temperature is always ramped at a rate of 20° C/hr. This is done to ensure that there is no rapid thermal expansion on the chamber viewports. Rapid expansion can lead to the failure of the glass-metal seal on the viewports which can introduce microscopic leaks. Such leaks can only be fixed by replacing the viewports. This is something we have to be extremely careful about as the viewports on our chamber are custom made with custom coatings which can take upto 6 months to replace.

Trap and atomic source installation

Once the long bakeout is completed, the most challenging phase of the assembly begins: installing the ablation targets and the Phoenix trap. As detailed in the introduction to this chapter, several factors contribute to the complexity of this step: the radioactivity of the ablation target $^{133}Ba^{+}$, the rapid oxidation of the metal ablation target, the limited baking tolerance of the Phoenix trap, and the lack of replacements for many components. To minimize the risk of failure, a detailed step-by-step checklist was developed, refined over several weeks, and validated through multiple practice runs.

The day before the long bakeout is finished and the chamber is removed from the temperature chamber, the non-radioactive $BaCl_2$ ablation target strips are prepared and installed on the ablation target holder. Once the chamber is removed from the temperature chamber, is it kept sealed until the Phoenix trap can be installed. The cleanroom used for this assembly is a shared space between multiple laboratories. However, due to the radioactivity of the $^{133}Ba^{+}$ atomic source, the facility had to be closed off to all other users during this stage of the assembly. This created yet another obstacle, as we had to complete the work within a limited time frame to ensure the facility could be reopened for other researchers.

On the day of the installation, one lab member begins the preparation of the radioactive $BaCl_2$ ablation target strips. This and other subsequent steps involving the radioactive sample are done under the supervision of the University's radiation safety officer. These strips are prepared according to the ablation target recipe outlined in section 5.1 and then installed onto the front part of the ablation target holder which holds the radioactive source as seen in Fig. 5.7. The preparation of the $BaCl_2$ ablation target strips and their installation onto the target holder were performed by PhD student Hawking Tan. Simultaneously, another lab member begins the preparation of the barium metal ablation targets. To prevent oxidation of barium metal, this preparation step is performed inside a nitrogen glove box which keeps the oxygen and moisture level below 0.01 Parts-Per-Million (PPM). The barium metal which comes packaged inside the argon filled glass ampules

is removed from the ampules inside this glove box. Since the barium metal can come in chunks of varying shapes and size, the chunks are shaped into cuboids using a custom-made press. The barium metal is then installed on the back part of the ablation target holder which holds the non-radioactive $BaCl_2$ strip and the barium metal as seen in Fig. 5.7 . The non-radioactive strip was already installed onto this holder the day before. The barium metal is installed onto the holder and is it ensured that the surface normal of the target is pointing towards the trapping region of the Phoenix trap. This target holder is kept inside the glove box until the next step of the installation can begin. The preparation of this barium metal target was performed by post-doctoral researcher Dr. Akbar Jahangiri Jozani.

Simultaneously to the preparation of the radioactive and barium metal ablation targets. Two lab members begin the installation of the Phoenix trap into the experimental chamber. The trap is installed from the bottom of the experimental chamber and screwed in from the sides. This requires us to remove just three ports from the experimental chamber: the bottom imaging re-entrant and the two Raman beam re-entrants. The trap is then carefully installed into the ZIF socket and secured in place. Extreme care must be taken when handling the trap to avoid damaging any of the sensitive electrodes or wire bonds. Although the installation is performed in a cleanroom environment, it is still important to minimize the trap's exposure time to atmosphere, as dust particles and other contaminants are still present, even in cleanrooms, and could damage the microfabricated device. The Phoenix trap installation was performed by PhD student Akimasa Ihara and the author. The final orientation of the trap inside the chamber was thoroughly verified and documented by multiple lab members. Fig. 6.12 shows the Phoenix trap installed inside the experimental chamber and process of doing so.

Once the Phoenix trap is installed. The lab member preparing the barium metal ablation target and holder is informed and instructed to remove the metal target from the nitrogen glove box and bring it to the cleanroom. The radioactive $BaCl_2$ targets are brought into the cleanroom at the same time. Now the clock starts ticking and we have to install these ablation targets into the chamber as quickly as possible to reduce the oxidation of the barium metal.

First, the two parts of the ablation target holders need to be joined together and then installed onto the metal shield shown in Fig. 6.1. The barium metal ablation target is brought to the cleanroom from the nitrogen filled glove box inside a nitrogen filled bag. This bag is quickly passed onto lab members who are assembling the ablation target holder + shield assembly. To minimize oxidation of the barium metal during this step, a in-house made plastic glove bag was built by us to perform this step in. This glove is constantly supplied with nitrogen gas and an oxygen sensor is used to ensure the oxygen content is

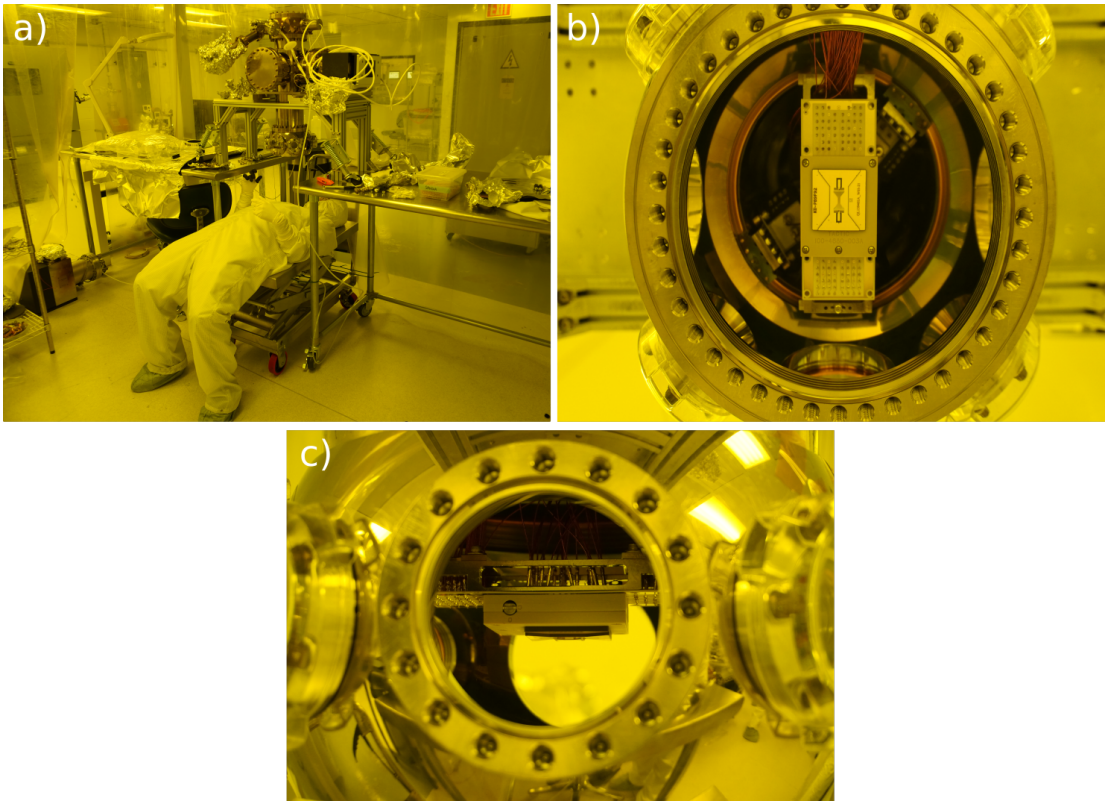


Figure 6.12: Installation procedure of the Phoenix trap. a) Shows PhD student Akimasa Ihara installing the Phoenix trap into the experimental chamber from the bottom. After the trap is inserted into the ZIF socket, another lab member tightens it in place. b) Shows a bottom view of the trap installed in the experimental chamber. c) Shows a side view of the trap installed in the chamber.

close to zero percent. The two parts of the ablation target holder are place inside this nitrogen environment along with all the tools required to assemble them. Fig. 6.13 shows this smaller nitrogen glove bag and the ablation targets holders being assembled inside it.

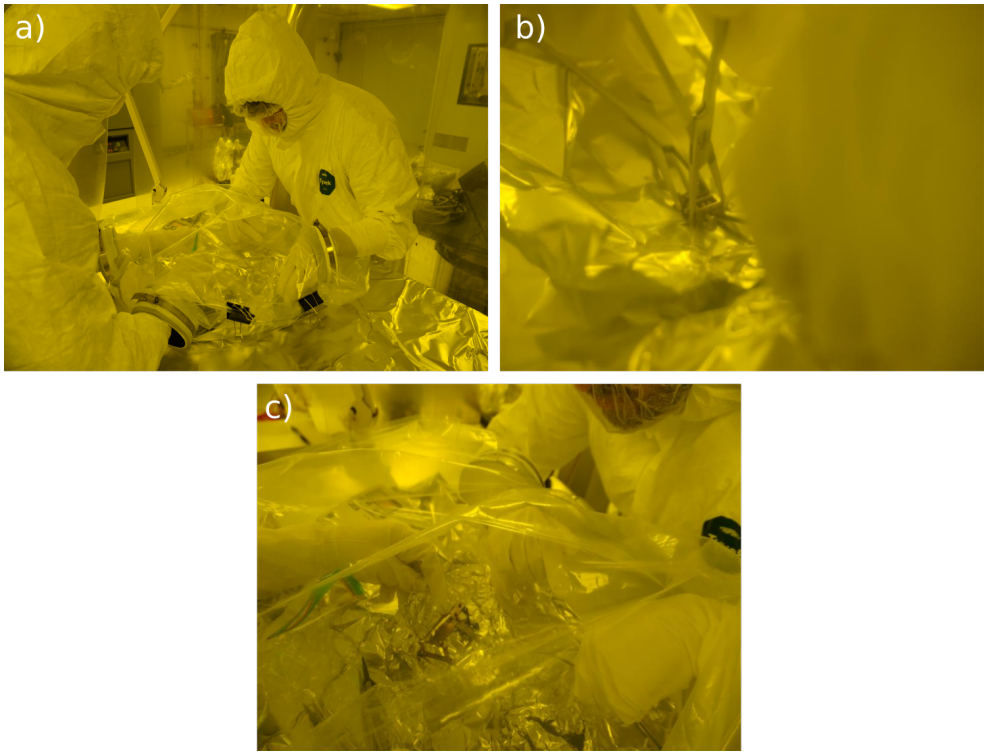


Figure 6.13: Assembly of the ablation target holder + shield assembly inside the nitrogen filled glove bag. a) Shows the smaller in-house made nitrogen filled glove bag used to assemble the ablation target holder + shield assembly in order to minimize exposure of the barium metal to oxygen and reduce oxidation. Two lab members need to work together to put the assembly together using tweezers and screw drivers. b) Shows the two halves of the ablation target being joined together. c) Shows the ablation target being installed onto the metal shield.

Once the ablation target holder + shield assembly is ready, it can be installed into the experimental chamber. We also need to minimize the exposure of the barium metal to oxygen once the ablation targets are inside the chamber as well as it can take several minutes to seal the chamber back up and start pumping. For this another larger in-house nitrogen filled glove bag was made which was installed at the bottom of the chamber on the experimental chamber. Then the entire vacuum chamber and the glove bag were filled with nitrogen until almost all the oxygen was displaced as measured by an oxygen meter. This larger glove bag is shown in Fig. 6.15. One lab member gets underneath this glove bag and installs the ablation target holder + shield assembly whilst other lab members pass all the required components and tools through an opening in the glove bag. Once the

ablation target holder + shield assembly is installed, we immediately begin sealing up the chamber.

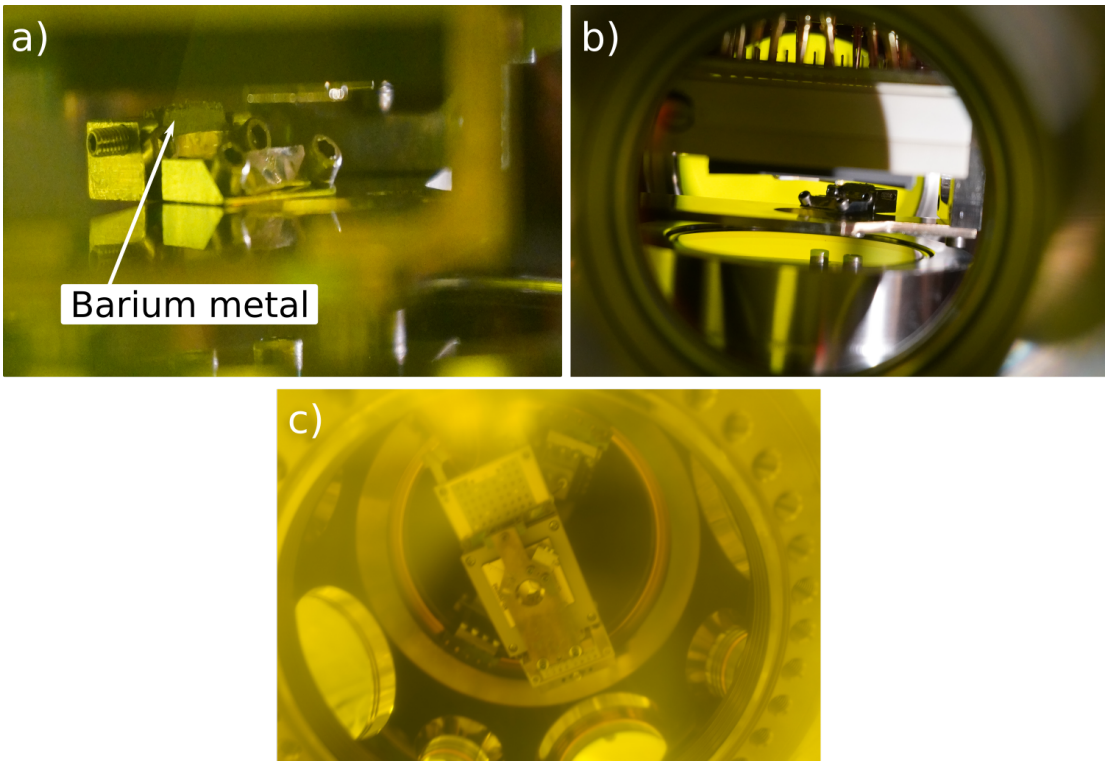


Figure 6.14: Shows the ablation target holder + shield assembly installed inside the experimental chamber. a) and b) shows two views of the ablation target + shield installed inside the chamber after it was sealed. In a) we can clearly see that the barium metal source still has the its silvery metallic surface that it had before being removed from the glass ampule. This indicated that we were successfully able to mitigate excessive oxidation of the barium metal. c) Shows an image of the metal shield installed in the trap from the bottom of the chamber before it is sealed.

The larger glove bag is kept on until the chamber is sealed following the bolt tightening procedure described earlier. Fig 6.14 shows the multiple views of the ablation target holder + shield assembly installed inside the chamber. Using these in-house made nitrogen filled glove bags, we were able to greatly reduce the oxidation of barium metal atomic source. We can clearly see in Fig 6.14 c) that the barium metal still has its silvery metallic surface with barely any oxidation compared to the images in Fig 5.6 b). Thus, the additional effort and complexity introduced into the assembly procedure to reduce oxidation proved worthwhile,

as it gives us greater confidence in reliably producing neutral barium atoms from the metallic barium source without significant risk of barium oxide flakes contaminating the surface-electrode trap.

The turbomolecular pump is then attached and the bulk of the nitrogen gas and residual oxygen is pumped out. During this initial pumping, the small aperture copper gasket is again used to reduce turbulent air flow in the chamber and then replaced with the regular gasket. At this point, all flanges on the vacuum chamber are checked to ensure even compression of the copper gaskets with feeler gauges. Once the pressure reaches approximately 10^{-5} mbar , the valve is closed, the turbomolecular pump is removed, and the chamber is transferred back to the temperature chamber for the short bakeout, after which the turbomolecular pump is reconnected.

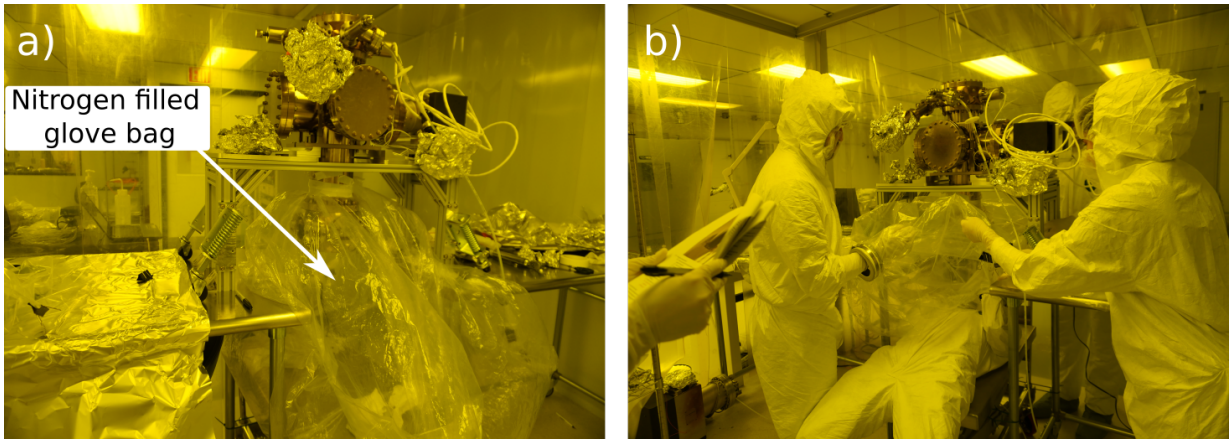


Figure 6.15: Nitrogen filled glove bag for installation of the ablation target holder + shield assembly. a) Show the larger in-house made nitrogen filled glove bag attached over the experimental chamber with cleanroom grade tape. The bag and the vacuum chamber are filled with nitrogen gas to minimize the exposure of the barium metal to oxygen whilst it sits in the chamber while it is being sealed. b) Shows PhD student Akimasa Ihara underneath the glove bag installing the ablation target holder + shield assembly whilst other lab members hand in components and tools through an opening in the glove bag.

The short bakeout

Now the short bakeout of the vacuum chamber can begin. This bakeout is meant to remove any moisture or gases adsorbed into the chamber walls during the ablation targets and trap installation. The short bakeout procedure is described below:

1. Turn ON the turbomolecular pump
2. Wait for the turbomolecular pump and its connections to reach 10^{-5} mbar
3. Ramp the temperature from room temp (30° C) to 120° C at a rate of 20° C/hr
4. Leave the chamber at 120° C until a pressure of 10^{-7} mbar is achieved. We would like to have this low pressures for degassing and leak checking
5. Turn ON the extractor guage
6. Ramp the temperature from 120° C to 30° C
7. Degas the RGA filament
8. Degas the extractor gauge
9. Perform leaks check on all the chamber's flanges using helium
10. Ramp the temperature from 30° C to 80° C at a rate of 20° C/hr
11. Activate the NEG pumps (550° C for 1 hour and 15 minutes)
12. Ramp the temperature from 80° C to 150° C at a rate of 20° C/hr
13. Leave the chamber at this temperature for a maximum of 60 hrs (limited by the Phoenix trap's baking constraint) or until a pressure of high 10^{-9} mbar is reached
14. Ramp the temperature from 150° C to 80° C
15. Re-activate the NEG pumps (550° C for 1 hour and 15 minutes)
16. Ramp the temperature from 80° C to 30° C
17. Turn ON the ion pump

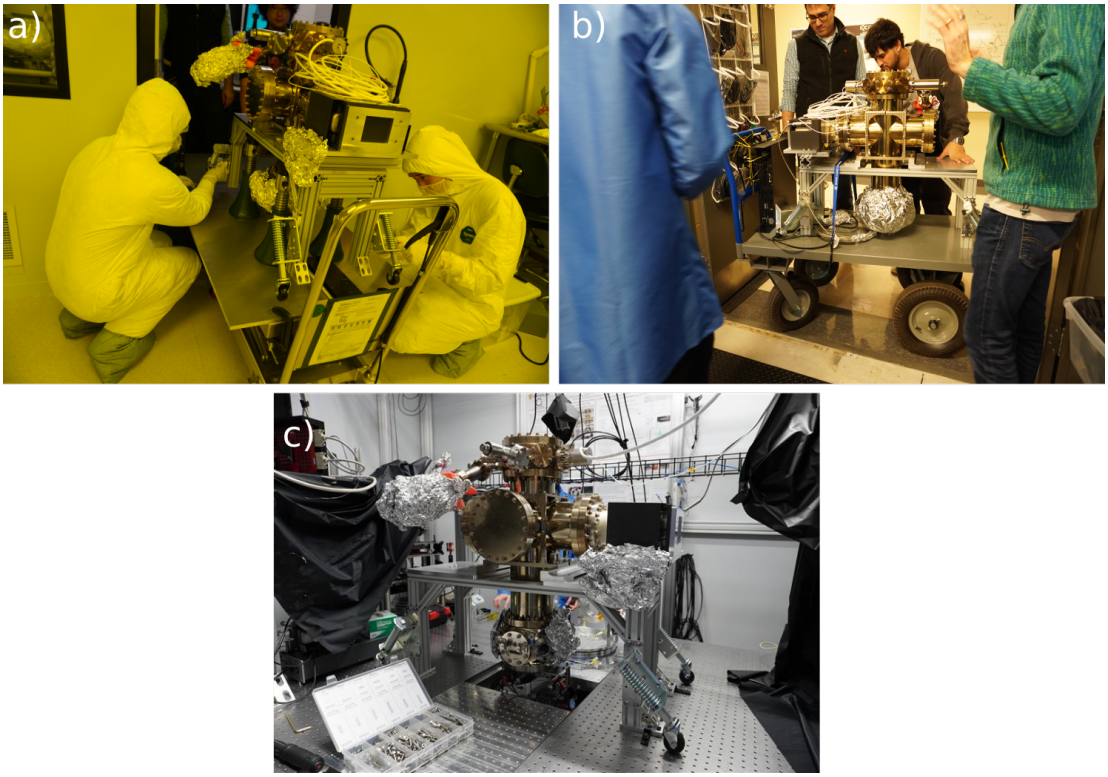


Figure 6.16: Moving the vacuum chamber to the Lab. a) and b) shows the process of moving our vacuum chamber from the cleanroom in RAC-1 where it was assembled to our lab in RAC-2. c) Shows our vacuum chamber installed onto the optics table in our lab.

The vacuum chamber is kept in the temperature chamber until the pressure reaches a stable value. Whilst in the temperature chamber, another round of electrical tests is done to check for electrical shorts. During this electrical testing, it was discovered that one of the DC electrodes was shorted to the ground point of the PCB. The vacuum chamber was removed from the temperature chamber and another round of leak checks was conducted. Once this was done, the vacuum chamber can be moved from the cleanroom and moved to our lab.

Fig. 6.16 shows the process of moving the vacuum chamber from the cleanroom to the optics table in our lab. During this move, a Uninterruptable-Power-Supply (UPS) was used to keep the ion pump turned on so that the pressure in the chamber wouldn't go up too much. Once the chamber was installed onto the optics table, the chamber pressure was approximately 4×10^{-11} mbar. However, after moving the pressure keeps going down

as the ion pump and the NEG pumps are still pumping. A few days after the move, the pressure stabilized to approximately 3×10^{-11} mbar. The chamber was moved to the lab in late November 2024. At the time of writing this thesis in July 2025, the pressure still sits at the $\approx 3 \times 10^{-11}$ mbar range. Fig. 6.17 shows the pressure of the chamber with time from the start of the short bake to a few days after it was moved to the lab. Therefore, we were successfully able to install the Phoenix trap, a radioactive $BaCl_2$ atomic source, a metallic barium source with minimal oxidation and a wire harness with ~ 100 connections inside our vacuum chamber and achieve low UHV pressures of $\approx 3 \times 10^{-11}$ mbar.

We conducted another round of electrical tests after the move and discovered that two more DC electrodes were shorted to the ground point of the PCB. This is not a surprise given the shorts we have seen in the past developed during previous installations and baking runs. Discussions with other research groups using similar ion traps informed us that it is actually very difficult to install these surface-electrode traps without developing any shorts and the best course of action is to just use the trap with a few shorts on it rather that try to fix them. The three shorts in our trap will not stop us from trapping as we only need about 3-5 consecutive unshorted DC electrodes to trap a chain of 16 ions given a 4 μm separation between neighboring ions. These shorted electrodes are also shorted to a ground point which is better than no connection to them as them being grounded means they are not floating and won't accumulate stray charges which can distort the trap's confining potential. Actually, assembling this whole system with just 3 shorts out of the 152 DC electrodes on the trap is quite a big achievement given the lack of PCB solder mask, the sheer number and spatial density of the connections, and the sensitive components on the microfabricated trap.

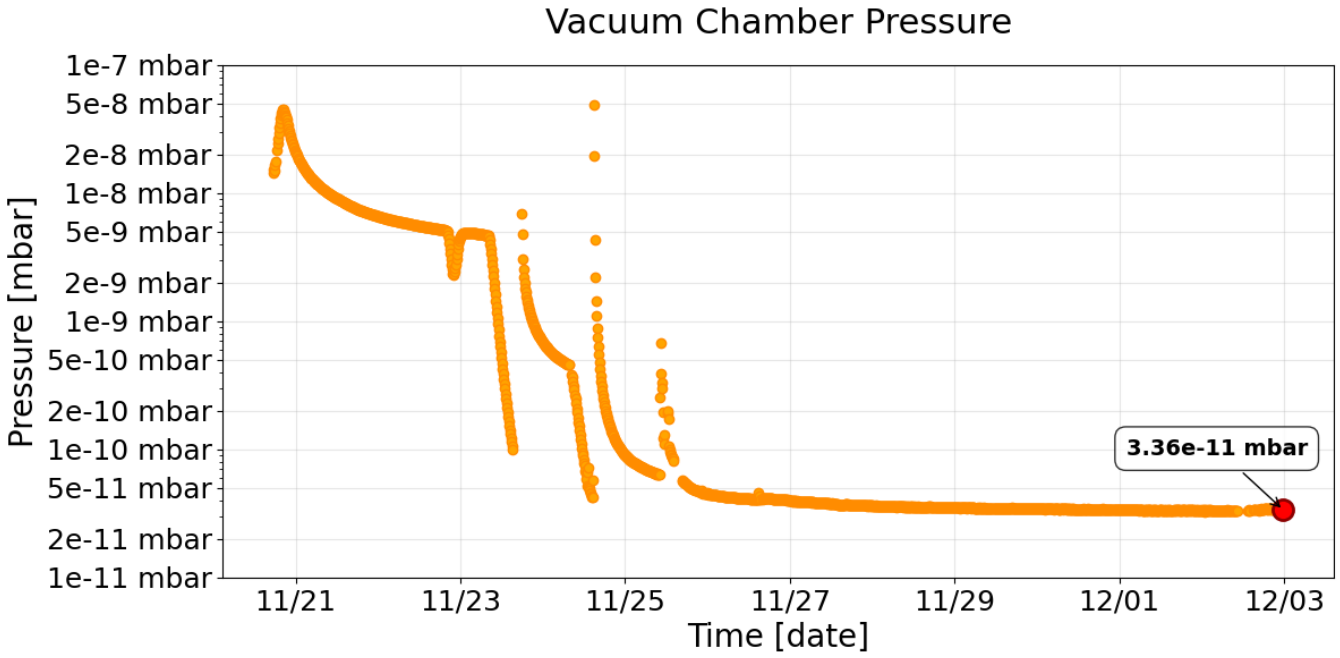


Figure 6.17: Pressure of the vacuum chamber during the short bake and a few days after it was moved to the lab. The plotting begins once the pressure reaches the 10^{-7} mbar level as that is when the extractor gauge can be turned on. The plot shows several spikes and gaps. The spikes are due to the degassing procedures done during bakeout and the gaps are due to connection loss or turning the gauge off when moving the chamber. The chamber was moved to the lab on November 25th 2024 and we can see that about 4 days after that the pressures started to plateau to around 3×10^{-11} mbar.

6.3 Summary

The centrally mounted surface-electrode trap design of our vacuum chamber maximizes both optical access and conductance from the trap to the vacuum pumps. These two capabilities are critical: the high optical access enables precise individual ion addressing for tunable, all-to-all interactions between ions, while the high conductance ensures exceptionally long ion lifetimes—an essential requirement for executing extended, large-scale experiments. Together, they create a uniquely capable platform for performing sophisticated quantum simulation protocols that would be difficult to realize in more conventional trap geometries. In this chapter, we have demonstrated that it is indeed feasible to build a UHV compatible wire harness using only commercially available components to route nearly 100 electrical connections to a centrally mounted trap. This achievement not only validates the practicality of the centrally mounted architecture, but also establishes a scalable, reproducible pathway toward the next generation of ion trap experiments that demand both high optical access and the ability to sustain large, stable ion chains over long durations.

The chapter then detailed the assembly of the vacuum chamber, which integrates three highly desirable features into a single platform: a microfabricated surface-electrode trap for scalable ion trapping experiments, a radioactive barium-133 atomic source for high-fidelity qubit initialization and readout, and a metallic barium atomic source for robust and repeatable ion loading. The stringent constraints imposed by the Phoenix trap's baking limits, as well as the challenges posed by the radioactivity and rapid oxidation of the atomic sources, required the development of innovative solutions. These solutions do more than simply overcome technical hurdles—they pave the way for integrating advanced ion trapping technology with challenging atomic sources in a UHV environment.

In doing so, this work brings us one step closer to realizing large-scale, high-fidelity quantum simulations, by demonstrating that such a complex and demanding system can be designed, assembled, and operated with readily available components.

Chapter 7

Summary and outlook

The work described in this thesis broadly contributes to addressing some of the technical challenges involved in building a trapped ion system capable of performing large-scale quantum simulation experiments. A significant portion of my master's degree was devoted to assembling the vacuum internals and the vacuum chamber itself. Through this process, I gained firsthand experience with the many components required to build a trapped ion system. This work gave me direct insight into the precision, patience, and attention to detail necessary to bring such systems into operation, as well as an appreciation for their inherent sensitivity. These experiences deepened my respect not only for the efforts of experimental physicists in the field, but also for the contributions I was able to make myself.

The results in Chapter 4 provide an estimate of the largest stray electric fields that can be compensated for with the Phoenix trap, given the voltage output limits of the DAC used in our system. These estimates were obtained through numerical simulations of single-ion trajectories under the electric potential generated by the Phoenix trap. Our results quantitatively demonstrate that the Phoenix trap is capable of effectively compensating for the typical stray electric fields—and therefore excess micromotion—encountered in trapped-ion systems. Since these results are based on numerical simulations, the next natural step will be to experimentally verify the micromotion compensation range of our trap once ions have been successfully trapped.

We discussed how one of the biggest problems of the surface-electrode trap architecture is the shallow trap depth. The shallow trap depth of surface-electrode traps presents an obstacle in trapping the fast moving atoms, especially from $BaCl_2$ salt, generated by laser ablation. The results in Chapter 5 demonstrated that laser ablation of barium metal

produces a larger number of slower atoms compared to $BaCl_2$ salt. The atomic plume generated from the ablation of barium metal contained a significant number of atoms with kinetic energy less than the maximum trap depth achievable by the Phoenix trap which suggests that loading rates from a barium metal source are expected to be much higher in surface-electrode traps. This is a very important result as both barium ions and surface-electrode traps are becoming increasingly popular in the trapped ion community and this results demonstrates how barium metal can be a very promising atomic source for barium based surface-electrode trap systems. In this chapter we were able to conclude from the measurement of the velocity distribution of the atomic plume that barium metal should lead to higher loading rates, however, a much more concrete result would be to actually trap barium ions and experimentally measure the loading rates in our trap. Since our system has both metallic barium and $BaCl_2$ salt ablation targets, the next obvious step of this work would be to experimentally measure the loading rates from both sources and show that the metallic source does indeed lead to higher loading rates in surface-electrode traps.

The results in Chapter 6 revolved around assembling our vacuum chamber. We discussed the issue of bringing $\sim$ 100 electrical connections to a centrally mounted surface electrode trap. We showed that it is indeed possible to implement a UHV compatible wire harness solution that makes these connections possible with commercially available components. We then discussed the very complex assembly procedure of a vacuum chamber that featured a surface-electrode trap with a limited baking window and a multi-species atomic source with radioactive and rapidly oxidizing barium ablation targets. The successful assembly described in this chapter proves that it is indeed possible, with a lot of patience and planning, to construct a trapped ion system with a lot of desirable features which include a surface-electrode trap, low UHV pressure, high NA optical access, and a multi-species barium atomic source with high trapping probability. System with such features are what will enable scalable, large scale and high fidelity quantum simulation and computation experiments.

The next step for this system is to trap barium ions. The first isotope we will attempt to trap will of course be $^{138}Ba^+$ from the barium metal ablation target as the metal target will facilitate in trapping with a system that has not yet been optimized. The next steps involve setting up the optical and electrical infrastructure in the lab required for trapping ions which the group is currently working on. This requires setting up the optical system for delivering the 493 nm, 650 nm, 553 nm and 405 nm laser beams required for ion loading, Doppler cooling and SPAM. Once an ion is trapped we can begin optimizing system parameters such as laser frequencies, laser intensities, laser beam alignment, aligning the ion imaging system for state detection and trapping voltages etc. Once the system is

setup and optimized, we can begin characterizing it. This can include measuring the trap frequencies, micromotion, loading rates and demonstrating Rabi oscillations. Much of the design choices of our vacuum chamber revolved around optimizing optical access for individual addressing of ions and lower vacuum pressures for long ion lifetimes. Therefore, setting up the Raman individual addressing system and imaging system that uses the high NA viewports on our vacuum chamber would prove the real capabilities of this system. Proving these capabilities would require measuring the SPAM and gate fidelities, optical crosstalk and ion lifetimes of a long chain of ions. From there on, the system would be able to tackle large scale quantum simulation problems that are far beyond the reach of a classical computer. This includes quantum simulation of spin models with arbitrary connectivity. With Raman-based individual addressing and control of ion–ion interactions, it becomes possible to engineer tunable spin Hamiltonians where the interaction range and graph connectivity can be precisely programmed. This allows us to explore a wide class of many-body phenomena, such as long-range Ising models, magnetism, or dynamical phase transitions. The technical challenges addressed in this thesis will hopefully contribute to the exploration of complex physical phenomena and to a deeper understanding of nature.

References

[1] Yuri i. manin. mathematics as metaphor: Selected essays of yuri i. manin. *Philosophia Mathematica*, 17(1):122–123, 04 2008.

[2] Yuhi Aikyo, Geert Vrijsen, Thomas W. Noel, Alexander Kato, Megan K. Ivory, and Jungsang Kim. Vacuum characterization of a compact room-temperature trapped ion system. *Applied Physics Letters*, 117(23):234002, 12 2020.

[3] D. T. C. Allcock, W. C. Campbell, J. Chiaverini, I. L. Chuang, E. R. Hudson, I. D. Moore, A. Ransford, C. Roman, J. M. Sage, and D. J. Wineland. omg blueprint for trapped ion quantum computing with metastable states. *Applied Physics Letters*, 119(21), November 2021.

[4] T. G. Ballance, J. F. Goodwin, B. Nichol, L. J. Stephenson, C. J. Ballance, and D. M. Lucas. A short response time atomic source for trapped ion experiments. *Review of Scientific Instruments*, 89(5), May 2018.

[5] Paul Benioff. The computer as a physical system: A microscopic quantum mechanical Hamiltonian model of computers as represented by Turing machines. *Journal of Statistical Physics*, 22(5):563–591, May 1980.

[6] D. J. Berkeland, J. D. Miller, J. C. Bergquist, W. M. Itano, and D. J. Wineland. Minimization of ion micromotion in a paul trap. *Journal of Applied Physics*, 83(10):5025–5033, 05 1998.

[7] R. B. Blakestad, C. Ospelkaus, A. P. VanDevender, J. M. Amini, J. Britton, D. Leibfried, and D. J. Wineland. High-fidelity transport of trapped-ion qubits through an **X**-junction trap array. *Phys. Rev. Lett.*, 102:153002, Apr 2009.

[8] Brendan Bramman. *Ablation loading and qudit measurements with barium ions*. PhD thesis, University of Waterloo, 2023.

[9] Marko Cetina, Andrew T. Grier, and Vladan Vuletić. Micromotion-induced limit to atom-ion sympathetic cooling in paul traps. *Phys. Rev. Lett.*, 109:253201, Dec 2012.

[10] J. Chiaverini, R. B. Blakestad, J. Britton, J. D. Jost, C. Langer, D. Leibfried, R. Ozeri, and D. J. Wineland. Surface-electrode architecture for ion-trap quantum information processing. *Quantum Info. Comput.*, 5(6):419–439, September 2005.

[11] Justin E Christensen. *High-fidelity operation of a radioactive trapped-ion qubit,* $^{133}Ba^{+}$. PhD thesis, University of California, Los Angeles, 2020.

[12] Justin E. Christensen, David Hucul, Wesley C. Campbell, and Eric R. Hudson. High-fidelity manipulation of a qubit enabled by a manufactured nucleus. *npj Quantum Information*, 6(1), April 2020.

[13] F. Diedrich, J. C. Bergquist, Wayne M. Itano, and D. J. Wineland. Laser cooling to the zero-point energy of motion. *Phys. Rev. Lett.*, 62:403–406, Jan 1989.

[14] David P. DiVincenzo. The physical implementation of quantum computation. *Fortschritte der Physik*, 48(9–11):771–783, September 2000.

[15] Ebba Edqvist. Characterization of micromotion induced by rf phase shift with photon correlation detection in a paul trap. Master's thesis, KTH Royal Institute of Technology, Stockholm, Sweden, 2022.

[16] Colin J.C. Epstein. Design and implementation of the real-time control system for an open trapped ion quantum computing platform. Master's thesis, University of Waterloo, 2023.

[17] Richard P. Feynman. Simulating physics with computers. *International Journal of Theoretical Physics*, 21(6-7):467–488, 1982.

[18] Zachary Fisher. Shuttling of ions for characterization of a microfabricated ion trap. Bachelor's Thesis, Massachusetts Institute of Technology, 2012.

[19] J. P. Gaebler, T. R. Tan, Y. Lin, Y. Wan, R. Bowler, A. C. Keith, S. Glancy, K. Coakley, E. Knill, D. Leibfried, and D. J. Wineland. High-fidelity universal gate set for $^{9}Be^{+}$ ion qubits. *Phys. Rev. Lett.*, 117:060505, Aug 2016.

[20] I.M. Georgescu, S. Ashhab, and Franco Nori. Quantum simulation. *Reviews of Modern Physics*, 86(1):153–185, March 2014.

[21] Noah Greenberg. Vacuum and optical designs for an open-access trapped ion quantum processor. Master's thesis, University of Waterloo, 2015.

[22] Noah Greenberg. *Trapping of Ba^+ using an Autoionizing Resonance and Construction of an Academic Ba^+ Testbed*. PhD thesis, University of Waterloo, 2024.

[23] Noah Greenberg, Akbar Jahangiri Jozani, Collin J. C. Epstein, Xinghe Tan, Rajibul Islam, and Crystal Senko. Microgram bacl2 ablation targets for trapped ion experiments. *Review of Scientific Instruments*, 95(4):045117, 04 2024.

[24] Lov K. Grover. A fast quantum mechanical algorithm for database search. In *Proceedings of the Twenty-Eighth Annual ACM Symposium on Theory of Computing*, STOC '96, page 212–219, New York, NY, USA, 1996. Association for Computing Machinery.

[25] Raymond A. Haltli, Eric Ou, Christopher D. Nordquist, Susan M. Clark, and Melissa C. Revelle. Mitigating the effects of au-al intermetallic compounds due to high-temperature processing of surface electrode ion traps, 2024.

[26] A. M. Hankin, E. R. Clements, Y. Huang, S. M. Brewer, J.-S. Chen, C. W. Chou, D. B. Hume, and D. R. Leibrandt. Systematic uncertainty due to background-gas collisions in trapped-ion optical clocks. *Phys. Rev. A*, 100:033419, Sep 2019.

[27] Seokjun Hong, Minjae Lee, Hongjin Cheon, Taehyun Kim, and Dong-il Cho. Guidelines for designing surface ion traps using the boundary element method. *Sensors*, 16:616, 04 2016.

[28] Hudson Group, UCLA. Ba-133: A Goldilocks Qubit, n.d. Accessed: 2025-07-01.

[29] R. Islam, E.E. Edwards, K. Kim, S. Korenblit, C. Noh, H. Carmichael, G.-D. Lin, L.-M. Duan, C.-C. Joseph Wang, J.K. Freericks, and C. Monroe. Onset of a quantum phase transition with a trapped ion quantum simulator. *Nature Communications*, 2(1), July 2011.

[30] Changhyun Jung, Woojun Lee, Junho Jeong, Minjae Lee, Yunjae Park, Taehyun Kim, and Dong-Il "Dan" Cho. A microfabricated ion trap chip with a sloped loading slot to minimize exposing trapped ions to stray charges. *Quantum Science and Technology*, 6(4):044004, jul 2021.

[31] J. Keller, H. L. Partner, T. Burgermeister, and T. E. Mehlstäubler. Precise determination of micromotion for trapped-ion optical clocks. *Journal of Applied Physics*, 118(10):104501, 09 2015.

[32] D. Kielpinski, C. Monroe, and D. J. Wineland. Architecture for a large-scale ion-trap quantum computer. *Nature*, 417(6890):709–711, 2002.

[33] K Kim, S Korenblit, R Islam, E E Edwards, M-S Chang, C Noh, H Carmichael, G-D Lin, L-M Duan, C C Joseph Wang, J K Freericks, and C Monroe. Quantum simulation of the transverse ising model with trapped ions. *New Journal of Physics*, 13(10):105003, oct 2011.

[34] Nikhil Kotibhasker. *Towards Large Scale Quantum Simulations with Trapped Ions: Programmable XY model, Precise Light Sensing, and Extreme High Vacuum*. PhD thesis, University of Waterloo, 2024.

[35] M Kumph, P Holz, K Langer, M Meraner, M Niedermayr, M Brownnutt, and R Blatt. Operation of a planar-electrode ion-trap array with adjustable rf electrodes. *New Journal of Physics*, 18(2):023047, February 2016.

[36] D. Leibfried, R. Blatt, C. Monroe, and D. Wineland. Quantum dynamics of single trapped ions. *Rev. Mod. Phys.*, 75:281–324, Mar 2003.

[37] Pei Jiang Low. *Control and Readout ofHigh-Dimensional Trapped Ion Qudits*. PhD thesis, University of Waterloo, 2023.

[38] M-Labs. Artiq: Advanced real-time infrastructure for quantum physics, 2023. Accessed: 2025-07-14.

[39] T. Andrew Manning. *QUANTUM INFORMATION PROCESSING WITH TRAPPED ION CHAINS*. PhD thesis, University of Maryland, 2014.

[40] Peter Lukas Wilhelm Maunz. High optical access trap 2.0. Technical report, Sandia National Lab. (SNL-NM), Albuquerque, NM (United States), 01 2016.

[41] C. Monroe, W. C. Campbell, L.-M. Duan, Z.-X. Gong, A. V. Gorshkov, P. W. Hess, R. Islam, K. Kim, N. M. Linke, G. Pagano, P. Richerme, C. Senko, and N. Y. Yao. Programmable quantum simulations of spin systems with trapped ions. *Rev. Mod. Phys.*, 93:025001, Apr 2021.

[42] Giovanna Morigi, Jürgen Eschner, and Christoph H. Keitel. Ground state laser cooling using electromagnetically induced transparency. *Phys. Rev. Lett.*, 85:4458–4461, Nov 2000.

[43] M-Labs. ARTIQ: Advanced Real-Time Infrastructure for Quantum Physics, 2025. Accessed: 2025-07-14.

[44] D. P. Nadlinger, P. Drmota, D. Main, B. C. Nichol, G. Araneda, R. Srinivas, L. J. Stephenson, C. J. Ballance, and D. M. Lucas. Micromotion minimisation by synchronous detection of parametrically excited motion, 2021.

[45] Nicoguaro. Saddle point on the graph of $z = x^2 - y^2$ (hyperbolic paraboloid). https://en.wikipedia.org/wiki/File:Saddle_point.svg, 2016. Own work, licensed under CC BY 3.0. Uploaded to Wikimedia Commons on May 18, 2016.

[46] G Pagano, P W Hess, H B Kaplan, W L Tan, P Richerme, P Becker, A Kyprianidis, J Zhang, E Birckelbaw, M R Hernandez, Y Wu, and C Monroe. Cryogenic trapped-ion system for large scale quantum simulation. *Quantum Science and Technology*, 4(1):014004, October 2018.

[47] Wolfgang Paul. Electromagnetic traps for charged and neutral particles. *Rev. Mod. Phys.*, 62:531–540, Jul 1990.

[48] Wolfgang Paul and Helmut Steinwedel. Ein neues massenspektrometer ohne magnetfeld. *Zeitschrift Naturforschung Teil A*, 8:448, 06 2014.

[49] Adam Pauli. Classical control of an ion in a surface trap. Master's thesis, University of Innsbruck, 2011.

[50] JM Pino, JM Dreiling, C Figgatt, JP Gaebler, SA Moses, MS Allman, CH Baldwin, M Foss-Feig, D Hayes, K Mayer, C Ryan-Anderson, and B Neyenhuis. Demonstration of the trapped-ion quantum ccd computer architecture. *Nature*, 592(7853):209—213, April 2021.

[51] D. Porras and J. I. Cirac. Effective quantum spin systems with trapped ions. *Phys. Rev. Lett.*, 92:207901, May 2004.

[52] John Preskill. Fault-tolerant quantum computation, 1997.

[53] John Preskill. Quantum Computing in the NISQ era and beyond. *Quantum*, 2:79, August 2018.

[54] Melissa C. Revelle. Phoenix and peregrine ion traps, 2020.

[55] Vladimir L. Ryjkov, XianZhen Zhao, and Hans A. Schuessler. Simulations of the rf heating rates in a linear quadrupole ion trap. *Phys. Rev. A*, 71:033414, Mar 2005.

[56] A. Safavi-Naini, R. J. Lewis-Swan, J. G. Bohnet, M. Gärttner, K. A. Gilmore, J. E. Jordan, J. Cohn, J. K. Freericks, A. M. Rey, and J. J. Bollinger. Verification of a many-ion simulator of the dicke model through slow quenches across a phase transition. *Phys. Rev. Lett.*, 121:040503, Jul 2018.

[57] S. Seidelin, J. Chiaverini, R. Reichle, J. J. Bollinger, D. Leibfried, J. Britton, J. H. Wesenberg, R. B. Blakestad, R. J. Epstein, D. B. Hume, W. M. Itano, J. D. Jost, C. Langer, R. Ozeri, N. Shiga, and D. J. Wineland. Microfabricated surface-electrode ion trap for scalable quantum information processing. *Phys. Rev. Lett.*, 96:253003, Jun 2006.

[58] Sankaranarayanan Selvarajan, Nikos Daniilidis, Sönke Möller, Rob Clark, Frank Ziesel, Kilian Singer, Ferdinand Schmidt-Kaler, and Hartmut Häffner. Electric field compensation and sensing with a single ion in a planar trap, 2011.

[59] X. Shi, S. L Todaro, G. L. Mintzer, C. D. Bruzewicz, J. Chiaverini, and I. L. Chuang. Ablation loading of barium ions into a surface-electrode trap. *Applied Physics Letters*, 122(26):264002, 06 2023.

[60] Peter W. Shor. Polynomial-time algorithms for prime factorization and discrete logarithms on a quantum computer. *SIAM Journal on Computing*, 26(5):1484–1509, 1997.

[61] James D. Siverns and Qudsia Quraishi. Ion trap architectures and new directions. *Quantum Information Processing*, 16(12), November 2017.

[62] David S. Smith and Michael G. Stabin. Exposure rate constants and lead shielding values for over 1,100 radionuclides. *Health Physics*, 102(3):271–291, March 2012.

[63] A. S. Sotirova, J. D. Leppard, A. Vazquez-Brennan, S. M. Decoppet, F. Pokorny, M. Malinowski, and C. J. Ballance. High-fidelity heralded quantum state preparation and measurement, 2024.

[64] Daniel Lynn Stick. *Fabrication and Characterization of Semiconductor Ion Traps for Quantum Information Processing*. Ph.d. thesis, University of Michigan, 2007. Accessed via Deep Blue repository.

[65] Xinghe Tan. Optimization of the optical infrastructure and trapping potential for a quantum processor based on trapped barium ions. Master's thesis, University of Waterloo, 2024.

[66] Q. A. Turchette, Kielpinski, B. E. King, D. Leibfried, D. M. Meekhof, C. J. Myatt, M. A. Rowe, C. A. Sackett, C. S. Wood, W. M. Itano, C. Monroe, and D. J. Wineland. Heating of trapped ions from the quantum ground state. *Phys. Rev. A*, 61:063418, May 2000.

[67] Martin W. van Mourik, Pavel Hrmo, Lukas Gerster, Benjamin Wilhelm, Rainer Blatt, Philipp Schindler, and Thomas Monz. rf-induced heating dynamics of noncrystallized trapped ions. *Phys. Rev. A*, 105:033101, Mar 2022.

[68] Pengfei Wang, Chun-Yang Luan, Mu Qiao, Mark Um, Junhua Zhang, Ye Wang, Xiao Yuan, Mile Gu, Jingning Zhang, and Kihwan Kim. Single ion qubit with estimated coherence time exceeding one hour. *Nature Communications*, 12(1), January 2021.

[69] Shannon X. Wang, Guang Hao Low, Nathan S. Lachenmyer, Yufei Ge, Peter F. Herskind, and Isaac L. Chuang. Laser-induced charging of microfabricated ion traps. *Journal of Applied Physics*, 110(10):104901, 11 2011.

[70] Brendan M. White, Pei Jiang Low, Yvette de Sereville, Matthew L. Day, Noah Greenberg, Richard Rademacher, and Crystal Senko. Isotope-selective laser ablation ion-trap loading of $^{137}Ba^{+}$ using a $bacl_2$ target. *Phys. Rev. A*, 105:033102, Mar 2022.

[71] Yichao Yu, Keqin Yan, Debopriyo Biswas, Vivian Ni Zhang, Bahaa Harraz, Crystal Noel, Christopher Monroe, and Alexander Kozhanov. In-situ mid-circuit qubit measurement and reset in a single-species trapped-ion quantum computing system, 2025.

APPENDICES

Appendix A

Wires harness components and tools

Component	Manufacturer	Part Number	Specifications
DC wires	Accu-Glass	100690	28 AWG, Kapton-insulated, stranded core
RF wires	Accu-Glass	112366	26 AWG, Kapton-insulated, solid core
ZIF socket	Tactic Electronics	100-4680-001A	100-pin, UHV compatible, Au plated
PCB	PCBway	Custom	No solder mask, exposed Cu traces
PCB crimp Pins	DigiKey	1807-0-15-15-43-27-04-0	Au plated, for PCB connections
ZIF crimp Pins	Accu-Glass	100180	Au plated, for ZIF connections
Micro-d connector crimp Pins	MPF Products	A11543-1	Be-Cu alloy, 0.018" diameter
PEEK Micro-D connector	MPF Products	A9601-100-36	100-pin UHV feedthrough interface
UHV solder	Accu-Glass	110796	Pb-free, UHV compatible
UHV flux	Accu-Glass	110797	Isopropyl soluble, UHV compatible

Table A.1: Components used in the In-vacuum wire harness assembly. All components are UHV compatible as our chamber achieved $\approx 3 \times 10^{-11}$ pressure with these components inside.

Tool	**Manufacturer**	**Part Number**	**Purpose**
Connector Crimp Tool	MPF Products	A4109-1-CT	Micro-D connector assembly
PCB/ZIF Crimp Tool	Sopoby	HSC8 6-4A	Wire terminal crimping
Wire Stripper	DigiKey	KS03-ND	Kapton wire preparation
Soldering Iron	Weller	10040293	Temperature-controlled soldering
Soldering Tip	DigiKey	T0054460199N-ND	Fine-point, temperature-stable tip

Table A.2: Tools used for the in-vacuum wire harness assembly.